9. SITE 955[1]

Shipboard Scientific Party[2]

HOLE 955A

Date occupied: 9 September 1994

Date departed: 14 September 1994

Time on hole: 4 days, 23 hr, 41 min

Position: 27°19.548′N, 15°13.848′W

Bottom felt (drill pipe measurement from rig floor, m): 2865.4

Distance between rig floor and sea level (m): 11.30

Water depth (drill pipe measurement from sea level, m): 2854.1

Total depth (from rig floor, m): 3464.80

Penetration (m): 599.40

Number of cores (including cores having no recovery): 63

Total length of cored section (m): 599.40

Total core recovered (m): 534.08

Core recovery (%): 89

Oldest sediment cored:
Depth (mbsf): 599.40
Nature: clayey nannofossil mixed sediment
Earliest age: middle Miocene

Principal results: Site 955, the third of four sites drilled into the volcanic apron peripheral to Gran Canaria, is located in the southern Canary Channel, 56 km southeast of Gran Canaria, 109 km southwest of Fuerteventura, and 125 km west of the African continental margin on the southeastern volcanic apron of Gran Canaria. The site is in line with DSDP Sites 397 and 369, 50 km and 100 km southeast of Site 955, respectively. The site is separated from Site 953 in the northern basin by the submarine ridge (maximum water depth ~1550 m) separating Fuerteventura and Gran Canaria. The drill site is in a fairly flat area at a water depth of ~2860 m. Although no structural or other complications were indicated on the high-resolution pre-site survey data, additional reflection seismic data was acquired on our approach to Site 955.

Site 955 is the first of two sites drilled in the southern volcanic apron of Gran Canaria that is open to sediment influx from the African continental margin. One of the objectives was to compare and correlate the volcaniclastic sediments south of Gran Canaria with those to be drilled in the northern basin. Because post-Miocene volcanic activity is absent in the south of the island, the influx of volcaniclastics in the upper part of the sediment column (younger than ~10 Ma) is probably small. The major events to be studied include large explosive eruptions that resulted in widespread ash flows and ash falls during Mogan and Fataga volcanism, roughly between 14 and 10 Ma.

The sedimentary succession at Site 955 was drilled with excellent recovery of ~85%. It is 599 m thick and consists dominantly of fine-grained hemipelagic sediments interbedded in the lower part with coarse-grained volcaniclastic and siliciclastic material, ranging in age from latest Quaternary to late early Miocene–early middle Miocene. The sequence at Site 955 differs from that found at Sites 953 and 954 in that the lithostratigraphy has been influenced significantly by the northwestern African continental margin in the larger amount of (1) siliciclastic material, (2) clay, as reflected also in the generally lower $CaCO_3$ concentrations of the sediment, (3) organic material, and (4) the greater abundance of slumps. Volcaniclastic material, chiefly Miocene fallout and ash turbidites from the Canary Islands, is abundant in the lower part of the sequence.

Unit I (0–207 mbsf): The upper part of the sequence is composed dominantly of clayey nannofossil mixed sediment interbedded with quartz-rich silt and sand, and minor ash layers, and has been strongly affected by slumping. Several discrete packages of presumably slumped sediment were identified in the interval from 102 to 240 mbsf. All the sediment within each of these packages belongs to the same nannofossil zone, or to consecutive zones within the limits of zonal resolution. Some zones are missing between these packages, and younger zones are present beneath older ones. The sediment accumulation rate from the surface to 102 mbsf (0–1.6 Ma) is about 67 m/m.y. At least one interval in the upper Pliocene appears to contain an allochthonous block of lower Pliocene sediment. A more regular biostratigraphic sequence was encountered below approximately 160 mbsf.

Unit II (207–273 mbsf): The middle part of the sequence is composed of clayey nannofossil mixed sediment and nannofossil clay with very minor interbedded silt and sand. No slump dislocation was found below 240 mbsf. Sediment accumulation rates (18 m/m.y.) are reasonably well constrained below 240 mbsf to about 285 mbsf (4.63–6.8 Ma) in Unit II, possibly reflecting the later part of the hiatus in volcanic activity on Gran Canaria.

Unit III (273–374 mbsf; 6.8–8.8 Ma): The accumulation rate is about 42 m/m.y, probably reflecting the earlier part of the volcanic hiatus on Gran Canaria. A hiatus appears to be present at about 370 mbsf, spanning about 0.6 m.y. between 8.8 and 9.4 Ma. A hiatus occurs in the same interval at Site 954, suggesting the possibility of a regional event.

Subunits IVa and IVb (374–567 mbsf): The bottom part of the sequence has numerous interbedded volcaniclastic deposits that can be correlated with Miocene Fataga and Mogan group volcanism on Gran Canaria. Zeolitized tuffs are common in Subunit IVa (Fataga), while more abundant unaltered glass occurs in Subunit IVb (Mogan); similar relationships were found at Site 953. Several compositionally distinct and dated individual ignimbrites studied on land have been recognized in the volcaniclastic-rich lower part of the hole (374–567 mbsf): P1 (14 Ma), which had been recognized at 845 mbsf at Site 953, ~160 km north of Site 955, as well as ignimbrites A and X (Schmincke, 1994).

Unit V (567–599 mbsf): The very bottom of the sequence marks a return to hemipelagic sedimentation with thin interbedded siliciclastic sediments and minor basaltic clasts that were probably derived from subaerial erosion of the shield of Gran Canaria.

The sediment accumulation rate is about 60 m/m.y. from 370 to about 445 mbsf (9.4–10.8 Ma) in lithologic Subunit IVa. This high rate is prob-

---

[1]Schmincke, H.-U., Weaver, P.P.E., Firth, J.V., et al., 1995. *Proc. ODP, Init. Repts.,* 157: College Station, TX (Ocean Drilling Program).

[2]Shipboard Scientific Party is given in the list preceding the Table of Contents.

ably related to the later part of the Fataga phase of volcanism on Gran Canaria. The microfossil age at 595 mbsf is 15.8 Ma, with the volcaniclastic layers suggesting an age of ~14–15 Ma by extrapolation.

Two hiatuses interrupt the sequence: one in the early Pleistocene to latest Pliocene between 102.81 and 103.1 mbsf (from 1.6 to 2.37 Ma) and one in the late Miocene between 364.0 and 373.6 mbsf (from 8.8 to 9.4 Ma). Hiatuses occur at similar times at Site 954 on the north flank of Gran Canaria.

Changes in pore-water composition are driven by the bacterially mediated oxidation of organic matter from organic-rich sediments, precipitation of dolomite, dissolution of biogenic silica, and diagenetic reactions in the siliciclastic fraction, particularly the appearance of smectites and zeolites forming at the expense of volcanic glass. Sulfate depletion ammonia production gradients at Site 955 are the steepest and reach the most extreme values of any site studied on Leg 157, indicating that sulfate reduction rates are greatest in this area. High methane contents and constant methane/ethane ratios characterize all sediments below the top of the sulfate reduction zone. Silica concentrations reach moderate values in the upper 120 m where biogenic silica is undergoing active dissolution. Salinity and chloride contents approach twice seawater concentrations near the base of the hole. Such high values are difficult to explain by normal diagenetic processes and may indicate the advection of brines derived from leaching of evaporites on the northwestern African continental margin.

Pore waters display progressive calcium enrichment and, generally, magnesium depletion with depth, in response to precipitation of dolomite combined with alteration processes affecting the volcanogenic fraction. A temporary reversal in the magnesium trend at intermediate depths may relate to brine influx.

At 71 mbsf, headspace samples of methane gas increased from background levels to between 1034 and 54965 ppm throughout the hole. C_1/C_2 ratios were mostly fairly constant between 3000 and 5000, indicating a biogenic origin of the gas, which is also supported by vacutainer samples. Organic carbon showed values between 0.5% and 2.6% C_{org} in the upper part of the hole, with a maximum of 4.77% C_{org} at 164 mbsf, while the deeper part of the hole show fairly constant lower values of C, N, and S.

Below about 80 mbsf cracks and fractures caused by expansion of gas disrupted the fabric of the core and made it impossible to determine compressional-wave velocities either with the MST, the penetration transducers, or Hamilton Frame.

A complete suite of three logging strings were successfully run at Hole 955A. The quad combination, geochemical, and FMS recorded data from the base of the hole (599 mbsf) to the end of pipe (72 mbsf). The quality of the recorded logs appears good, enabling detailed characterization of this Miocene to Holocene sequence of pelagic, turbidite, and volcaniclastic material. The geochemical logs are diagnostic indicators for the amount and composition of volcanic material. An increase in the Th log (~500 mbsf) delineates the more geochemically evolved volcaniclastics correlated to the Gran Canaria Mogan stage of volcanism. The downward transition into the shield phase of volcanism (~570 mbsf) is marked by a significant decrease in thorium, indicating the more mafic nature of the sediments. Geochemical logs indicate significant concentrations of carbonate above 217 mbsf and these abrupt variations in carbonate may delineate thick, contiguous slump blocks from the African margin to the east. High resolution microresistivity images from the FMS show current bedding in sand units and delineate ash layers as thin as 1 cm. The images will augment core-based studies of ash abundance and thickness in the zones of poor recovery and will also enable unequivocal correlation between core and logging depths. Oriented images from the FMS provide dip and strike information of the beds and should provide information on the tectonic evolution of this site.

Together with velocity data from the MST a complete velocity function from seafloor to 575 mbsf was obtained from the sonic logs, allowing a precise transformation of two-way traveltimes to depths. The depths of the seismic units at Site 955 were calculated as follows:

Unit A: 0–140 mbsf
Unit B: 140–170 mbsf
Unit C: 170–270 mbsf
Unit D: 270–420 mbsf
Unit E: 420–525 mbsf

There is generally good agreement between the stratigraphic and lithologic interpretations of the cores and the depositional architecture as derived from the seismic profile. Two major sequences can be distinguished in the seismic profile, an upper one comprising Units A, B, and C and a lower comprising Units D and E. The upper sequence, characterized by basinward thickening units and pronounced lateral change in seismic facies, corresponds to the Pliocene-Pleistocene deposits in lithostratigraphic Units I and II. The lower sequence, which thins basinward, corresponds to the middle–late Miocene lithologic Units III and IV. The transition from seismic Unit D to E seems to mark the middle/late Miocene boundary. The acoustic basement (i.e., the base of Unit E at 515 mbsf) corresponds to the top of the lower volcanic sands (lithologic Subunit IVb) tentatively correlated to the Mogan formation on the island.

Four ADARA temperature measurements taken between 27 and 113 mbsf gave a geothermal gradient of 39.99°C/km. Thermal conductivity downhole had an average value of approximately 1.15 W/(m·K), resulting in a heat flow value of 45.99 mW/m^2. These values are high for a continental margin setting and most likely reflect the Canary Island hot spot.

BACKGROUND AND OBJECTIVES

Background

Site 955, the third of four sites to be drilled into the volcanic apron peripheral to Gran Canaria, is located in the southern Canary Channel 56 km southeast of the coast of Gran Canaria, 109 km southwest of Fuerteventura, and 125 km west of the African continental margin on the southeastern volcanic apron of Gran Canaria. The site is in line with DSDP Sites 397 (Leg 47A, 50 km away) and 369 (Leg 41) 100 km southeast of Site 955. The site is separated from Site 953 in the northern basin by the submarine ridge separating Fuerteventura and Gran Canaria with a maximum water depth of ~1550 m. The drill site is in a fairly flat area at a water depth of ~2860 m.

Objectives

Site 955 is the first of two sites drilled in the southern volcanic apron of Gran Canaria. The objectives of drilling these sites are similar, with Site 955 representing the more eastern and Site 956 the more western of the Gran Canaria southern flank facies of the volcaniclastic apron.

Volcano Evolution and Correlation between Northern and Southern Sites

One of the objectives is to compare and correlate the volcaniclastic sediments south of Gran Canaria with those to be drilled in the northern basin. Because post-Miocene volcanic activity is absent in the south of the island, the influx of volcaniclastics during this time may be small. It will be of interest to contrast the facies of the volcaniclastics corresponding to the Miocene Fataga and Mogan formations (many ash flows and fallout tephra layers) in the south and north (Site 953) as both sites are at roughly similar distances from Gran Canaria.

The Shield Phase

One of the objectives at this site is to document the top of the shield stage of Gran Canaria beneath the marine equivalents of the Miocene ignimbrites.

Event Stratigraphy, Volcanology, and Chronology, and Paleowind Directions

The major events to be studied include large explosive eruptions that resulted in widespread ash flows and ash falls during Mogan and Fataga volcanism, roughly between 14 and 10 Ma. One of the objectives is to correlate characteristic subaerial ash flows with their submarine equivalents. This relates to an unsolved volcanological problem, the processes occurring when high temperature ignimbrites enter water. Because of the absence of major erosion during the time interval of the Mogan volcanic phase, at least some distinct tephra units encountered are likely to represent the distal submarine equivalents of subaerially erupted and documented ignimbrites. High resolution calibration of the biostratigraphic and paleomagnetic record against single crystal $^{40}Ar/^{39}Ar$ age dates is a major objective at this site.

We will also attempt to correlate major submarine events with distinct reflectors. Fallout ash layers from Tenerife and from Miocene explosive eruptions on Gran Canaria should help to reconstruct the fallout fans and thus help to constrain the paleowind pattern during the middle Miocene and Pleistocene.

Diagenesis

Because of the closer proximity to the island, diagenetic alteration of glassy tephra layers especially of the Mogan and Fataga formations might be more advanced than at DSDP Site 397 (Leg 47A) allowing better assessment of the effect of higher temperature on chemical fluxes between volcanic glass and pore water. The pore waters may show extreme compositions and one objective is to distinguish the chemical imprint of the Fataga from that of the Mogan glass-rich volcaniclastic deposits.

Basin Evolution

The two southern sites, unlike the two northern sites, are open to sediment influx from the African continental margin, Site 955 more so than Site 956 because the East Canary Ridge ends about 80 km northeast of Site 955. We expect a major sediment input from the African coast and shelf upwelling area, resulting in greater amounts of organic matter, siliciclastic sediments, and slump events.

UNDERWAY GEOPHYSICS

On our approach to Site 955 a ~14-km-long reflection seismic profile was acquired starting at 27°23.4′N, 15°14.1′W and ending at 27°16.0′N, 15°13.4′W. An 80 in.^{3} water gun was used as a seismic source and the signals were recorded on a single channel streamer and displayed on line-scan recorders for immediate inspection. The shot interval was 8 s corresponding to a distance of ~24 m. Data was stored digitally on 8 mm tape and subsequently processed by means of shipboard SIOSEIS software. The processing sequence was as follows: finite difference migration, bandpass filter (30–120 Hz), automatic gain control (500 ms window), trace mix (weights 1 2 1), display. The processed profile is shown in Figure 1 and the interpretative line drawing in Figure 2. The profile is located on the pre-site-survey Profile P127 covering approximately the interval SP 3500–2790. The generally high noise level on that profile resulting from bad weather conditions during the data acquisition necessitated duplication of the existing profile. Unless otherwise specified, the following description refers to the new seismic profile.

The acoustic basement is difficult to assess, but a high amplitude reflection dipping southward, from 4.40 to 4.45 s, immediately north of the profile center appears to correlate with a strong, southward descending reflector on profile P127. This reflector forms the acoustic basement on P127 and is here thought to image the flank of Gran Canaria.

Exact identification and correlation of this assumed island-flank reflector is hampered by spatial amplitude variations and a relative complex geometry. A tentative correlation across the seismic profile is shown in Figure 2. Pieces of an almost parallel reflector are seen at levels ~200 ms deeper (Fig. 1).

The island-flank reflector is covered by a sequence of nearly even thickness of 600 ms. Based on internal reflector configurations and character of reflector terminations at the boundaries, the sequence is divided into Units A, B, C, D, and E (Fig. 2). The uppermost unit (A) is characterized by an upper interval ~20 ms thick with high-amplitude reflectors concordant with the seafloor, and a lower interval with few relatively low-amplitude reflectors. In the reflector immediately beneath the seafloor a series of small sags and highs, 5–700 m long and with amplitudes of ~5 m, are seen in the northern half of the profile. The sags and highs are reflected as subtle undulations in counterphase at the seafloor. These lens-shaped bodies possibly represent cross sections in mud waves.

The base of Unit A is defined by a reflector that changes appearance along the profile. In the northern half of the profile the reflector has a relatively low and northward decreasing amplitude. The reflector is largely concordant with the seafloor, which is characterized by two broad highs separated by a narrow sag. In the southern half of the profile, the base of Unit A is defined by a nearly horizontal high-amplitude reflector. The total thickness of Unit A increases from ~90 ms at the northern end of the profile to ~150 ms at the southern end. The internal reflectors in the lower part of Unit A show two distinctly different patterns in the mounded northern part and in the southern part of the profile. In the mounds in the northern end of the profile the unit is almost transparent. Few weak reflectors are almost concordant with the seafloor. In the southern part of the profile internal reflectors, which have relatively high amplitudes, are wavy or subparallel. The reflectors onlap the basal reflector. Closer inspection shows several pinch outs, apparently mostly related to toplaps or truncations. In the southernmost part of the profile a ~2-km-wide and 80-ms-high mound, with an internal chaotic structure, rests at the base of Unit A.

The onlap surface that forms the base of Unit A defines the top of Unit B. The base of Unit B is defined by a southward gently dipping reflector onto which the internal reflectors onlap or downlap. In the southern half of the profile the thickness of Unit B is modest, 40–50 ms. In the northern half of the profile, where Unit B constitutes the lower part of the large, regular mounds, the thickness increases to a maximum of ~125 ms. In this part of the profile the internal reflectors have relatively short periods and generally have low amplitudes. The reflectors are upward convex and converge toward the edge of the mounds where they downlap onto the base of Unit B.

The internal and external structures of the mounds have a remarkable similarity to patterns described in overbank deposits along submarine channels (e.g., Cremer et al., 1985). South of the mounds Unit B is almost transparent. A single high-amplitude reflector is seen to onlap the base of Unit B in the southern part of the profile.

Unit C has a constant thickness, 75 ms, below the mounds in the northern third of the profile. The numerous internal reflectors in this zone are concordant with the base and top of the unit. The reflectors are characterized by a relatively short period. In the southern two thirds of the profile, Unit C is wedge-shaped and ranges in thickness from ~75 to ~250 ms. A remarkable change in reflector character is seen at the entrance to the wedge. The short period reflectors are here succeeded by reflectors with relatively long periods, varying amplitudes, and continuity. Tracing of the reflectors in the transition zone is difficult. Crossing reflectors may indicate that the structure is not adequately interpreted as a two dimensional structure.

The reflectors in the wedge are subparallel and slightly wavy with a tendency to diverge in a basinward (i.e., southward) direction. Internal truncations appear here and there in Unit C.

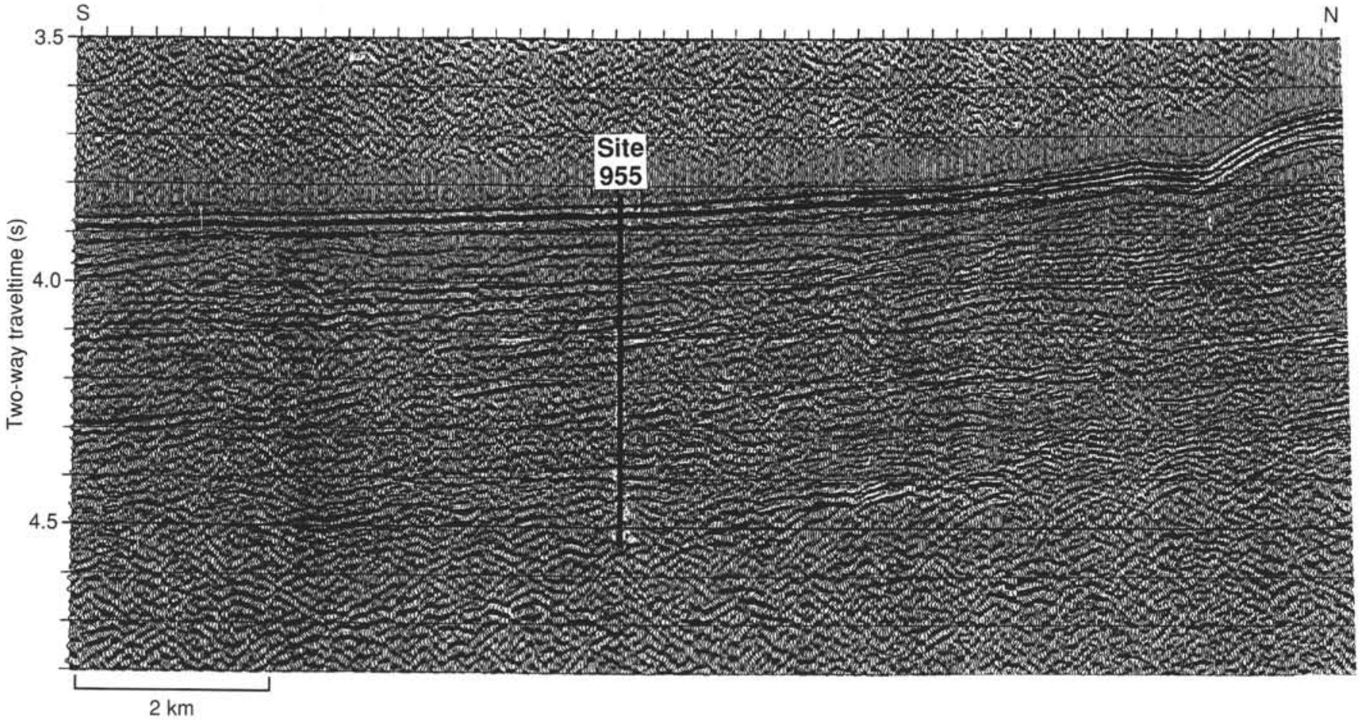

Figure 1. Processed seismic profile acquired during approach to Site 955.

Unit D is wedge-shaped with southward decreasing thickness. The base, which can only be identified in the southern part of the profile, is nearly horizontal at ~4.35 s. The thickness is estimated at ~350 ms in the northern end of the profile and 100 ms in the southern end. The unit is relatively transparent with only a few coherent reflectors. Internal reflectors downlap onto the horizontal base, thus indicating a depositional unit prograding from a northern source area, most likely Gran Canaria.

Unit E has an approximately even thickness of 100 ms. Internal reflectors are wavy. Amplitude variations are considerable. Internal reflector terminations are numerous. Reflectors onlap or downlap onto the southward inclined surface of the basement reflector.

At Site 955 an excellent sonic log was measured. Together with velocity data from the MST a complete velocity function from seafloor to 575 mbsf was obtained allowing a precise transformation of two-way traveltimes to depths (Fig. 3). The depths of the seismic units at Site 955 was calculated as follows: Unit A: 0–140 mbsf, Unit B: 140–170 mbsf, Unit C: 170–270 mbsf, Unit D: 270–420 mbsf, and Unit E: 420–525 mbsf as indicated on Figure 2.

On a large scale there is a good agreement between the stratigraphic and lithologic interpretations of the cores and the depositional architecture as derived from the seismic profile. Two major sequences can be discerned in the seismic profile, namely an upper comprising Units A, B, and C, and a lower comprising Units D and E. The upper sequence, characterized by basinward thickening units and pronounced lateral change in seismic facies, corresponds to the Pliocene–Pleistocene deposits in lithostratigraphic Units I and II. The lower sequence, which is thinning basinward, corresponds to the middle–upper Miocene lithologic Units III and IV. The transition from seismic Unit D to E seems to mark the middle/upper Miocene boundary. The acoustic basement (i.e., the base of Unit E) corresponds the top of the lower volcanic sands (lithologic Subunit IVb) tentatively correlated to the Mogan formation on the island.

OPERATIONS

Site 954 to Site 955 (VICAP-4) Transit

The 64 nmi transit from Site 954 to Site 955 was accomplished in 6 hr. During the short cruise, the vessel passed within 4 nmi of the city of Las Palmas on Grand Canary Island. At 0230, local time, 9 September, the vessel slowed to 6 kt and the seismic gear was deployed as the vessel approached the survey area. After a 2 hr survey, the gear was retrieved and the vessel returned to the site. A beacon was deployed at 0531, 9 September.

Hole 955A

An APC/XCB BHA was made up and Core 157-955A-1H was shot, establishing the mud line depth at 2854.2 mbsl (Table 1). Cores 1H to 18H advanced to 168.9 mbsf and recovered 177.1 m (104.9% recovery). The cores were oriented starting with Core 3H. Heat flow measurements were made on Cores 3H, 6H, 9H, and 12H. The last piston core (18H) did not stroke out fully and it was decided to continue with the XCB system. XCB coring deepened the hole to 599.4 mbsf with 82.9% recovery. Total recovery for the hole was 89.1%. During coring, many of the cores were charged with gas, requiring the drilling of small holes to relieve pressure and prevent sediment from expanding out the ends of the core liner. Headspace analysis measured methane as high as 36,000 ppm (8 ppm ethane at 158 mbsf). The ratio of methane to ethane stayed in the range of 3000–4000. No heavier hydrocarbons were detected. Coring conditions were excellent with no abnormal pressure or torque problems.

At 1645, 12 September, coring terminated at a depth of 599.4 mbsf after having achieved all objectives for this site. The hole was swept with a 50 bbl sepiolite flush and a wiper trip was conducted with no drag registered. 12 m of soft fill at the bottom of the hole was quickly washed and reamed to bottom (599.4 mbsf). The bit was pulled up to the logging depth of 103 mbsf.

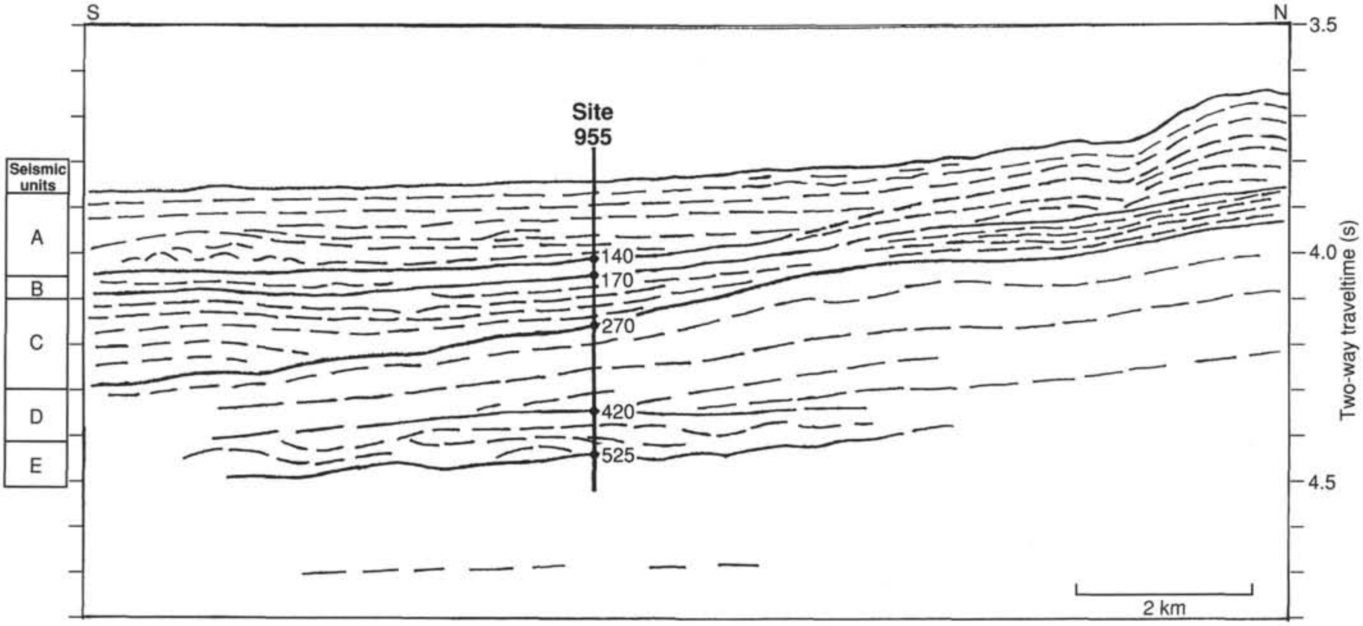

Figure 2. Seismic-stratigraphic interpretation of the seismic profile at Site 955. Depths (mbsf) to the unit boundaries are given at Site 955.

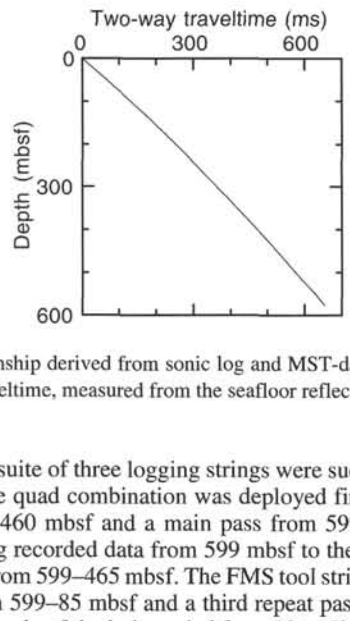

Figure 3. Relationship derived from sonic log and MST-data between depth and two-way traveltime, measured from the seafloor reflector.

A complete suite of three logging strings were successfully run at Hole 955A. The quad combination was deployed first and recorded data from 599–460 mbsf and a main pass from 599–72 mbsf. The geochemical log recorded data from 599 mbsf to the mud line and a repeat section from 599–465 mbsf. The FMS tool string recorded two full passes from 599–85 mbsf and a third repeat pass from 599–390 mbsf. The dip angle of the hole varied from 2° to 5°.

At 2330, 13 September, the logging equipment was rigged down. The pipe was pulled out of the hole with the bit clearing the seafloor at 2350 and was on deck at 0455, 14 September. The vessel was underway for the next location by 0515, 14 September.

LITHOSTRATIGRAPHY

The sedimentary succession recovered at Site 955 is 599 m thick and consists of abundant fine-grained hemipelagic sediments that are interbedded in the lower part of the sequence with volcaniclastic material (Fig. 4). The age of the sequence ranges from Pleistocene to middle Miocene. In the upper part of the sequence the dominant lithology is clayey nannofossil mixed sediment with foraminifers, with minor interbeds of clayey quartz silt and sand, and rare interbeds of pumice sand and ash. The upper part of the sequence at Site 955 differs significantly from that found at Sites 953 and 954 by having an abundance of quartz-rich sands derived from the northwest African continental margin. Volcaniclastic material from Gran Canaria dominates in the lower part of the sequence. Downhole variations in the abundance and lithology of the sand layers (Fig. 5) have been used as an important criteria for the subdivision of the sequence into five major units with four subunits.

Calcium carbonate concentrations for sediments at Site 955 vary with depth (Fig. 6). Calcium carbonate contents for the hemipelagic sediments from 0 to 270 mbsf (Units I, II, and III) are mostly between 40 and 60 wt% $CaCO_3$. The $CaCO_3$ contents decrease significantly and are typically in the range 20–40 wt% $CaCO_3$ from 270 to 460 mbsf (Units III and IVa). $CaCO_3$ contents increase from 460 to 595 mbsf (Units IVb and V) and range from 30 to 65 wt%. Calcium carbonate data for silt and sand interbeds in the upper part of the sequence (Unit I) show both higher and lower $CaCO_3$ contents than the hemipelagic sediments. From 340 to 500 mbsf (Units III and IVa) silt and sand interbeds have $CaCO_3$ contents of 10–30 wt%, which is similar to the range for hemipelagic sediments in this depth interval.

Unit I

Interval: Sections 157-955A-1H-1 to 157-955C-23X-1
Depth: 0–207 mbsf
Age: Pleistocene to late Pliocene

Unit I is 207 m thick and the dominant lithology is clayey nannofossil mixed sediment with foraminifers interbedded with gray, clayey quartz silt, and sand (mainly thin to very thin bedded). Unit I is subdivided into two subunits based on the frequency of slumped sediment sequences, the presence of dispersed shallow-water shell debris, and the thickness of siliciclastic sediments emplaced by gravity flows.

Subunit Ia

Interval: Sections 157-955A-1H-1 to 157-955A-19X-4
Depth: 0–175 mbsf

Table 1. Coring summary, Site 955.

Core	Date (August 1994)	Time (UTC)	Sub-bottom (m) Top	Sub-bottom (m) Bottom	Cored (m)	Recovered (m)	Recovery (%)	Section	Length (m)	Depth (mbsf) Top	Depth (mbsf) Bottom	Samples
157-955A-												
1H	8	1235	0.0	8.1	8.1	8.14	100.0					
								1	1.50	0.00	1.50	
								2	1.50	1.50	3.00	
								3	1.50	3.00	4.50	
								4	1.50	4.50	6.00	IW 145–150
								5	1.50	6.00	7.50	HS 0–5
								6	0.40	7.50	7.90	
								CC	0.24	7.90	8.14	
2H	8	1330	8.1	17.6	9.5	9.84	103.0					
								1	1.50	8.10	9.60	
								2	1.50	9.60	11.10	
								3	1.50	11.10	12.60	
								4	1.50	12.60	14.10	IW 145–150
								5	1.50	14.10	15.60	HS 0–5
								6	1.50	15.60	17.10	
								7	0.58	17.10	17.68	
								CC	0.26	17.68	17.94	
3H	8	1445	17.6	27.1	9.5	10.11	106.4					
								1	1.50	17.60	19.10	
								2	1.50	19.10	20.60	
								3	1.50	20.60	22.10	
								4	1.50	22.10	23.60	IW 145–150
								5	1.50	23.60	25.10	HS 0–5
								6	1.50	25.10	26.60	
								7	0.75	26.60	27.35	
								CC	0.36	27.35	27.71	
4H	8	1535	27.1	36.6	9.5	9.94	104.0					
								1	1.50	27.10	28.60	
								2	1.50	28.60	30.10	
								3	1.50	30.10	31.60	
								4	1.50	31.60	33.10	IW 145–150
								5	1.50	33.10	34.60	HS 0–5
								6	1.50	34.60	36.10	
								7	0.65	36.10	36.75	
								CC	0.29	36.75	37.04	
5H	8	1630	36.6	46.1	9.5	9.94	104.0					
								1	1.50	36.60	38.10	
								2	1.50	38.10	39.60	
								3	1.50	39.60	41.10	
								4	1.50	41.10	42.60	IW 145–150
								5	1.50	42.60	44.10	HS 0–5
								6	1.50	44.10	45.60	
								7	0.67	45.60	46.27	
								CC	0.27	46.27	46.54	
6H	9	1735	46.1	55.6	9.5	10.05	105.8					
								1	1.50	46.10	47.60	
								2	1.50	47.60	49.10	
								3	1.50	49.10	50.60	
								4	1.50	50.60	52.10	IW 145–150
								5	1.50	52.10	53.60	HS 0–5
								6	1.50	53.60	55.10	
								7	0.70	55.10	55.80	
								CC	0.35	55.80	56.15	
7H	9	1825	55.6	65.1	9.5	10.20	107.3					
								1	1.50	55.60	57.10	
								2	1.50	57.10	58.60	
								3	1.50	58.60	60.10	
								4	1.50	60.10	61.60	IW 145–150
								5	1.50	61.60	63.10	HS 0–5
								6	1.50	63.10	64.60	
								7	0.76	64.60	65.36	
								CC	0.44	65.36	65.80	
8H	9	1915	65.1	74.6	9.5	10.03	105.6					
								1	1.50	65.10	66.60	
								2	1.50	66.60	68.10	
								3	1.50	68.10	69.60	
								4	1.50	69.60	71.10	IW 145–150
								5	1.50	71.10	72.60	HS 0–5
								6	1.50	72.60	74.10	
								7	0.82	74.10	74.92	
								CC	0.21	74.92	75.13	
9H	9	2035	74.6	84.1	9.5	10.37	109.1					
								1	1.50	74.60	76.10	
								2	1.50	76.10	77.60	
								3	1.50	77.60	79.10	
								4	1.50	79.10	80.60	IW 145–150
								5	1.50	80.60	82.10	HS 0–5
								6	1.50	82.10	83.60	
								7	0.76	83.60	84.36	
								CC	0.61	84.36	84.97	0–14 cm unoriented
10H	9	2130	84.1	93.6	9.5	9.96	105.0					
								1	1.50	84.10	85.60	
								2	1.50	85.60	87.10	
								3	1.50	87.10	88.60	
								4	1.50	88.60	90.10	IW 145–150
								5	1.50	90.10	91.60	HS 0–5
								6	1.50	91.60	93.10	

Table 1 (continued).

Core	Date (August 1994)	Time (UTC)	Sub-bottom (m) Top	Sub-bottom (m) Bottom	Cored (m)	Recovered (m)	Recovery (%)	Section	Length (m)	Depth (mbsf) Top	Depth (mbsf) Bottom	Samples
								7	0.63	93.10	93.73	
								CC	0.33	93.73	94.06	
11H	9	2230	93.6	103.1	9.5	9.79	103.0					
								1	1.50	93.60	95.10	
								2	1.50	95.10	96.60	
								3	1.50	96.60	98.10	
								4	1.50	98.10	99.60	
								5	1.50	99.60	101.10	HS 0–5
								6	1.50	101.10	102.60	
								7	0.48	102.60	103.08	
								CC	0.31	103.08	103.39	
12H	9	2340	103.1	112.6	9.5	10.03	105.6					
								1	1.50	103.10	104.60	
								2	1.50	104.60	106.10	
								3	1.50	106.10	107.60	
								4	1.50	107.60	109.10	IW 145–150
								5	1.50	109.10	110.60	HS 0–5
								6	1.50	110.60	112.10	
								7	0.57	112.10	112.67	
								CC	0.46	112.67	113.13	
13H	10	0030	112.6	122.1	9.5	9.99	105.0					
								1	1.50	112.60	114.10	
								2	1.50	114.10	115.60	
								3	1.50	115.60	117.10	
								4	1.50	117.10	118.60	
								5	1.50	118.60	120.10	
								6	1.50	120.10	121.60	HS 0–5
								7	0.69	121.60	122.29	
								CC	0.30	122.29	122.59	
14H	10	0115	122.1	131.6	9.5	10.00	105.2					
								1	1.50	122.10	123.60	
								2	1.50	123.60	125.10	
								3	1.50	125.10	126.60	
								4	1.50	126.60	128.10	IW 145–150
								5	1.50	128.10	129.60	HS 0–5
								6	1.50	129.60	131.10	
								7	0.71	131.10	131.81	
								CC	0.29	131.81	132.10	
15H	10	0200	131.6	141.1	9.5	9.97	105.0					
								1	1.50	131.60	133.10	
								2	1.50	133.10	134.60	
								3	1.50	134.60	136.10	
								4	1.50	136.10	137.60	
								5	1.50	137.60	139.10	
								6	1.50	139.10	140.60	HS 0–5
								7	0.64	140.60	141.24	
								CC	0.33	141.24	141.57	
16H	10	0250	141.1	150.6	9.5	9.95	105.0					
								1	1.55	141.10	142.65	
								2	1.50	142.65	144.15	
								3	1.50	144.15	145.65	
								4	1.50	145.65	147.15	
								5	1.50	147.15	148.65	IW 145–150
								6	1.50	148.65	150.15	HS 0–5
								7	0.69	150.15	150.84	
								CC	0.26	150.84	151.10	
17H	10	0345	150.6	160.1	9.5	10.01	105.3					
								1	1.50	150.60	152.10	
								2	1.50	152.10	153.60	
								3	1.50	153.60	155.10	
								4	1.50	155.10	156.60	
								5	1.50	156.60	158.10	
								6	1.50	158.10	159.60	HS 0–5
								7	0.72	159.60	160.32	
								CC	0.29	160.32	160.61	
18H	10	0435	160.1	168.9	8.8	8.80	100.0					
								1	1.50	160.10	161.60	
								2	1.50	161.60	163.10	
								3	1.50	163.10	164.60	
								4	1.50	164.60	166.10	HS 0–5
								5	1.50	166.10	167.60	
								6	0.82	167.60	168.42	
								CC	0.48	168.42	168.90	
19X	10	0540	168.9	176.4	7.5	9.74	130.0					
								1	1.50	168.90	170.40	
								2	1.50	170.40	171.90	
								3	1.50	171.90	173.40	
								4	1.50	173.40	174.90	
								5	1.50	174.90	176.40	
								6	1.50	176.40	177.90	
								7	0.36	177.90	178.26	
								CC	0.38	178.26	178.64	
20X	10	0630	176.4	186.0	9.6	8.28	86.2					
								1	1.50	176.40	177.90	
								2	1.50	177.90	179.40	
								3	1.50	179.40	180.90	
								4	1.50	180.90	182.40	
								5	1.55	182.40	183.95	IW 150–155
								6	0.53	183.95	184.48	HS 0–5

Table 1 (continued).

Core	Date (August 1994)	Time (UTC)	Sub-bottom (m) Top	Sub-bottom (m) Bottom	Cored (m)	Recovered (m)	Recovery (%)	Section	Length (m)	Depth (mbsf) Top	Depth (mbsf) Bottom	Samples
								CC	0.20	184.48	184.68	
21X	10	0715	186.0	195.5	9.5	3.16	33.2					
								1	1.50	186.00	187.50	
								2	1.50	187.50	189.00	HS 0–5
								CC	0.16	189.00	189.16	
22X	10	0805	195.5	205.1	9.6	8.35	87.0					
								1	1.50	195.50	197.00	
								2	1.50	197.00	198.50	
								3	1.50	198.50	200.00	
								4	1.50	200.00	201.50	
								5	1.50	201.50	203.00	HS 0–5
								6	0.57	203.00	203.57	
								CC	0.28	203.57	203.85	
23X	10	0850	205.1	214.6	9.5	4.27	44.9					
								1	1.50	205.10	206.60	
								2	1.50	206.60	208.10	IW 140–150
								3	1.04	208.10	209.14	HS 0–5
								CC	0.23	209.14	209.37	
24X	10	0945	214.6	224.3	9.7	6.81	70.2					
								1	1.50	214.60	216.10	
								2	1.50	216.10	217.60	
								3	1.50	217.60	219.10	
								4	1.50	219.10	220.60	HS 0–5
								5	0.40	220.60	221.00	
								CC	0.41	221.00	221.41	
25X	10	1040	224.3	234.0	9.7	9.84	101.0					
								1	1.50	224.30	225.80	
								2	1.50	225.80	227.30	
								3	1.50	227.30	228.80	
								4	1.50	228.80	230.30	
								5	1.50	230.30	231.80	
								6	1.50	231.80	233.30	HS 0–5
								7	0.55	233.30	233.85	
								CC	0.29	233.85	234.14	
26X	10	1125	234.0	243.6	9.6	9.91	103.0					
								1	1.50	234.00	235.50	
								2	1.50	235.50	237.00	
								3	1.50	237.00	238.50	
								4	1.50	238.50	240.00	
								5	1.50	240.00	241.50	IW 140–150
								6	1.50	241.50	243.00	HS 0–5
								7	0.59	243.00	243.59	
								CC	0.32	243.59	243.91	
27X	10	1215	243.6	253.3	9.7	8.05	83.0					
								1	1.50	243.60	245.10	
								2	1.50	245.10	246.60	
								3	1.50	246.60	248.10	
								4	1.50	248.10	249.60	
								5	1.50	249.60	251.10	HS 0–5
								6	0.34	251.10	251.44	
								CC	0.21	251.44	251.65	
28X	10	1310	253.3	263.0	9.7	10.10	104.1					
								1	1.50	253.30	254.80	
								2	1.50	254.80	256.30	
								3	1.50	256.30	257.80	
								4	1.50	257.80	259.30	
								5	1.50	259.30	260.80	HS 0–5
								6	1.50	260.80	262.30	
								7	0.57	262.30	262.87	
								CC	0.53	262.87	263.40	
29X	10	1410	263.0	272.7	9.7	9.87	102.0					
								1	1.50	263.00	264.50	
								2	1.50	264.50	266.00	
								3	1.50	266.00	267.50	
								4	1.50	267.50	269.00	IW 140–150
								5	1.50	269.00	270.50	HS 0–5
								6	1.50	270.50	272.00	
								7	0.57	272.00	272.57	
								CC	0.30	272.57	272.87	
30X	10	1510	272.7	282.2	9.5	9.90	104.0					
								1	1.50	272.70	274.20	
								2	1.50	274.20	275.70	
								3	1.50	275.70	277.20	
								4	1.50	277.20	278.70	HS 0–5
								5	1.50	278.70	280.20	
								6	1.50	280.20	281.70	
								7	0.52	281.70	282.22	
								CC	0.38	282.22	282.60	
31X	10	1615	282.2	291.7	9.5	9.27	97.6					
								1	1.50	282.20	283.70	
								2	1.50	283.70	285.20	
								3	1.50	285.20	286.70	
								4	1.50	286.70	288.20	
								5	1.50	288.20	289.70	HS 0–5
								6	1.39	289.70	291.09	
								CC	0.38	291.09	291.47	
32X	10	1725	291.7	301.2	9.5	9.97	105.0					
								1	1.50	291.70	293.20	
								2	1.50	293.20	294.70	
								3	1.50	294.70	296.20	

Table 1 (continued).

Core	Date (August 1994)	Time (UTC)	Sub-bottom (m) Top	Sub-bottom (m) Bottom	Cored (m)	Recovered (m)	Recovery (%)	Section	Length (m)	Depth (mbsf) Top	Depth (mbsf) Bottom	Samples
								4	1.50	296.20	297.70	IW 140–150
								5	1.50	297.70	299.20	HS 0–5
								6	1.50	299.20	300.70	
								7	0.46	300.70	301.16	
								CC	0.51	301.16	301.67	
33X	10	1840	301.2	310.8	9.6	9.92	103.0					
								1	1.50	301.20	302.70	
								2	1.50	302.70	304.20	
								3	1.50	304.20	305.70	
								4	1.50	305.70	307.20	
								5	1.50	307.20	308.70	HS 0–5
								6	1.50	308.70	310.20	
								7	0.58	310.20	310.78	
								CC	0.34	310.78	311.12	
34X	10	1955	310.8	320.4	9.6	9.81	102.0					
								1	1.50	310.80	312.30	
								2	1.50	312.30	313.80	
								3	1.50	313.80	315.30	
								4	1.50	315.30	316.80	HS 0–5
								5	1.50	316.80	318.30	
								6	1.50	318.30	319.80	
								7	0.50	319.80	320.30	
								CC	0.31	320.30	320.61	
35X	10	2110	320.4	330.1	9.7	9.96	102.0					
								1	0.28	320.40	320.68	
								2	1.50	320.68	322.18	
								3	1.50	322.18	323.68	
								4	1.50	323.68	325.18	IW 140–150
								5	1.27	325.18	326.45	HS 0–5
								6	1.50	326.45	327.95	
								7	1.50	327.95	329.45	
								8	0.49	329.45	329.94	
								CC	0.42	329.94	330.36	
36X	10	2210	330.1	339.6	9.5	9.90	104.0					
								1	1.50	330.10	331.60	
								2	1.50	331.60	333.10	
								3	1.50	333.10	334.60	
								4	1.50	334.60	336.10	
								5	1.50	336.10	337.60	HS 0–5
								6	1.50	337.60	339.10	
								7	0.49	339.10	339.59	
								CC	0.41	339.59	340.00	
37X	10	2320	339.6	349.1	9.5	9.61	101.0					
								1	1.50	339.60	341.10	
								2	1.50	341.10	342.60	
								3	1.50	342.60	344.10	
								4	1.50	344.10	345.60	
								5	1.50	345.60	347.10	HS 0–5
								6	1.50	347.10	348.60	
								7	0.23	348.60	348.83	
								CC	0.38	348.83	349.21	
38X	11	0020	349.1	358.7	9.6	9.80	102.0					
								1	1.50	349.10	350.60	
								2	1.50	350.60	352.10	
								3	1.50	352.10	353.60	
								4	1.50	353.60	355.10	
								5	1.50	355.10	356.60	IW 140–150
								6	1.50	356.60	358.10	HS 0–5
								7	0.41	358.10	358.51	
								CC	0.39	358.51	358.90	
39X	11	0125	358.7	368.3	9.6	9.72	101.0					
								1	1.50	358.70	360.20	
								2	1.50	360.20	361.70	
								3	1.50	361.70	363.20	
								4	1.50	363.20	364.70	
								5	1.50	364.70	366.20	
								6	1.50	366.20	367.70	HS 0–5
								7	0.36	367.70	368.06	
								CC	0.36	368.06	368.42	
40X	11	0220	368.3	377.9	9.6	9.44	98.3					
								1	1.50	368.30	369.80	
								2	1.50	369.80	371.30	
								3	1.50	371.30	372.80	
								4	1.50	372.80	374.30	
								5	1.50	374.30	375.80	
								6	1.46	375.80	377.26	HS 0–5
								CC	0.48	377.26	377.74	
41X	11	0315	377.9	387.5	9.6	8.92	92.9					
								1	1.50	377.90	379.40	
								2	1.50	379.40	380.90	
								3	1.50	380.90	382.40	
								4	1.50	382.40	383.90	
								5	1.50	383.90	385.40	IW 140–150
								6	1.19	385.40	386.59	HS 0–5
								CC	0.23	386.59	386.82	
42X	11	0420	387.5	397.2	9.7	9.45	97.4					
								1	1.50	387.50	389.00	
								2	1.50	389.00	390.50	
								3	1.50	390.50	392.00	
								4	1.50	392.00	393.50	

Table 1 (continued).

Core	Date (August 1994)	Time (UTC)	Sub-bottom (m) Top	Sub-bottom (m) Bottom	Cored (m)	Recovered (m)	Recovery (%)	Section	Length (m)	Depth (mbsf) Top	Depth (mbsf) Bottom	Samples
								5	1.50	393.50	395.00	
								6	1.50	395.00	396.50	HS 0–5
								CC	0.45	396.50	396.95	
43X	11	0520	397.2	406.8	9.6	1.32	13.7					
								1	1.00	397.20	398.20	
								CC	0.32	398.20	398.52	
44X	11	0630	406.8	416.5	9.7	8.87	91.4					
								1	1.50	406.80	408.30	
								2	1.50	408.30	409.80	
								3	1.50	409.80	411.30	
								4	1.50	411.30	412.80	
								5	1.50	412.80	414.30	IW 135–150
								6	0.88	414.30	415.18	HS 0–5
								CC	0.49	415.18	415.67	
45X	11	0800	416.5	426.2	9.7	6.14	63.3					
								1	1.50	416.50	418.00	
								2	1.50	418.00	419.50	
								3	1.50	419.50	421.00	
								4	1.30	421.00	422.30	HS 0–5
								CC	0.34	422.30	422.64	
46X	11	0925	426.2	435.8	9.6	7.85	81.8					
								1	1.50	426.20	427.70	
								2	1.50	427.70	429.20	
								3	1.50	429.20	430.70	
								4	1.50	430.70	432.20	
								5	1.50	432.20	433.70	HS 0–5
								CC	0.35	433.70	434.05	
47X	11	1105	435.8	445.5	9.7	9.51	98.0					
								1	1.50	435.80	437.30	
								2	1.50	437.30	438.80	
								3	1.50	438.80	440.30	
								4	1.50	440.30	441.80	
								5	1.50	441.80	443.30	IW 135–150
								6	1.50	443.30	444.80	HS 0–5
								CC	0.51	444.80	445.31	
48X	11	1305	445.5	455.2	9.7	8.91	91.8					
								1	1.50	445.50	447.00	
								2	1.50	447.00	448.50	
								3	1.50	448.50	450.00	
								4	1.50	450.00	451.50	
								5	1.50	451.50	453.00	HS 0–5
								6	1.05	453.00	454.05	
								CC	0.36	454.05	454.41	
49X	11	1500	455.2	464.8	9.6	9.65	100.0					
								1	1.50	455.20	456.70	
								2	1.50	456.70	458.20	
								3	1.50	458.20	459.70	
								4	1.50	459.70	461.20	
								5	1.50	461.20	462.70	HS 0–5
								6	1.50	462.70	464.20	
								CC	0.65	464.20	464.85	
50X	11	1645	464.8	474.4	9.6	7.12	74.1					
								1	1.50	464.80	466.30	
								2	1.50	466.30	467.80	
								3	1.50	467.80	469.30	IW 135–150
								4	1.50	469.30	470.80	HS 0–5
								5	0.77	470.80	471.57	
								CC	0.35	471.57	471.92	
51X	11	1845	474.4	484.1	9.7	9.69	99.9					
								1	1.50	474.40	475.90	
								2	1.50	475.90	477.40	
								3	1.50	477.40	478.90	
								4	1.50	478.90	480.40	
								5	1.50	480.40	481.90	HS 0–5
								6	1.50	481.90	483.40	
								7	0.34	483.40	483.74	
								CC	0.35	483.74	484.09	
52X	11	2030	484.1	493.8	9.7	3.77	38.8					
								1	1.50	484.10	485.60	
								2	1.50	485.60	487.10	HS 0–5
								3	0.45	487.10	487.55	
								CC	0.32	487.55	487.87	
53X	11	2155	493.8	503.4	9.6	5.51	57.4					
								1	1.50	493.80	495.30	
								2	1.50	495.30	496.80	IW 135–150 HS 130–135
								3	1.50	496.80	498.30	
								4	0.70	498.30	499.00	
								CC	0.31	499.00	499.31	
54X	11	2335	503.4	512.9	9.5	0.21	2.2					
								CC	0.21	503.40	503.61	
55X	12	0100	512.9	522.4	9.5	5.13	54.0					
								1	1.50	512.90	514.40	
								2	1.50	514.40	515.90	
								3	1.50	515.90	517.40	HS 0–5
								4	0.34	517.40	517.74	
								CC	0.29	517.74	518.03	
56X	12	0220	522.4	532.0	9.6	4.94	51.4					
								1	1.50	522.40	523.90	
								2	1.50	523.90	525.40	IW 140–150

Table 1 (continued).

Core	Date (August 1994)	Time (UTC)	Sub-bottom (m) Top	Sub-bottom (m) Bottom	Cored (m)	Recovered (m)	Recovery (%)	Section	Length (m)	Depth (mbsf) Top	Depth (mbsf) Bottom	Samples
								3	1.50	525.40	526.90	HS 0–5
								4	0.42	526.90	527.32	
								CC	0.02	527.32	527.34	
57X	12	0340	532.0	541.6	9.6	9.69	101.0					
								1	1.50	532.00	533.50	
								2	1.50	533.50	535.00	
								3	1.50	535.00	536.50	
								4	1.50	536.50	538.00	
								5	1.50	538.00	539.50	
								6	1.50	539.50	541.00	HS 0–5
								CC	0.69	541.00	541.69	
58X	12	0505	541.6	551.2	9.6	7.58	78.9					
								1	1.50	541.60	543.10	
								2	1.50	543.10	544.60	
								3	1.50	544.60	546.10	
								4	1.50	546.10	547.60	
								5	1.21	547.60	548.81	HS 0–5
								CC	0.37	548.81	549.18	
59X	12	0630	551.2	560.9	9.7	9.34	96.3					
								1	1.50	551.20	552.70	
								2	1.50	552.70	554.20	
								3	1.50	554.20	555.70	
								4	1.50	555.70	557.20	
								5	1.50	557.20	558.70	IW 130–150
								6	1.41	558.70	560.11	HS 0–5
								CC	0.43	560.11	560.54	
60X	12	0810	560.9	570.5	9.6	7.66	79.8					
								1	1.50	560.90	562.40	
								2	1.50	562.40	563.90	
								3	1.50	563.90	565.40	
								4	1.50	565.40	566.90	
								5	1.30	566.90	568.20	HS 0–2
								CC	0.36	568.20	568.56	
61X	12	1000	570.5	580.2	9.7	4.11	42.4					
								1	1.50	570.50	572.00	
								2	1.50	572.00	573.50	HS 0–5
								3	0.76	573.50	574.26	
								CC	0.35	574.26	574.61	
62X	12	1235	580.2	589.8	9.6	10.26	106.9					
								1	0.39	580.20	580.59	
								2	1.50	580.59	582.09	
								3	1.50	582.09	583.59	
								4	1.50	583.59	585.09	
								5	1.23	585.09	586.32	HS 98–103/IW 103–123
								6	1.50	586.32	587.82	
								7	1.50	587.82	589.32	
								8	0.56	589.32	589.88	
								CC	0.58	589.88	590.46	
63X	12	1540	589.8	599.4	9.6	5.65	58.8					
								1	1.50	589.80	591.30	
								2	1.50	591.30	592.80	
								3	1.50	592.80	594.30	HS 0–5
								4	0.76	594.30	595.06	
								CC	0.39	595.06	595.45	
Coring Totals					599.4	534.08	89.10					

Notes: Hole 955A located at 27°19.546′N, 15°13.847′W. Water depth from sea surface = 2854.2 m. HS = headspace samples; IW = interstitial water samples.

Subunit Ia is composed of very thin bedded to massive clayey nannofossil mixed sediment with foraminifers and lesser amounts of clayey nannofossil ooze with foraminifers and nannofossil clay. MThese sediments range from green to pale green, and brown to pale brown, commonly with alternating thin to very thin laminations. The sediments are generally mottled and slightly to moderately bioturbated. Abundant, dispersed shallow marine shell fragments and complete shells as large as 2 cm are common, and small wood fragments are occasionally present. Smear slide analysis shows the dominant lithologies to be composed of coccolith plates and clay, with lesser amounts of foraminifers, and trace amounts of pyrite, quartz, feldspar, clinopyroxene, amphibole, and opaque minerals. In addition, siliceous microfossils occur in trace amounts in the upper part of the subunit (Sections 157-955A-1H-1 to 157-955A-1H-13). Calcium carbonate contents in these sediments vary from 20 to 80 wt% $CaCO_3$, with most values between 40 and 60 wt% (Fig. 6).

Minor lithologies in Subunit Ia occur as thin to very thin interbedded silt and sand that are often normally graded. In the upper part of the sequence (Cores 1H to 8H) these are mainly foraminifer silts and sands with variable quartz and lithic components. In the lower part (Cores 9H to 19X) they are dominantly dark gray clayey quartz silts and sands, sometimes pyrite-rich, with lesser amounts of foraminifers.

Minor fine- to coarse-grained volcaniclastic deposits consist of very thin beds of pumice sand in Sections 157-955A-2H-1 and 157-955A-2H-5, pumiceous ash in Section 157-955A-3H-5, and thin to very thin bedded vitric ash in Sections 157-955A-3H-6, 157-955A-6H-4, and 157-955A-13H-4. The ash layers, which are probably fall deposits from explosive volcanic eruptions, typically have sharp basal contacts and bioturbated tops (Fig. 7). They are composed dominantly of colorless, unaltered glass shards, with trace amounts of alkali feldspar, green clinopyroxene, and amphibole, together with variable proportions of biogenic material that has presumably been mixed in by bioturbation.

Soft sediment deformation and slump structures are common in most of the sediments in Subunit Ia especially in the intervals from

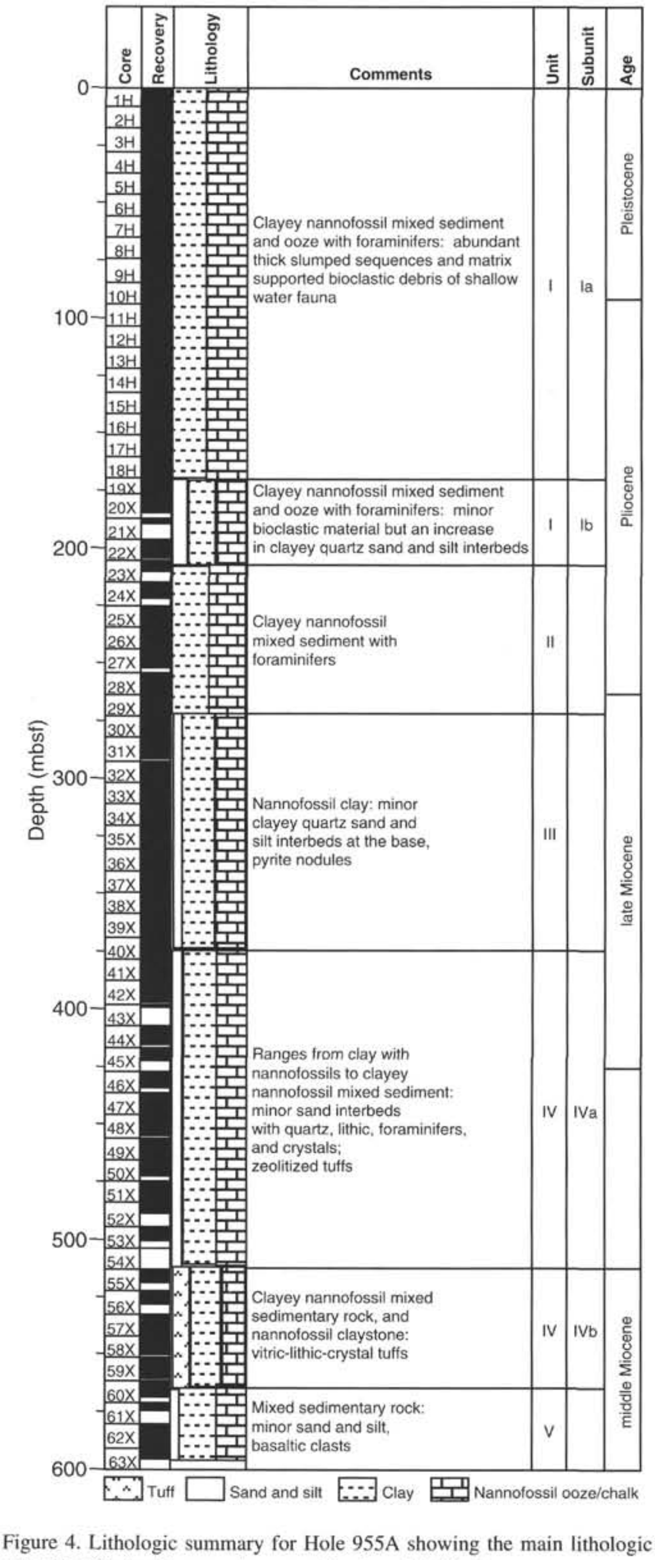

Figure 4. Lithologic summary for Hole 955A showing the main lithologic units identified with age and a generalized graphic lithology.

Cores 3H to 12H and 16H to 19X. They include convolute bedding, deformed and folded large mud clasts, slump folds, and microfaults (Figs. 8 and 9). Dispersed shell debris commonly occurs in the matrix between large mud clasts. The poor sorting of these shell-rich intervals suggests that they formed during slumping or debris flows through mixing of shallow marine-derived material and mobilized mud.

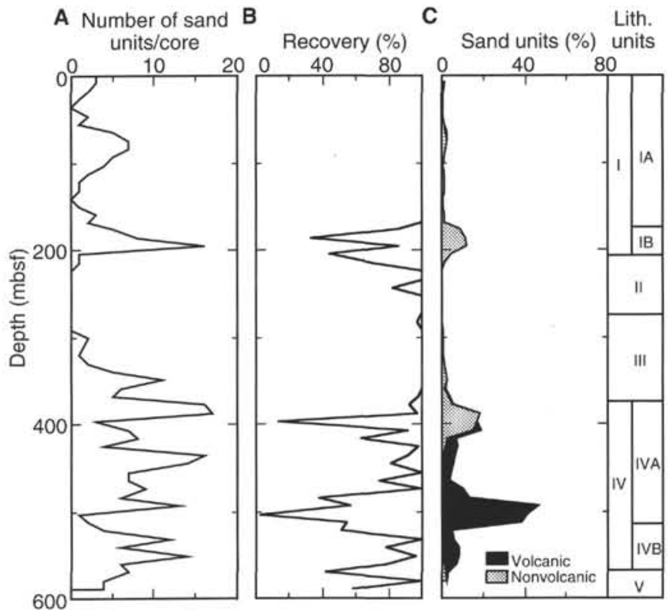

Figure 5. Variation in (**A**) the number of coarse (sand-sized) volcaniclastic layers per core, (**B**) the percentage recovery for each core, and (**C**) the total percentage of coarse volcaniclastic layers per core as a function of depth below seafloor.

Subunit Ib

Interval: Sections 157-955A-19X-5 to 157-955A-23X-1
Depth: 175–207 mbsf

Subunit Ib is 32 m thick and consists of medium to very thick bedded clayey nannofossil mixed sediment with medium to very thin interbeds of dark gray clayey quartz silt and sand with variable amounts of foraminifers. It is distinguished from Subunit Ia by the absence of dispersed shell debris, a decrease in the intensity of soft sediment deformation features, and an increase in the thickness and frequency of interbedded silt and sand (Fig. 5). The silt and sand beds are frequently disturbed by drilling, yet they sometimes show sharp bases, bioturbated tops, and normal grading. Calcium carbonate content of the hemipelagic sediment in Subunit Ib is slightly lower, on average, than that of Subunit Ia. The silt and sand beds contain 12–25 wt% $CaCO_3$, continuing the trend of decreasing $CaCO_3$ with increasing depth that was observed for Subunit Ia (Fig. 6). This trend probably reflects a decrease in the input of continental (siliciclastic) material through time.

Unit II

Interval: Sections 157-955A-23X-2 to 157-955A-29X-7
Depth: 207–273 mbsf
Age: early Pliocene to late Miocene

Unit II is 66 m thick and the dominant lithology is clayey nannofossil mixed sediment with foraminifers, together with lesser amounts of clayey nannofossil ooze with foraminifers and nannofossil clay. This unit is distinguished from Unit I by an almost complete absence of silt and sand interbeds (Fig. 5) and general lack of bedding. The sediments are pale green, gray, and brown, and massive and they are typically mottled. The sediments are composed mostly

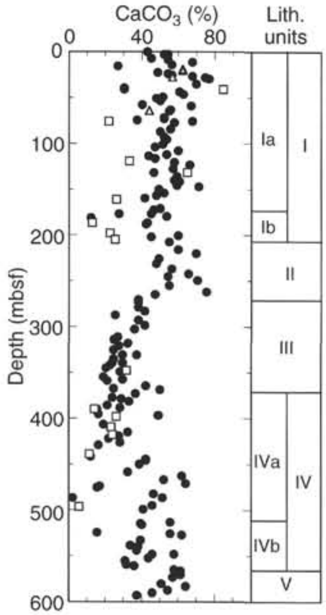

Figure 6. Variation in the calcium carbonate contents of hemipelagic sediments (filled circles), turbidite muds (open triangles), and silt or sand bases of turbidites (open squares) as a function of depth below seafloor, Hole 955A.

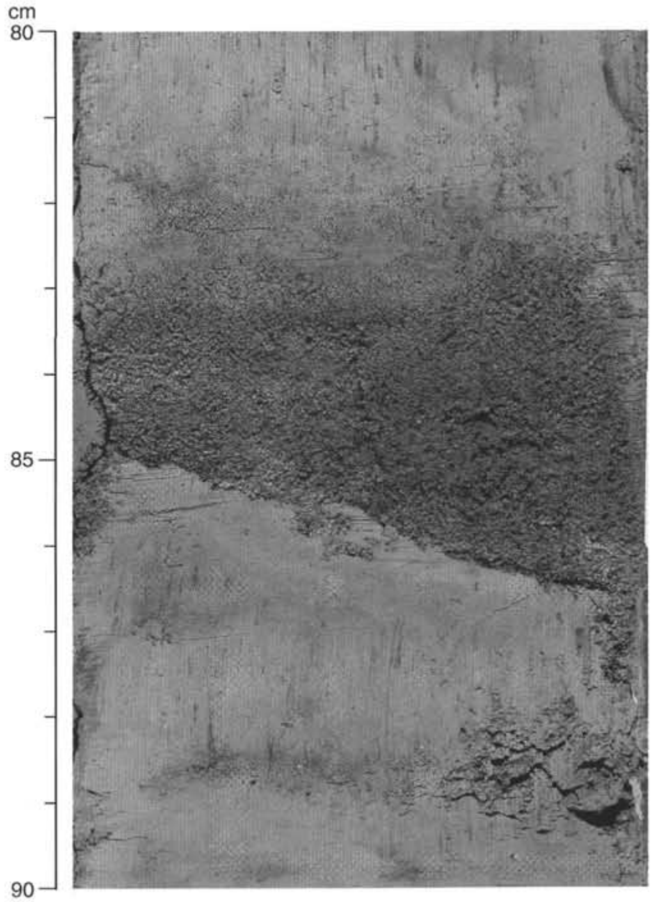

Figure 7. Ash fall layer from Subunit Ia composed of fresh, colorless glass shards. Note sharp base and bioturbated upper contact. Interval 157-955A-13H-4, 80–90 cm.

of coccolith plates, clay, and foraminifer tests, with trace amounts of pyrite, dolomite, calcareous grains, discoasters, iron oxides, feldspar, quartz, and green clinopyroxene. Disruption of the sediment by gas (methane) expansion is pervasive.

Rare interbeds in Unit II consist of gray very thin bedded clayey quartz-lithic sand in Sections 157-955A-24X-1 and 157-955A-24X-4, and clayey pyrite-foraminifer-quartz sand in Section 157-955A-29X-2.

Calcium carbonate contents of sediments in Unit II are similar to those in Unit I, generally between 40–60 wt% $CaCO_3$, with significant scatter toward higher values (Fig. 6).

Unit III

Interval: Sections 157-955A-29X-CC to 157-955A-40X-4
Depth: 273–374 mbsf
Age: late Miocene

Unit III is 101 m thick and is composed of thick bedded to structureless, brown to pale brown and gray nannofossil clay and less abundant clay with nannofossils interbedded with thin to very thin beds of clayey quartz silt and sand of variable foraminifer content. Unit III is distinguished from Unit II by an increase in clay content, a decrease in foraminifer content, and an increase in the abundance of small pyrite nodules and pyritized burrows. The upper contact of this unit also approximately corresponds to the Miocene/Pliocene boundary. Gas disruption of the cores of Unit III is much less compared with Unit II.

The sediments in this unit are generally structureless apart from persistent moderate mottling, probably largely bioturbation. They are composed dominantly of coccolith plates and clay with trace amounts of quartz, feldspar, and opaques.

Minor lithologies are mostly thin to very thin bedded, dark gray clayey quartz silt and sand layers, sometimes rich in pyrite, with variable proportions of foraminifers and other calcareous biogenic material. Gray medium bedded foraminifer sands with planar and cross laminations are also present.

Calcium carbonate contents of hemipelagic sediments in Unit III decrease with increasing depth from ~40 wt% $CaCO_3$ at the top of the unit to 20–30 wt% at the bottom (Fig. 6). The silt and sand interbeds have similarly low $CaCO_3$ contents (~30 wt%).

Unit IV

Interval: Sections 157-955A-40X-5 to 157-955A-60X-4
Depth: 374–567 mbsf
Age: late to middle Miocene

Unit IV is 193 m thick and contains a variety of lithologies composed of distinct volcaniclastic, siliciclastic, and pelagic components. The major lithologies are indurated nannofossil clay and clay with nannofossils interbedded with quartz-foraminifer-lithic silt and sand, zeolitized fine-grained tuff, vitric tuff with variable lithic and crystal contents, and pumice lapilli. Unit IV has been subdivided based on variations in the type and abundance of major volcaniclastic components.

Subunit IVa

Interval: Sections 157-955A-40X-5 to 157-955A-54X-CC
Depths: 374–513 mbsf

Subunit IVa is composed dominantly of thin to thick bedded, gray, green, and brown nannofossil clay, clayey nannofossil mixed sediment, and clay with nannofossils. It is distinguished from Unit III by a large increase in the frequency and thickness of nonvolcanic silt

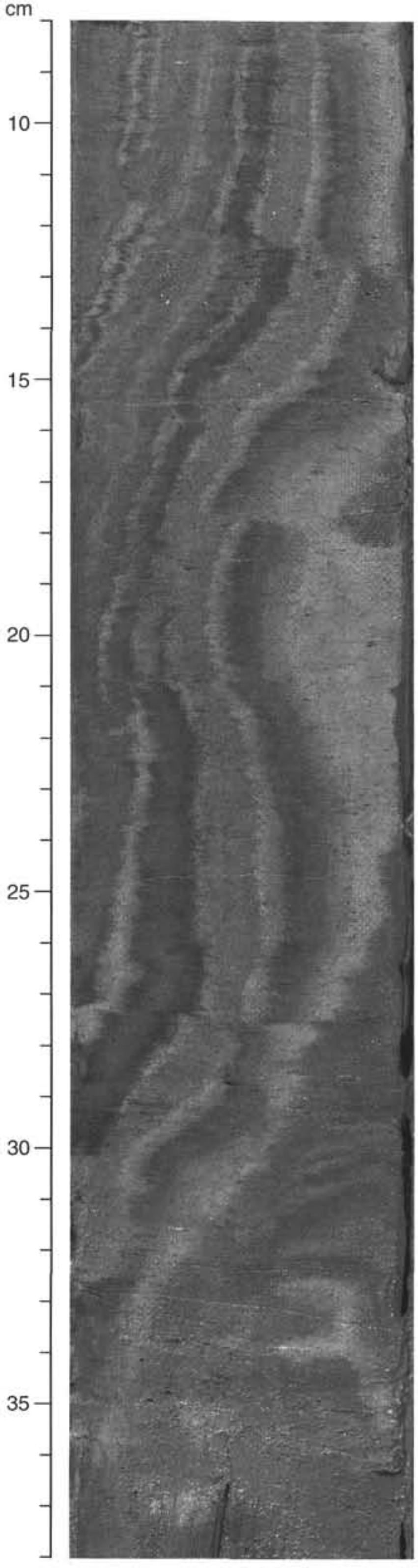

Figure 8. Soft sediment deformation features in Subunit Ia showing convolute, vertical bedding cut by several microfaults. Interval 157-955A-3H-1, 8–38 cm.

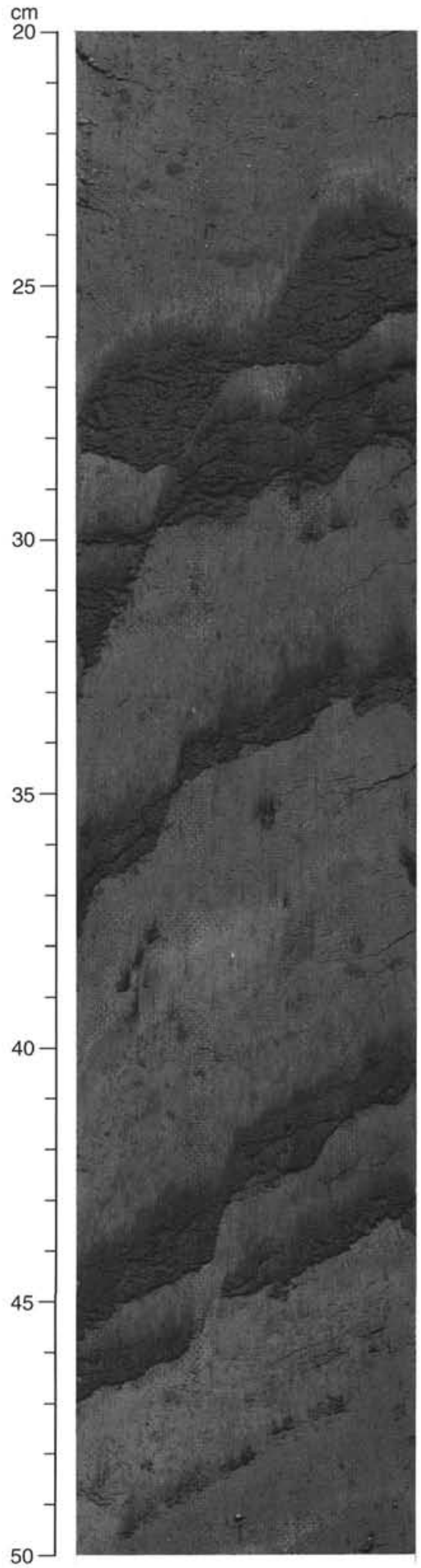

Figure 9. Very thin bedded sands disrupted by numerous microfaults in Subunit Ia. Interval 157-955A-11H-4, 20–50 cm.

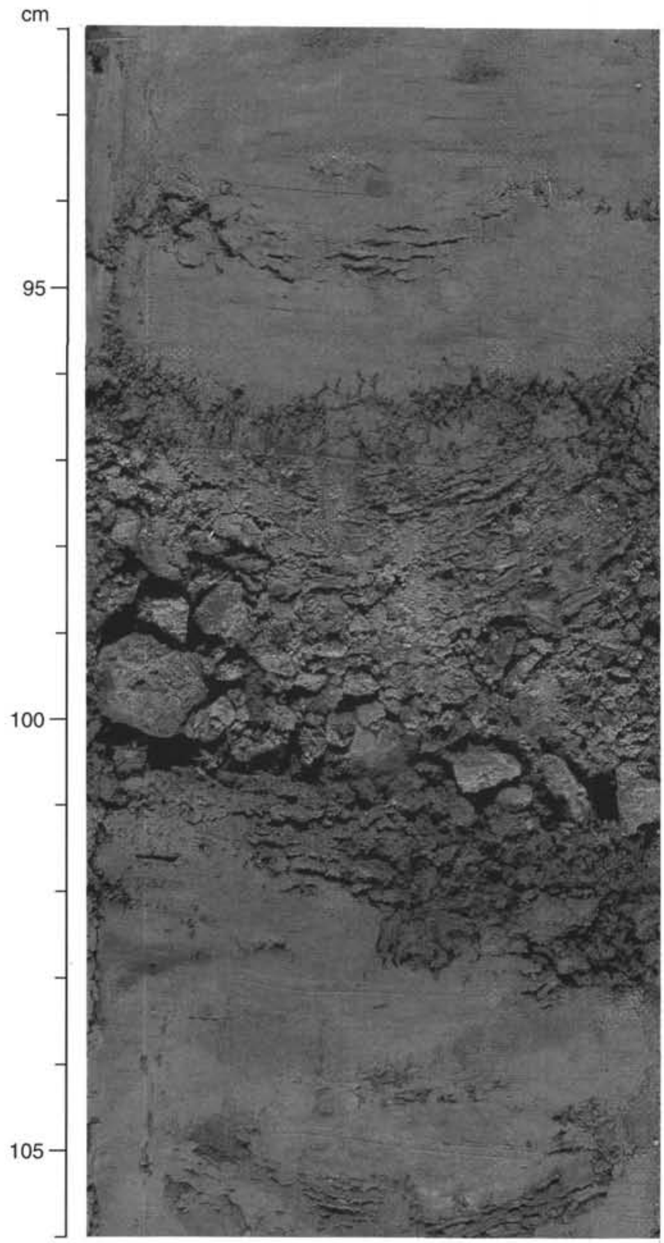

Figure 10. Fine-grained zeolitized tuff near the top of Subunit IVa showing an indurated layer above the sharp base and bioturbation of the upper contact. Interval 157-955A-40X-5, 92–106 cm.

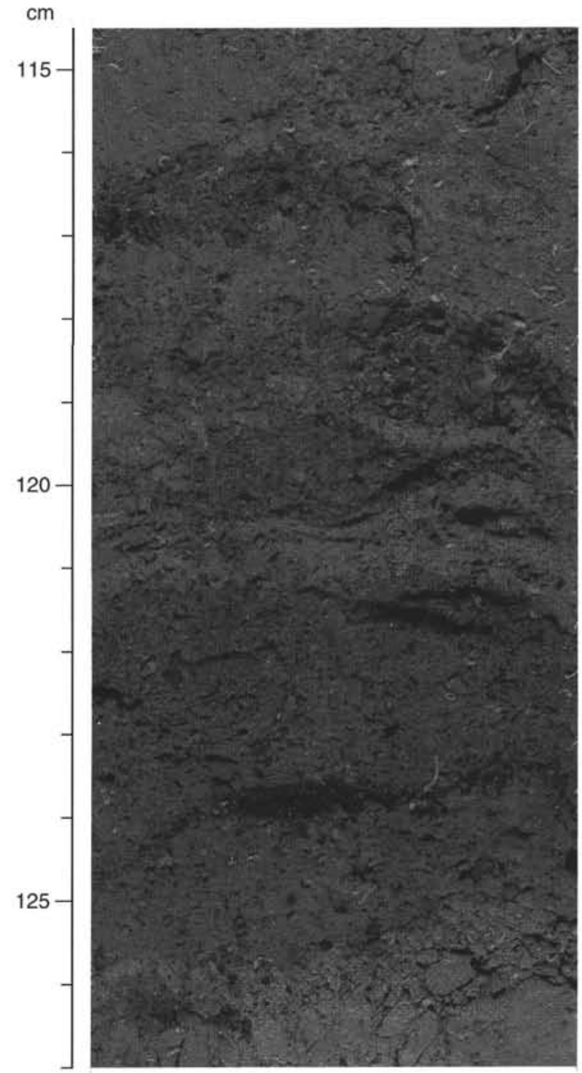

Figure 11. Vitric tuff in Subunit IVb showing dark green, fine-grained layers within coarser pumiceous tuff and strong bioturbation of the upper contact. This tuff contains phenocrysts of biotite and is equivalent to ignimbrite A on Gran Canaria. Interval 157-955A-58X-1, 114.5–127 cm.

and sand interbeds and the occurrence of zeolitized fine-grained tuffs (Fig. 5). Calcium carbonate contents of hemipelagic sediments in Subunit IVa range from 5 to 65 wt% $CaCO_3$ and increase with depth.

The coarse sediments are typically thin to medium bedded, with sharp bases and bioturbated upper contacts, and commonly they show normal grading. Lithologically they are dominantly clayey quartz silts and sands with variable proportions of foraminifers, crystals, and volcanic lithic fragments.

Volcaniclastic material occurs as thin interbeds within the dominant lithology. Thin bedded zeolitized tuffs occur in Sections 157-955A-40X-5, 157-955A-44X-3, 157-955A-45X-1, and 157-955A-45X-2, 157-955A-46X-1, 157-955A-50X-5, and 157-955A-50X-CC, and 157-955A-51X-1 to 157-955A-51X-4 (Fig. 10). The tuffs are composed mainly of fine-grained zeolite (phillipsite) with trace amounts of feldspar, green clinopyroxene, biotite, and amphibole. Some also contain coccolith plates and traces of quartz that were probably incorporated through bioturbation. The lower part of Subunit IVa (Cores 157-955A-52X to 157-955A-54X) is characterized by an increase in the thickness and frequency of coarse volcaniclastic sediments composed dominantly of lithics, crystals, and some pumice (Fig. 5).

Subunit IVb

Interval: Sections 157-955A-55X-1 to 157-955A-60X-4
Depth: 513–567 mbsf

Subunit IVb is 54 m thick and middle Miocene in age. It is composed of medium to very thick bedded, gray to pale green clayey nannofossil mixed sedimentary rock and nannofossil claystone interbedded with varied types of volcaniclastic sediment. It is distinguished from Subunit IVa by the abundance of vitric tuffs with variable but minor proportions of lithics and crystals, and by the absence of zeolitized tuffs. Calcium carbonate contents of hemipelagic sediments in Subunit IVb range from 30 to 65 wt%.

A distinctive feature of Subunit IVb is the presence of numerous interbeds of gray pumice lapilli, dark gray crystal ash, and green to olive green vitric tuff composed dominantly of colorless, unaltered glass shards. For example, Section 157-955A-58X-1 contains a thin bed of pumice lapilli with a 2-mm-thick dark green lamination in the middle (Fig. 11). Minerals comprise alkali feldspar, alkali amphibole, and biotite. In Section 157-955A-58X-5, a thin bedded crystal-vitric tuff is composed of glass shards, felsic rock fragments, and abundant alkali feldspar, alkali amphibole, and sphene. Another type of coarse-grained volcaniclastic deposit occurs in Sections 157-955A-60X-3 to 157-955A-60X-4, which is characterized by a thick bed of coarse basaltic tuff that is normally graded in the upper part, planar laminated in the middle, and slightly reversely graded at the base with a sharp basal contact. It contains abundant tachylitic basaltic ash particles along with some felsic pumice.

Unit V

Interval: Sections 157-955A-60X-5 to 157-955A-63X-CC
Depth: 567–595 mbsf
Age: middle Miocene

Unit V is 28 m thick and is composed dominantly of greenish-gray clayey nannofossil mixed sedimentary rock with thin interbeds of dark gray silts and foraminifer-feldspar-quartz sands. This unit is distinguished from Subunit IVb by the lack of felsic volcaniclastic sediments, and by the presence of quartz-rich sands (Fig. 5). Important minor lithologies are a medium bedded unit of black basaltic lithic tuff with minor parallel laminations in Section 157-955A-60X-CC, and the presence of aphyric to sparsely pyroxene-phyric basalt clasts in Sections 157-955A-62X-CC and 157-955A-63X-CC. Calcium carbonate contents of hemipelagic sediments in Subunit V are identical to those in Subunit IVb and range from 30 to 65 wt%.

Depositional History

The oldest sediments recovered at Site 955 (Unit V) are hemipelagic nannofossil clays of middle Miocene age (~14–17 Ma) interbedded with minor volcaniclastic material (Section 157-955A-63X-CC). The presence of basalt clasts in Sections 157-955A-62X-CC and 157-955A-63X-CC suggests that at this depth there may be a transition from hemipelagic sediments to basaltic breccias and lapillistones. Basaltic tuffs such as those occurring in Section 157-953-60X-CC are similar to those found at Site 953 in the equivalent time-stratigraphic basal interval.

Thin interbeds of quartz-rich sand are also present in Unit V and are probably turbidites emplaced by sediment gravity flows coming from the northwestern continental margin of Africa. Similar quartz-rich silts and sands occur throughout the sequence, except for Subunit IVb, at Site 955. The presence of coarse-grained siliclastic material as a persistent minor, and sometimes major, sedimentary component strongly contrasts with the sediments at Sites 953 and 954 in which coarse, nonvolcanic sediments were dominated by neritic material from the Canary Islands.

At ~14 Ma (base of Subunit IVb) volcaniclastic deposits composed of pumice, felsic glass shards, crystals, and lithics appear in the section. This material was dominantly derived from the highly explosive rhyolitic Mogan Group volcanism on Gran Canaria that lasted from 14 to 13.4 Ma (Schmincke, 1994). These volcaniclastic sediments, many of which are poorly sorted, were probably emplaced by turbidity currents and debris flows, and some units are the distal equivalents of pyroclastic flows that entered the sea along the south coast of Gran Canaria.

Three of these tuffs can be correlated with subaerial eruptive units of known age on Gran Canaria by virtue of their distinctive mineralogical characteristics (Schmincke, 1994). A coarse basaltic tuff with minor felsic pumice and zircon occurs in Sections 157-955A-60X-3 and 157-955A-60X-4. The presence of zircon in this tuff is diagnostic of ignimbrite P1, a compositionally zoned ignimbrite dated at 14 Ma that forms an important chronostratigraphic marker at the base of the Mogan Group (Bogaard et al., 1988; Schmincke, 1994; Freundt and Schmincke, 1995). A crystal-vitric tuff in Core 157-955A-58X-5 contains trace amounts of sphene, which is a diagnostic indicator of ignimbrite X from the middle Mogan Group (Schmincke, 1976). This ignimbrite has been dated by single crystal $^{40}Ar/^{39}Ar$ at 13.8 ± 0.1 Ma (Bogaard et al., 1988). A pumice lapilli tuff in Section 157-955A-58X-5 contains phenocrysts of biotite, which is a characteristic feature of ignimbrite A from the upper Mogan Group on Gran Canaria (Schmincke, 1976).

At the bottom of Subunit IVa, the abundance of coarse, dark gray volcaniclastic sediments that are rich in lithics, crystals, and pumice (Fig. 5) increase dramatically. This change may mark the beginning of Fataga stage volcanism on Gran Canaria that consists mostly of trachyphonolitic lavas and tuffs erupted from ~13.4 to 9.5 Ma (Schmincke, 1994).

Felsic vitric components being supplied by turbidity currents and debris flows decrease from Subunits IVb and IVa. In addition, tuffs in Subunit IVa are typically zeolitized, whereas those in Subunit IVb are mostly composed of unaltered glass shards, probably the result of changes in composition of the vitric components, as the Fataga Group volcanics contain moderately silica-undersaturated felsic glass that is easily altered. These layers may also have been emplaced by turbidity currents or perhaps are the distal fallout equivalents of explosive volcanic eruptions.

In the upper part of Subunit IVa, the amount of quartz-rich, relatively nonvolcanic sands increases suddenly, corresponding with a rise in sea level that occurred in the late Miocene (Haq et al., 1987) that may be responsible for the change in influx of siliclastic sediment from the northwestern African continental margin.

Units II and III are composed almost entirely of hemipelagic sediments. The major difference between the two units is the much lower $CaCO_3$ contents and relative paucity of foraminifers in the sediments of Unit III (Fig. 6). The boundary between these two units is approximately coincident with the Miocene/Pliocene boundary, which is also a period of significant sea-level change. This change in sea level does not seem to have caused an influx of coarse siliciclastic material as occurred in the upper part of Subunit IVa. The virtual absence of any coarse volcaniclastic sediment emplaced by turbidity currents during this period is not surprising, because the upper part of Unit II corresponds with the constructional phase of the large Roque Nublo stratocone on Gran Canaria that was eroded by rivers draining almost entirely to the north.

Subunit Ib marks a transition to abundant deposition of nonvolcanic, quartz-rich silt and sand. Subunit Ia is dominated by hemipelagic sediment with thin interbedded nonvolcanic silt and sand. Shell-rich intervals form the matrix between large deformed mud clasts and coherent larger undeformed blocks. The overall poor sorting of this matrix suggests that it formed during slumping or debris flows in which shallow water bioclastic sands and deep water pelagic sediments were thoroughly mixed. In particular, the interval below Core 16H is characterized by very abundant soft sediment deformation features and the overlying interval (Cores 12H to 16H), which shows much less deformation, marks an age reversal in the biostratigraphy. Based on this evidence it seems likely that this interval was emplaced as a single large slump block or several smaller ones that were transported downslope from the edge of the continental shelf.

Volcaniclastic sediments in Subunit Ia consisting of vitric ash, pumiceous ash, and pumice sand were probably emplaced both by sediment gravity flows and from fallout. These deposits are similar to those recovered at Sites 953 and 954, and at Site 397 located 50 km to the south (Schmincke and von Rad, 1979). Based on their age and lithologic characteristics, the ashes are most likely derived from explosive eruptions of Pico de Teide Volcano on the island of Tenerife.

In summary, the sedimentary succession at Site 955 consists dominantly of fine-grained hemipelagic sediments interbedded with coarse-grained volcaniclastic and siliciclastic material that shows a number of important changes in frequency and thickness. Siliciclastic sediments derived from the northwestern African continental margin were emplaced by sediment gravity flows throughout many intervals in the upper and middle parts of the sequence and are also present in Unit V. Volcaniclastic sediments emplaced by sediment gravity flows and by fallout from explosive eruptions were supplied from Gran Canaria predominantly during the middle Miocene and from Tenerife during the late Pliocene to Pleistocene. The character of coarse-grained sediments at Site 955 has thus been largely controlled by temporal variations in these two components (volcanic vs. continental) that reflect larger scale changes in both sea level and growth of the nearby volcanic islands.

BIOSTRATIGRAPHY

Introduction

Hole 955A penetrated 599 m of fossiliferous, mostly pelagic sediments with some turbidites and volcaniclastic deposits ranging in age from Pleistocene to early middle Miocene–late early Miocene (Fig. 12).

The upper 170 m of the hole contain chaotic slumped intervals (see lithologic Subunit 1a in "Lithostratigraphy," this chapter), which are reflected in the biostratigraphic data. Within Unit Ia there is at least one hiatus in the lower Pleistocene to upper Pliocene representing removal of lower Pleistocene nannofossil Subzone CN13a and perhaps part of upper Pliocene Subzone CN12d and removal of upper Pliocene foraminiferal Zone PL6 and the basal part of Pleistocene N22. This hiatus at approximately 1.6 to 2.37 Ma occurs between 102.81 and 103.1 mbsf. Also within Subunit 1a there is a block of lower Pliocene sediment within the upper Pliocene, possible removal of an additional upper Pliocene section, and perhaps removal of some middle Pliocene. There is also a hiatus at roughly 8.8 to 9.4 Ma, within the late Miocene, between 364.0 and 373.6 mbsf, near the base of lithologic Unit III. This hiatus is expressed mainly in the nannofossil data. The lower Pleistocene to upper Pliocene hiatus and the late Miocene hiatus, are similar in age to those present at Site 954 and may be regional in scale.

The Pliocene/Pleistocene boundary is placed at the disconformity between 102.81 and 103.1 mbsf. The Pliocene/Miocene boundary is placed between 262.9 mbsf, the base of Zone PL1, and 263.16 mbsf, the highest occurrence of *Discoaster quinqueramus* below the base of PL1. This placement may be a little high since the Miocene foraminiferal marker in this area, *Globorotalia juanai,* is not observed until 272.6 mbsf.

Calcareous Nannofossils

Pleistocene

Pleistocene nannofossils were recovered from Sample 157-955A-1H-3, 79 cm (3.79 mbsf), to 157-955A-11H-7, 21 cm (102.81 mbsf; Table 2). The uppermost sample, 157-955A-1H-3, 79 cm (3.79 mbsf), was below the acme of *Emiliania huxleyi* in Zone CN15, indicating an age older than 82 Ka (Thierstein et al., 1977). The lowest occurrence of *E. huxleyi,* which marks the base of Zone CN15, could not be positively determined using the light microscope. Instead, the downcore change in dominance from *Gephyrocapsa* spp. smaller than about 3 µm to *G. "caribbeanica"* larger than about 3 µm, which occurs at the base of oxygen isotope stage 7 (Weaver, 1983), was used to approximate the Zone CN15/CN14 boundary. This change occurs between Samples 157-955A-3H-3, 132 cm (21.92 mbsf), and 157-955A-3H-7, 70 cm (27.30). The highest occurrence of *Pseudoemiliania lacunosa* in Sample 157-955A-4H-2, 70 cm (29.30 mbsf), indicates Subzone CN14a. Within Subzone CN14a, Sample 157-955A-7H-1, 68 cm (56.28 mbsf), contains the highest occurrence of *R. asanoi,* and Sample 157-955A-8H-6,73 cm (73.33 mbsf), contains the lowest occurrence, which is used to approximate the base of Subzone CN14a.

The only useful events within Subzone CN13b that could be distinguished were the highest and lowest occurrences of large (>5.5 µm) *Gephyrocapsa* spp., which were in Samples 157-955A-9H-6, 44 cm (82.54 mbsf), and 157-955A-10H-7, 13 cm (93.23 mbsf). The LO datums of *Calcidiscus macintyrei* and *Helicosphaera sellii* usually occur stratigraphically beneath these *Gephyrocapsa* events; however, *C. macintyrei* and *H. sellii* occur sporadically in this interval and are apparently reworked.

Pliocene

From ~93.73 to 170 mbsf the biostratigraphic record reflects the disturbed and slumped nature of lithologic Subunit Ia. The highest occurrence of *Discoaster brouweri* without *D. pentaradiatus* in Sample 157-955A-11H-CC (103.08 mbsf) indicates Pliocene Subzone CN12d. The occurrence of CN13b directly above CN12d without any intervening SubzoneSubzoneCN13a (the lowest Pleistocene zone) indicates missing section. This idea is supported by the foraminifer data where Zone PL6 in the uppermost Pliocene is missing. This seems to suggest a lower Pleistocene to upper Pliocene hiatus.

Within the Pliocene, lower Pliocene Zone CN10 may be slumped within upper Pliocene Subzone CN12a and lower Pliocene Subzones CN12c and CN12b may be missing; however, additional sampling is needed to determine the missing zones. The highest occurrence of *Discoaster tamalis* in Sample 157-955A-13H-7, 59 cm, marks Subzone CN12a, which is directly beneath Subzone CN12d in Sample 157-955A-13H-2, 76 cm (114.86 mbsf). The FO of *D.tamalis* defines the base of Subzone CN12a in Sample 157-955A-14H-6, 60 cm (130.20 mbsf); however, directly beneath it in Samples 157-955A-14H-CC (131.81 mbsf) to 157-955A-16H-1, 80 cm (141.90 mbsf), is an interval containing *Amaurolithus* spp. and *D. asymmetricus* without *Pseudoemiliania lacunosa* suggesting Zone CN10.

In Samples 157-955A-16H-7, 60 cm (150.75 mbsf), to 157-955A-22X-6, 11 cm (203.11 mbsf), Subzone CN12a is again indicated by the recurrence of *D. tamalis.* The highest occurrence of *Reticulofenestra pseudoumbilicus* and *Sphenolithus* spp. without *D. tamalis* in Sample 157-955A-23X-3, 89 cm (208.99 mbsf), indicates Subzone CN11a. This suggests that Subzone CN11b is missing although additional sampling would be necessary to determine this. Sample 157-955A-27X-4, 26 cm (248.36 mbsf), contains *Amaurolithus* spp. and indicates Zone CN10 again.

Miocene

The highest occurrence of *D. quinqueramus* in Sample 157-955A-28X-CC (262.87 mbsf) indicates late Miocene Subzone CN9b. The base of this zone is indicated in Sample 157-955A-34X-5, 80 cm (317.60 mbsf), by the lowest occurrence of *A. primus* in Sample 157-955A-33X-CC (310.78 mbsf). The lowest occurrence of *D. berggrenii* in Sample 157-955A-37X-1, 80 cm (340.40 mbsf), indicates the base of Subzone CN9a.

Between 364 and 373 mbsf a short hiatus between 8.8 and 9.4 Ma is suggested by the nannofossil data. As at Site 954 *Discoaster loeblichii* and *D. neorectus,* the primary markers for Subzone CN8b, were not seen. However, another event, the LO of large *Reticulofenestra pseudoumbilicus* (>7 µm maximum diameter), which occurs within the lower part of CN8b (Rio et al., 1990; Young, 1990; Young et al., 1994), at about 8.8 Ma, proved useful. Sample 157-955A-40X-4, 80 cm (373.60 mbsf) contains both the highest occurrence of large *R. pseudoumbilicus,* which has a LO datum of 8.8 Ma, and the highest occurrence of *D. hamatus,* which has a LO datum of 9.4 Ma. The co-occurrence of these two events suggests a short hiatus. A hiatus of this age is also present at Site 954, which suggests a regional event.

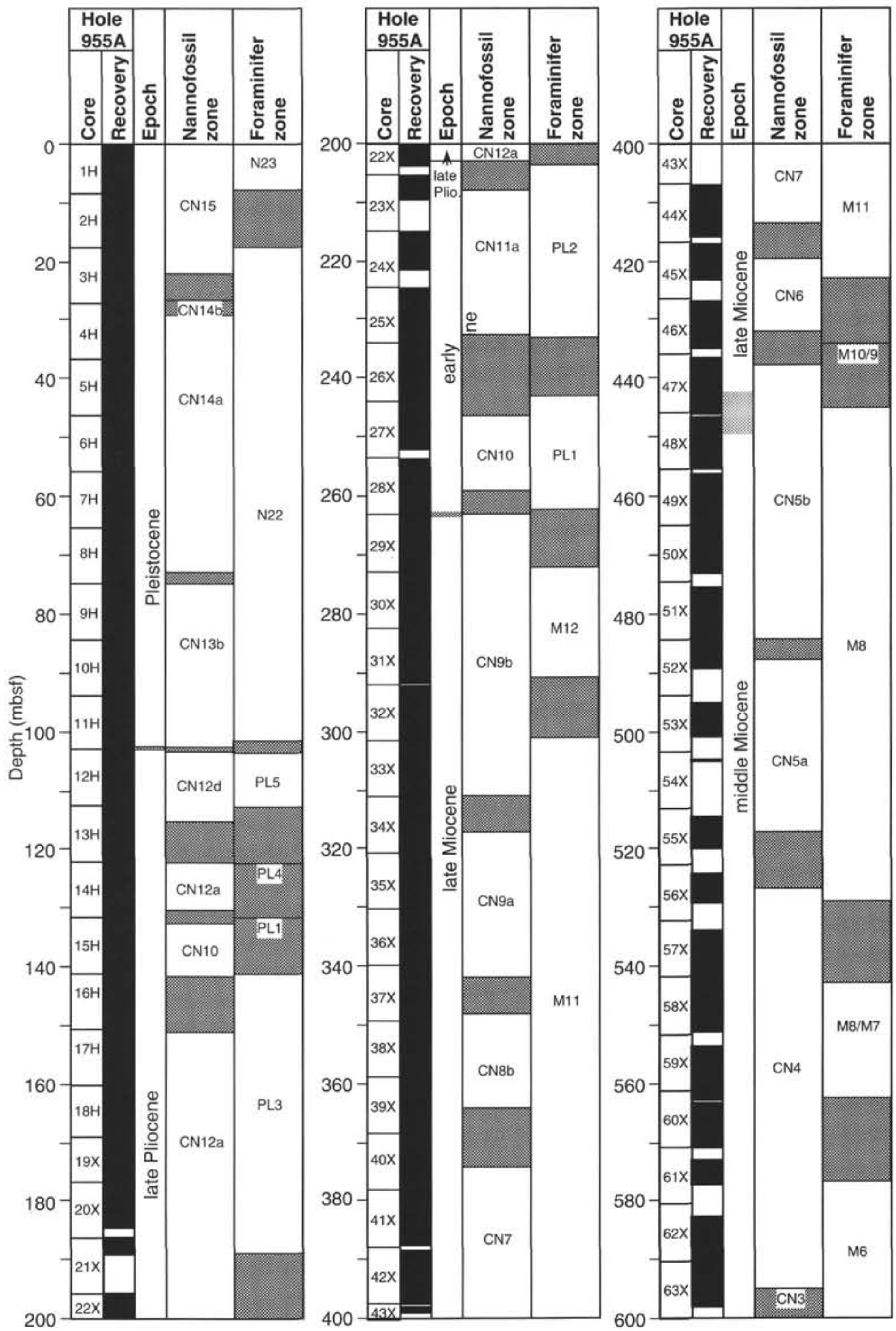

Figure 12. Nannofossil and foraminifer zonation at Site 955.

The lowest occurrence of *D. hamatus* in Sample 157-955A-44X-CC (415.18 mbsf) marks the base of Zone CN7. The lowest occurrence of *Catinaster coalitus* in Sample 157-955A-46X-5, 43 cm (432.63 mbsf), indicates the base of CN6. The lowest occurrence of *D. kugleri* in Sample 157-955A-51X-CC (483.74 mbsf) indicates the base of Subzone CN5b and the highest occurrence of *Sphenolithus heteromorphus* in Sample 157-955A-56X-3, 120 cm (526 mbsf), indicates Zone CN4. The lowest nannofossil datum for Hole 955A, in Sample 157-955A-63X-CC (595.06 mbsf), is the highest occurrence of *Helicosphaera ampliaperta,* indicating Zone CN3.

Planktonic Foraminifers

Preservation of foraminifers was quite good and abundance was high generally throughout the hole (Table 3) except for an interval of low abundance and poor preservation near the base of the hole.

Table 2. Abundance, preservation, and lithology of samples used in nannofossil zonation, Hole 955A.

Core, section, interval (cm)	Depth (mbsf)	Abundance	Preservation	Zone	Lithology
157-955A-					
1H-3, 79–79	3.79	VH	G	CN15	Hemipelagic ooze
1H-6, 6–6	7.56	VH	G	CN15	Hemipelagic ooze
2H-4, 70–70	13.30	VH	G	CN15	Hemipelagic ooze
2H-7, 65–65	17.75	VH	G	CN15	Hemipelagic ooze
3H-3, 132–132	21.92	VH	G	CN15	Hemipelagic ooze
3H-7, 70–70	27.30	VH	G	CN14b	Hemipelagic marl
4H-2, 70–70	29.30	VH	G	CN14a	Hemipelagic ooze
4H-7, 19–19	36.29	VH	G	CN14a	Hemipelagic ooze
5H-7, 27–27	45.87	VH	G	CN14a	Hemipelagic ooze
6H-1, 45–45	46.55	H	G	CN14a	Hemipelagic ooze
6H-7, 6–6	55.16	H	G	CN14a	Hemipelagic ooze
7H-1, 68–68	56.28	H	G	CN14a	Hemipelagic ooze
7H-4, 106–106	61.16	H	G	CN14a	Hemipelagic ooze
7H-7, 20–20	64.80	VH	G	CN14a	Hemipelagic ooze
8H-1, 39–39	65.49	H	G	CN14a	Hemipelagic ooze
8H-6, 73–73	73.33	VH	G	CN14a	Hemipelagic ooze
8H-CC	74.92	H	G	CN13b	Hemipelagic ooze
9H-6, 44–44	82.54	H	G	CN13b	Hemipelagic ooze
10H-4, 74.5–74.5	89.35	H	G	CN13b	Hemipelagic ooze
10H-7, 13–13	93.23	H	G	CN13b	Hemipelagic ooze
10H-CC	93.73	VH	G	CN13b	Hemipelagic ooze
11H-7, 21–21	102.81	VH	M	CN13b	Hemipelagic ooze
11H-CC	103.08	H	G	CN12d	Hemipelagic ooze
12H-6, 86–86	111.46	H	M	CN12d	Hemipelagic ooze
13H-2, 76–76	114.86	H	G	CN12d	Hemipelagic ooze
13H-7, 59–59	122.19	H	M	CN12a	Hemipelagic ooze
13H-CC	122.29	H	G	CN12a	Hemipelagic ooze
14H-6, 60–60	130.20	H	M	CN12a	Hemipelagic ooze
14H-CC	131.81	H	M	CN10	Hemipelagic ooze
15H-2, 53–53	133.63	H	M	CN10	Hemipelagic ooze
15H-7, 30–30	140.90	H	M	CN10	Hemipelagic ooze
16H-1, 80–80	141.90	H	M	CN10	Hemipelagic ooze
16H-7, 60–60	150.75	H	M	CN12a	Hemipelagic ooze
17H-7, 20–20	159.80	H	M	CN12a	Hemipelagic ooze
18H-CC, 10–10	168.52	H	M	CN12a	Hemipelagic ooze
19X-7, 27–27	178.17	H	G	CN12a	Hemipelagic ooze
20X-6, 40–40	184.35	H	G	CN12a	Hemipelagic ooze
21X-2, 40–40	187.90	M	G	CN12a	Hemipelagic ooze
22X-6, 11–11	203.11	H	G	CN12a	Hemipelagic ooze
23X-3, 89–89	208.99	H	G	CN11a	Hemipelagic ooze
24X-1, 27–27	214.87	H	M	CN11a	Hemipelagic ooze
25X-1, 12–12	224.42	H	G	CN11a	Hemipelagic ooze
25X-7, 18–18	233.48	H	G	CN11a	Hemipelagic ooze
26X-2, 40–40	235.90	H	G	CN11a	Hemipelagic ooze
27X-4, 26–26	248.36	H	G	CN10	Hemipelagic ooze
28X-5, 34–34	259.64	VH	M	CN10	Hemipelagic ooze
28X-CC	262.87	VH	M	CN9b	Hemipelagic ooze
29X-1, 16–16	263.16	VH	G	CN9b	Hemipelagic ooze
29X-CC	272.57	VH	M	CN9b	Hemipelagic ooze
30X-CC	282.22	VH	M	CN9b	Hemipelagic ooze
31X-CC	291.09	H	M	CN9b	Hemipelagic ooze
32X-CC	301.16	H	M	CN9b	Hemipelagic marl
33X-4, 70–70	306.40	H	M	CN9b	Hemipelagic marl
33X-CC	310.78	H	M	CN9b	Hemipelagic marl
34X-5, 80–80	317.60	M	G	CN9a	Hemipelagic marl
34X-CC	320.30	H	M	CN9a	Hemipelagic marl
35X-CC	329.94	H	G	CN9a	Hemipelagic marl
36X-4, 70–70	335.30	H	G	CN9a	Hemipelagic marl
36X-CC	339.59	M	G	CN9a	Hemipelagic marl
37X-1, 80–80	340.40	H	G	CN9a	Hemipelagic marl
37X-4, 80–80	344.90	M	G	CN8b	Hemipelagic marl
37X-CC	348.83	M	G	CN8b	Hemipelagic marl
38X-4, 80–80	354.40	M	G	CN8b	Hemipelagic marl
38X-CC	358.51	H	G	CN8b	Hemipelagic marl
39X-4, 80–80	364.00	H	M	CN8b	Hemipelagic marl
40X-4, 80–80	373.60	M	G	CN7	Hemipelagic marl
40X-CC	377.26	M	G	CN7	Hemipelagic marl
41X-CC	386.59	M	G	CN7	Hemipelagic marl
42X-CC	396.50	H	G	CN7	Hemipelagic marl
43X-CC	398.20	H	G	CN7	Hemipelagic marl
44X-CC	415.18	H	G	CN7	Hemipelagic marl
45X-3, 58–58	420.08	H	G	CN6	Hemipelagic marl
45X-CC	422.30	H	M	CN6	Hemipelagic marl
46X-5, 43–43	432.63	H	G	CN6	Hemipelagic marl
46X-CC	433.70	M	M	CN5b	Hemipelagic marl
47X-CC	444.80	H	M	CN5b	Hemipelagic marl
48X-1, 34–34	445.84	VH	M	CN5b	Hemipelagic marl
48X-4, 47–47	450.47	VH	G	CN5b	Hemipelagic marl
48X-CC	454.05	M	M	CN5b	Hemipelagic marl
49X-5, 33–33	461.53	H	G	CN5b	Hemipelagic marl
49X-CC	464.20	H	M	CN5b	Hemipelagic marl
50X-3, 74–74	468.54	H	M	CN5b	Hemipelagic marl
50X-CC	471.57	H	M	CN5b	Hemipelagic marl
51X-CC	483.74	M	G	CN5b	Hemipelagic marl
52X-CC	487.55	H	M	CN5a	Hemipelagic marl
53X-CC	499.00	M	M	CN5a	Hemipelagic marl
55X-CC	517.74	H	G	CN5a	Hemipelagic marl
56X-3, 120–120	526.60	M	M	CN4	Hemipelagic marl
56X-CC	527.32	M	G	CN4	Hemipelagic marl

Table 2 (continued).

Core, section, interval (cm)	Depth (mbsf)	Abundance	Preservation	Zone	Lithology
57X-CC	541.00	H	G	CN4	Hemipelagic marl
58X-CC	548.81	H	G	CN4	Hemipelagic marl
59X-1, 105–105	552.25	M	M	CN4	Hemipelagic marl
59X-6, 110–110	559.80	M	M	CN4	Hemipelagic marl
59X-CC	560.11	M	M	CN4	Hemipelagic marl
60X-4, 95–95	566.35	H	M	CN4	Hemipelagic marl
61X-CC	574.26	M	M	CN4	Hemipelagic marl
62X-CC	589.88	M	M	CN4	Hemipelagic marl
63X-4, 60–60	594.90	M	M	CN4	Hemipelagic marl
63X-CC	595.06	M	M	CN3	Hemipelagic marl

Note: Key to abbreviations for abundance and preservation in "Explanatory Notes" chapter (this volume).

Table 3. Abundance, preservation, and lithology of samples used in foraminifer zonation, Site 955.

Core, section, interval (cm)	Depth (mbsf)		Abundance	Preservation	Zone	Lithology
	Top	Bottom				
157-955A-						
1H-1, 0–2	0.00	0.02	A	G	N23	Brownish ooze
1H-CC, 0–2	7.89	7.91	A	G	N23	Ooze
2H-CC, 0–2	17.67	17.69	A	G	N22	Ooze
3H-CC, 0–2	27.34	27.36	A	G	N22	Ooze
4H-CC, 0–2	36.74	36.76	A	G	N22	Greenish ooze
5H-CC, 0–2	46.26	46.28	A	G	N22	Greenish marl
6H-CC, 0–2	55.79	55.81	A	G	N22	Ooze
7H-CC, 0–2	65.35	65.37	A	G	N22	Pale green ooze
8H-CC, 0–2	74.91	74.93	A	G	N22	Pale green ooze
9H-CC, 0–2	84.35	84.37	A	M	N22	Pale green ooze
10H-CC, 0–2	93.72	93.74	A	G	N22	Greenish oozes
11H-3, 128–130	97.87	97.89	A	G	N22	Marly oozes
11H-6, 41–43	101.50	101.52	A	G	N22	Marly oozes
11H-CC, 0–2	103.07	103.09	A	G	PL5	Marly oozes
12H-CC, 0–2	112.66	112.68	A	M	PL5	Greenish clayey nannofossil ooze
13H-CC, 0–2	122.28	122.30	A	G	PL4	Gray ooze
14H-CC, 0–2	131.80	131.82	C	P	PL1	Gray ooze
15H-CC, 0–2	141.23	141.25	C	M	PL3	Gray ooze
16H-CC, 0–2	150.83	150.85	A	M	PL3	Green-gray ooze
17H-CC, 0–2	160.31	160.33	C	M	PL3	Gray ooze
18H-CC, 0–2	168.41	168.43	A	G	PL3	Gray ooze
19X-CC, 0–2	178.26	178.28	A	G	PL3	Green-gray ooze
20X-CC, 0–2	184.48	184.50	F	P	PL3?	Foraminifer-rich mineral sand
21X-CC, 0–2	189.00	189.02	A	M	PL3	Marl
22X-CC, 0–2	203.57	203.59	A	G	PL2	Marl
23X-CC, 0–2	209.13	209.15	A	G	PL2	Marl
24X-CC, 0–2	220.99	221.01	A	G	PL2	Marl
25X-CC, 0–2	233.84	233.86	A	G	PL2	Marl
26X-CC, 0–2	243.58	243.60	A	G	PL1	Greenish-gray marl
27X-4, 27–29	248.36	248.38	A	G	PL1	Greenish-gray marl
28X-CC, 0–2	262.86	262.88	A	G	PL1	Marl
29X-CC, 0–2	272.56	272.58	C	M	M12	Greenish-gray marl
30X-CC, 0–2	282.21	282.23	C	P	M12	Clayey nannofossil ooze
31X-CC, 0–2	291.08	291.10	C	M	M12	Marl
32X-CC, 0–2	301.15	301.17	F	P	M11	Marl
34X-CC, 0–2	320.29	320.31	C	M	M11	Marl
35X-CC, 0–2	329.93	329.95	C	M	M11	Marl
36X-CC, 0–2	339.58	339.60	C	M	M12?	Marl
37X-CC, 0–2	348.82	348.84	C	M	M12?	Marl
38X-CC, 0–2	358.50	358.52	C	M	M11	Marl
39X-CC, 0–2	368.05	368.07	A	M	M11	Marl
40X-CC, 0–2	377.25	377.27	C	M	M11	Marl
41X-CC, 0–2	386.58	386.60	F	M	M11	Marl
42X-CC, 0–2	396.49	396.51	C	M	M11	Marl
43X-CC, 0–2	398.19	398.21	C	M	M11	Marl
44X-CC, 0–2	415.17	415.19	C	M	M11	Marl
45X-CC, 0–2	422.29	422.31	A	M	M11	Marl
46X-CC, 0–2	433.69	433.71	C	M	M10/M9	Marl
47X-CC, 0–2	444.79	444.81	C	P	M8	Marl
48X-CC, 0–2	454.04	454.06	C	M	M8	Marl
49X-CC, 0–2	464.19	464.21	A	G	M8	Marl
50X-CC, 0–2	471.99	472.01	A	M	M8	Marl
51X-CC, 0–2	483.99	484.01	C	P	M8	Marl
52X-CC, 0–2	487.54	487.56	A	M	M8	Marl
53X-CC, 0–2	498.99	499.01	F	P	M8	Marl
55X-CC, 0–2	517.73	517.75	F	P	M8/M7	Clayey nannofossil foraminifer ooze
56X-CC, 0–2	527.31	527.33	R	P	M8	Clayey nannofossil foraminifer ooze
57X-CC, 0–2	540.99	541.01	R	P	M8/M7	Coarse ash?
58X-CC, 0–2	548.80	548.82	R	P	?	Marl
59X-CC, 0–2	560.10	560.12	R	P	M8/M7	Marl
61X-CC, 0–2	574.25	574.27	A	P	M6	Marl
62X-CC, 0–2	589.87	589.89	A	P	M6	Marl
63X-CC, 0–2	595.05	595.07	A	M	M6	Foraminifer sand

Note: Key to abbreviations for abundance and preservation in "Explanatory Notes" chapter (this volume).

Pleistocene

The Quaternary sequence was divided into Zone N23 based on the range of *Globigerina calida calida* and Zone N22 between the first appearances of *Globorotalia truncatulinoides* and *Globigerina calida calida* (Fig. 12). The interval contained a diverse assemblage typical of subtropical waters including abundant *Globigerinoides ruber, Globigerinella aequilateralis, Globigerinoides sacculifer,* and *Globorotalia crassaformis.* Climatic fluctuations were indicated by the alternation of warm subtropical assemblages with *Pulleniatina obliquiloculata* and cool subtropical assemblages with abundant dextral *Neogloboquadrina pachyderma* and *Globorotalia inflata.* Lower Zone N22 was not recovered. The lower part of the zone typically contains abundant *Sphaeroidinella dehiscens* and rare *Globorotalia truncatulinoides,* but this interval was not encountered probably due to a hiatus. The deepest sample assigned to N22 was Sample 157-955A-11H-6, 41–43 cm (101.50 mbsf). This sample lies within a slumped interval based on the lithologic description.

Pliocene

The next foraminifer sample beneath the slump in Core 157-955A-11H was assigned to Zone PL5 (Sample 157-955A-11H-CC, 0–2 cm, 103.07 mbsf). Zone PL6 was not observed in the sequence. Sample 157-955A-12H-CC, 0–2 cm, was also placed in Zone PL5 based on the occurrence of *Globorotalia miocenica* without *Globorotalia multicamerata.* Sample 157-955A-13H-CC, 0–2 cm (122.28 mbsf), was assigned to Zone PL4 based on the presence of *Globorotalia multicamerata* and *Dentoglobigerina altispira* without *Sphaeroidinellopsis seminulina.*

Sample 157-955A-14H-CC, 0–2 cm (131.81 mbsf) contained a fauna typical of Zone PL1 including *Globorotalia margaritae, Globigerina nepenthes,* and *Sphaeroidinellopsis seminulina.* The sample probably contains very little upper Pliocene material because *Globorotalia crassaformis* and *Globorotalia puncticulata* were absent from the sample. However, rare specimens close to *Globorotalia multicamerata* and *Globorotalia miocenica* were present. The sample contained a benthonic foraminiferal assemblage of lower bathyal to abyssal forms including *Fontbotia wuellerstorfi, Oridorsalis umbonatus, Sigmoilopsis schlumbergeri,* and *Epistominella exigua.* No shallower forms were noted suggesting that the sample probably was not reworked from shallow depth. The sample probably lies in a block of lower Pliocene sediment slumped to Site 955. This interpretation is supported by the nannofossil data.

The interval between Samples 157-955A-15H-CC, 0–2 cm (141.24 mbsf), and 157-955A-21X-CC, 0–2 cm (189.01 mbsf), was assigned to Zone PL3 by the occurrences of common *Globorotalia multicamerata, Globorotalia miocenica, Sphaeroidinellopsis seminulina, Globorotalia puncticulata,* and *Globorotalia hirsuta.* However, foraminifer-rich mineral sands in Samples 157-955A-15H-CC, 0–2 cm, and 157-955A-20X-CC, 0–2 cm, contain rare reworked specimens of lower Pliocene species *Globorotalia margaritae* and *Globigerina nepenthes.*

Samples from 157-955A-22X-CC, 0–2 cm (203.6 mbsf), to 157-955A-25X-CC, 0–2 cm (233.85 mbsf) were placed in Zone PL2 because they had a continuous sequence of *Globorotalia margaritae* without *Globigerina nepenthes.* The highest occurrence of *Globigerina nepenthes* was in Sample 157-955A-26X-CC, 0–2 cm (243.6 mbsf), and marked the top of Zone PL1. Samples from 157-955A-26X-CC, 0–2 cm, to 157-955A-28X-CC, 0–2 cm, were assigned to Zone PL1 based on the occurrence of *Globorotalia margaritae* and *Globigerina nepenthes* without *Globorotalia juanai.*

Miocene

The upper zone of the Miocene, Zone M13, could not be recognized based on the definitive species, *Globoquadrina dehiscens,* because it was excluded from this region of the Atlantic Ocean after 9.99 Ma. Instead, we used the highest stratigraphic occurrence of *Globorotalia juanai* to approximate the upper boundary. We did not find any material assignable to M13 at Site 955. Uppermost Miocene Samples 157-955A-29X-CC, 0–2 cm, 157-955A-30X-CC, 0–2 cm, and 157-955A-31X-CC, 0–2 cm, belong to Zone M12, based on the presence of *Globorotalia conomiozea,* sinistral *Neogloboquadrina acostaensis,* and the absence of *Globorotalia margaritae.*

Samples 157-955A-32X-CC, 0–2 cm, to 157-955A-45X-CC, 0–2 cm, were assigned to Zone M11 based on the presence of *Neogloboquadrina acostaensis* and the absence of *Globorotalia conomiozea.* The upper part of the zone bore sinistral *Neogloboquadrina acostaensis,* and the coiling shift to dextral forms occurs deeper in the sequence in Sample 157-955A-40X-CC, 0–2 cm. *Globorotalia lenguaensis* and *Globorotalia menardii menardii* appears sporadically below Core 157-955A-38X, and *Globoquadrina dehiscens* has its highest occurrence in Sample 157-955A-44X-CC, 0–2 cm, near the base of the zone. Two samples within the interval assigned to Zone M11, Samples 157-955A-36X-CC, 0–2 cm, and 157-955A-37X-CC, 0–2 cm, contain forms similar to *Globorotalia conomiozea.*

Only Sample 157-955A-46X-CC, 0–2 cm, was assigned to Zone M10/M9 based on the absence of *Neogloboquadrina acostaensis* and the presence of *Globigerina nepenthes.* Other species included *Globoquadrina dehiscens* and *Globorotalia menardii menardii.* Samples from 157-955A-47X-CC, 0–2 cm, to 157-955A-56X-CC, 0–2 cm, belong in Zone M8 based on the absence of *Globigerina nepenthes* and *Globorotalia peripheroronda. Paragloborotalia mayeri* and *Globorotalia siakensis* were persistent elements of the assemblage, and *Globorotalia fohsi* s.l. occurred sporadically throughout the interval. Samples from 157-955A-57-X–CC, 0–2 cm (541 mbsf), to 157-955A-59X-CC, 0–2 cm (560.1 mbsf), contained rare and poorly preserved specimens and were difficult to assign to a zone. The upper sample was placed tentatively in M8/7 as it contained *Globorotalia peripheroacuta.* Sample 157-955A-58-X-CC, 0–2 cm, was from an ignimbrite and was barren.

The abundance of planktonic foraminifers increases downhole from Samples 157-955A-61X-CC, 0–2 cm (574.3 mbsf), to 157-955A-63X-CC, 0–2 cm (595.1 mbsf), near the base of the hole. The first two samples had *Dentoglobigerina altispira, Globoquadrina baroemoenensis, Globorotalia continuosa, Globorotalia peripheroronda, Globorotalia archeomenardii,* and *Sphaeroidinellopsis disjuncta* along with one specimen each of *Praeorbulina glomerosa circularis.* The bottom sample, a foraminiferal sand layer at the base of a probable turbidite, contains a rich and well-preserved planktonic assemblage including abundant *Praeorbulina glomerosa glomerosa, Praeorbulina glomerosa curva, Praeorbulina glomerosa circularis,* and *Globigerinoides sicanus.* The samples were tentatively assigned to Zone M6.

PALEOMAGNETISM

Introduction

Paleomagnetic measurements were made on the APC and the XCB cores recovered from Hole 955A. They were demagnetized to at least 25 mT and analyzed for magnetostratigraphy. The results from the XCB cores showed a strong normal overprint that was interpreted as magnetization acquired during drilling. The overprint consists of a component directed almost vertically downward, which is easily demagnetized, and a much harder component directed downward and radially. This latter component was so intense and hard that the AF-cleaning procedure was not able to get rid of it. In view of the domination of the signal by this magnetization, a number of experiments were carried out to investigate its origin. We also developed a test to detect this type of magnetic behavior. These will be described in the Leg 157 *Scientific Results* volume.

The APC cores from Hole 955A were measured in the long-core mode on the 2G magnetometer after demagnetization to 25 mT. The results show a weaker bias to normal polarity than the XCB cores and appear to have acquired a somewhat weaker drill component which was again directed downward and outward in the core.

Nearly all the XCB cores were measured in the long-core mode. The intensity shows an increase with a higher normal overprint. The biscuiting process caused by XCB drilling combined with inflow of wet drilling crushed material between the biscuits makes interpretation of long-core measurements unreliable.

Magnetostratigraphy

Hole 955A

Plots of the inclination from cores are shown in Figure 13, with the NRM intensity after demagnetization of 25 mT from the 2G magnetometer and the susceptibility data from the whole-core MST measurements.

In the first core, 157-955A-1H, an interval that may be a short event in the Brunhes appears, but in view of the difficulty in the interpretation of the paleomagnetism in Hole 955A, we are unsure whether this observed reversed inclination is a reflection of field behavior. Another similar feature is seen in Core 157-955A-3H, but this core is clearly disturbed in part.

There is a polarity change from normal to reversed between 56.5 to 57.5 mbsf. This is interpreted as the Brunhes/Matuyama transition and is consistent with the biostratigraphy. Below this, there is an interval of about 2 m of reversed sediment, which is the top of the Matuyama.

The preceding 60 m have low intensity, low susceptibility values in comparison to previous VICAP sites, and a normal polarity. This material is impossible to interpret at present. The low intensity is approaching the noise level of the instrument and for this reason alone it is not wise to interpret its polarity until shore-based measurements have been made on discrete samples. In addition, much of the section is slumped and it is possible that slumping may partially demagnetize and/or remagnetize the original signal. Between 130 and 150 mbsf the intensity increases and we see the first clear evidence of reversed intervals below the short Matuyama interval. However, the interval is too small to attempt magnetostratigraphic interpretation. In Core 157-955A-20X the base of the slump is reached and the intensity of remanence accompanied by a minor increase in susceptibility increases spectacularly. This again suggests that the slumping may reduce the magnetic signal.

In the remainder of the recovered interval, the remanence is monotonously normal. The susceptibility and remanence intensity records are as usual inversely correlated with carbonate. Both values are generally weaker than in the previous VICAP sites. This behavior might suggest a lower content of magnetic input or a change in kind of magnetic material.

Rock Magnetism

The demagnetization characteristics of NRM, ARM, and IRM, and measurements of weak field susceptibility were conducted as part of the preliminary rock magnetism analysis, the magnitudes of which have also revealed systematic differences downhole. For example, in the King diagram (Figure 14), the general increase in both parameters correlates with depth downcore. The muds formed between the biscuits have the highest ARM intensity and susceptibility values.

A Test for Radial Components of Magnetism

In analyzing data from earlier holes, we were not sure when we were encountering the effect of the drilling overprint. However, in Hole 955A a strong drill movement was evident and a simple test has been developed to detect radial drill contamination. In addition to measuring the archive half, the working half of a section is also measured. If the magnetization is directed oppositely, when the two halves are measured, as shown in Case 1 in Figure 15, the whole core is homogeneously magnetized. If, on the other hand, both halves give the same magnetization (Case 2), it is radially magnetized and should be interpreted for magnetostratigraphy with caution.

Conclusions

The magnetostratigraphy of sediments from Hole 955A has been impossible to establish below the Brunhes/Matuyama. A test has been developed to detect the radial aspect of the drill magnetization overprint.

PETROGRAPHY, MINERALOGY, AND GEOCHEMISTRY OF VOLCANICLASTIC SEDIMENTS

Volcaniclastic sediments recovered at Site 955 include ash fall, pumice sand, zeolitized tuffs, vitric-crystal tuffs, and basaltic tuffs. In addition, quartz-rich silt and sand turbidites commonly contain minor volcanic lithics and crystals. As observed at Sites 953 and 954, the stratigraphic succession of lithic, crystal, and vitric components and the trace element geochemistry of whole-rock and sediment samples closely parallel the subaerial volcanic stratigraphy of Gran Canaria (Table 4).

Petrography and Mineralogy

Unit I (0–207 mbsf) contains numerous beds of foraminifer-lithic silt and sand. The dominant lithic clasts are tachylitic basalt, trachyphonolite lava (groundmass aegirine) and fine-grained tuff. Crystals are mostly alkali feldspar and plagioclase, with less abundant clinopyroxene (both aegirine-augite and Ti-augite), and minor amphibole (Fig. 16). These volcaniclastic components appear to be derived dominantly from erosion of the Miocene Fataga Group (trachyphonolite) of Gran Canaria and late Pliocene to Holocene post-Roque Nublo basalts and basanites (basaltic lithics, rare sideromelane). In contrast to the upper parts of the sequences at Sites 953 and 954, erosional detritus from the Pliocene Roque Nublo Group (Ti-augite, brown amphibole) is very minor at Site 955, probably because the Roque Nublo volcanic edifice was largely eroded and drained to the north of the island.

Fine-grained ash layers and pumiceous sands are also present in Subunit Ia. The ash fall layers are composed chiefly of colorless glass shards, presumably of phonolitic composition, which are most likely the result of explosive eruptions of Pico de Teide Volcano (Tenerife).

Unit II (207–273 mbsf) is composed entirely of fine-grained hemipelagic sediment and contains no volcaniclastic sediments. The age of sediments in this interval corresponds with the constructional phase of the Roque Nublo volcano which, as described above, supplied material dominantly to the north of Gran Canaria.

Unit III (273–374 mbsf) is also composed dominantly of fine-grained hemipelagic sediments but, in contrast to Unit II, contains thin interbeds of quartz silt and sand with minor volcanic lithic fragments. In addition it contains a tuff composed of zeolites with minor green clinopyroxene. Unit III corresponds to the volcanic hiatus on Gran Canaria, which accounts for the general paucity of volcaniclastic material.

Subunit IVa (374–513 mbsf) contains numerous interbeds of quartz-foraminifer silt and sand with volcanic lithics and crystals, crystal-lithic sands, and many fine-grained zeolitized tuffs. The silts and sands are typically poorly sorted, with abundant matrix composed of clay and calcareous nannofossils. Lithic components are dominantly trachyphonolite lava and fine-grained tuff together with minor basaltic clasts (Fig. 16). Large crystals of alkali feldspar are abundant and make up as much as 25% of some crystal-lithic sands. Other crystals include large green clinopyroxene (aegirine-augite),

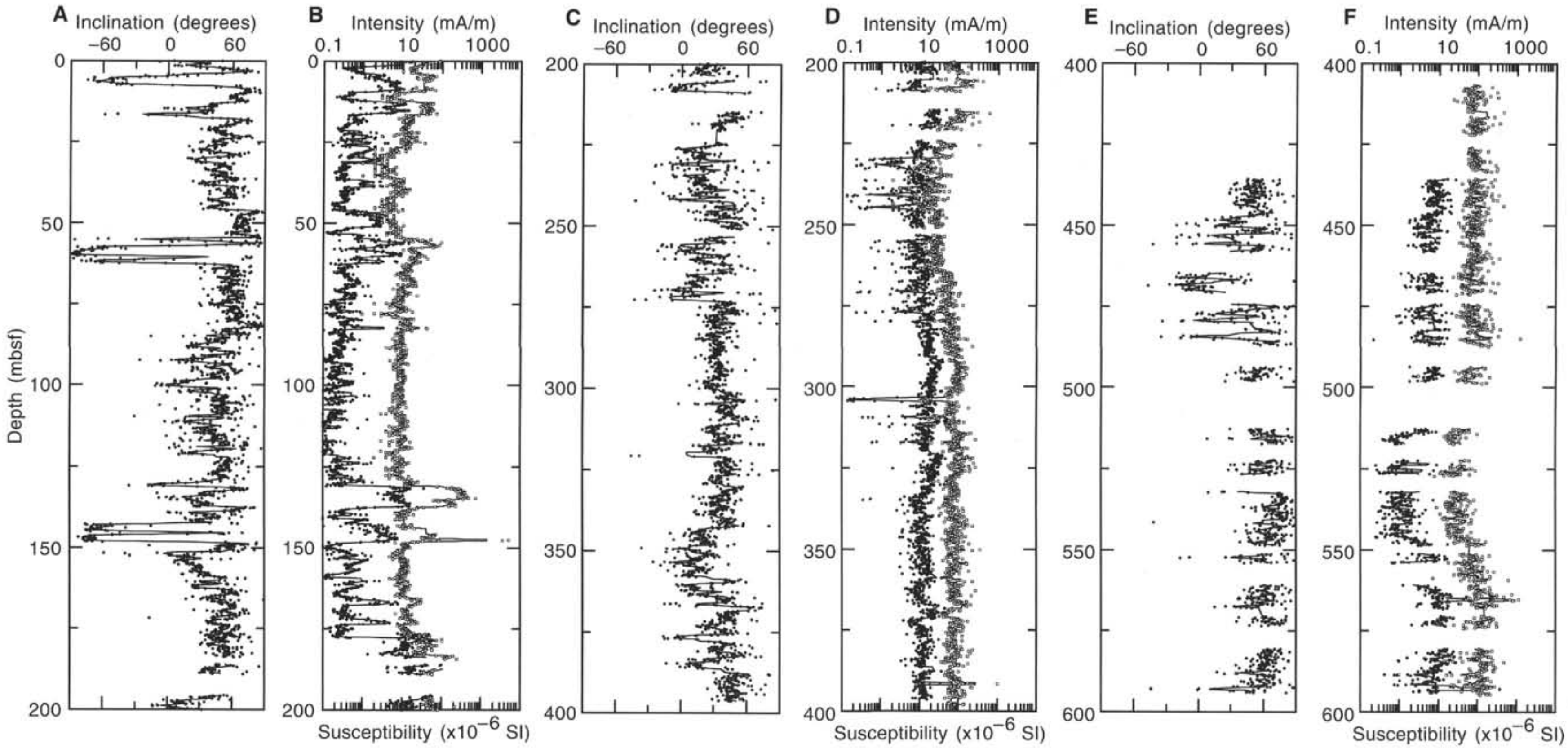

Figure 13. Magnetic data from APC and XCB cores from Site 955. **A, C,** and **E.** Inclination; connecting lines indicate smoothed inclination ($n = 7$). **B, D,** and **F.** 25 mT NRM intensity (filled circles) and susceptibility (open squares). Lines connecting data points indicate smoothed intensity ($n = 7$) and smoothed susceptibility ($n = 20$).

Table 4. Summary of volcanic components, Site 955.

Unit	Subunit	Core (top)	Depth (mbsf)	Age (Ma)	Period	Lithologies with volcanic components
I	a	1H	0.0	0.0	Post-Roque Nublo Tenerife	Foraminifer-lithic sand Volcanic ash and pumice
	b	19X-5	175	3.4		Quartz silts and sands with very minor volcanics
II		23X-2	207	3.9	Roque Nublo	None
III		29X-CC	273	6.1	Volcanic hiatus	Quartz silts and sands with very minor volcanics Rare zeolitized tuff
IV	a	40X-5	374	9.7	Fataga	Quartz silts and sands with lithics and crystals, zeolitized tuffs
	b	55X	513	13.3	Mogan	Crystal-vitric tuffs and pumiceous tuffs Basaltic tuffs
V		60X-5	567	14.1	Pre-Mogan	Basaltic lithic tuff and basalt clasts

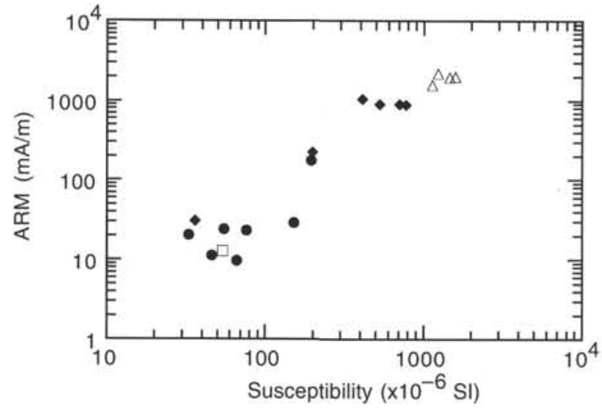

Figure 14. King diagram. ARM (filled circle = ooze, open square = marly ooze, filled diamond = marl, open triangle = mud) vs. weak field susceptibility.

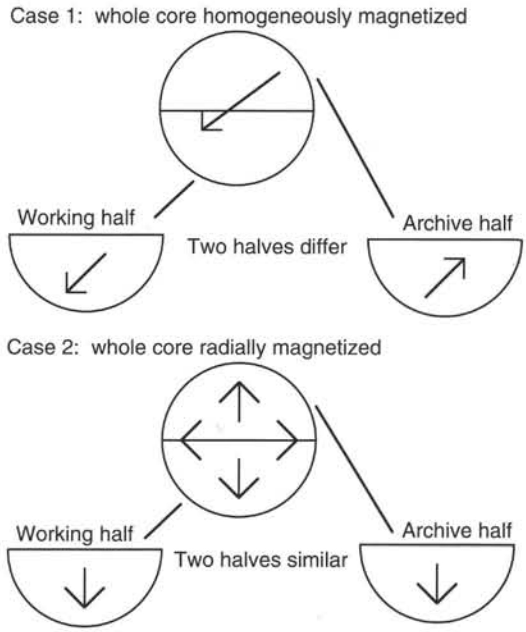

Figure 15. Test for detection of radial magnetization in drilled cores for long-core cryogenic measurements.

small crystals of deep green aegirine, biotite (Fig. 17), and minor amphibole (both alkali and dark brown varieties). The mineralogy and abundant trachyphonolite clasts indicate derivation from Fataga Group lava flows and ignimbrites.

The highly indurated tuffs in Subunit IVa are composed dominantly of fine-grained zeolite (phillipsite), presumably formed by alteration of felsic glass shards, with trace amounts of feldspar, green clinopyroxene, biotite, and amphibole. The mineralogy of these tuffs suggests that they are also related to Fataga Group volcanism. They were probably emplaced either as tephra fall associated with explosive eruptions or as the distal equivalents of pyroclastic flows that entered the sea.

Subunit IVb (513–567 mbsf) contains numerous felsic tuffs as well as one thick-bedded dominantly basaltic tuff (Sections 157-955A-60X-3 and 157-955A-60X-4). The felsic tuffs are composed chiefly of unaltered, colorless glass shards (Fig. 18) and pumice (Fig.19), with crystals of alkali feldspar and minor pale green clinopyroxene, alkali amphibole, and biotite. As discussed in the section on lithostratigraphy, two of these tuffs can be correlated with subaerial ignimbrites of the middle Mogan Group on Gran Canaria based on diagnostic mineralogical assemblages. The basaltic tuff is composed chiefly of coarse tachylitic ash particles together with minor felsic pumice. It is correlated with the 14 Ma P1 composite rhyolite-basalt ignimbrite of Gran Canaria (Schmincke, 1976) based on the presence of trace amounts of zircon and its stratigraphic position. Thus the volcaniclastic sediments in Subunit IVb are correlated with the highly explosive eruptions of peralkaline rhyolite of the Morgan Group.

Unit V (567–595 mbsf) is composed of fine-grained hemipelagic sediments with interbeds of nonvolcanic siltstone and sandstone, and minor crystal-lithic sands. Volcanic components in the crystal-lithic sands include basaltic lithic clasts, plagioclase, alkali feldspar, Ti-augite, and minor sideromelane. A basaltic lithic tuff in Section 157-955A-63X-CC is composed dominantly of tachylitic basalt fragments, plagioclase, and Ti-augite. Large clasts of aphyric to sparsely pyroxene-phyric basalt occur in this unit as well and were probably emplaced as a debris flow. The volcaniclastic sediments in this unit are largely derived from erosion of the subaerial basaltic shield of Gran Canaria during the period prior to the voluminous eruption of middle Miocene Mogan and Fataga Group ignimbrites.

Geochemistry

Major and trace element abundances were analyzed by XRF for four samples from Site 955. The results are given in Table 5. Analytical conditions and uncertainties are discussed in the "Igneous Petrology" section of the "Explanatory Notes." Samples were taken from the lower half of the sequence in Hole 955C (Cores 51X through 60X), as it contains most volcaniclastic sediments. The samples include a vitric tuff, two crystal-lithic sands, and a foraminifer sand with crystals. Thin sections were prepared from the chemically analyzed samples (see previous section for discussion).

Table 4 (continued).

Unit	Volcanic components		
	Rock fragments	Crystals	Vitric clasts
I	Minor basalt and trachyphonolite	Alkali feldspar, plagioclase > clinopyroxene > alkali amphibole	Very minor sideromelane
		Minor alkali feldspar, green clinopyroxene, alkali amphibole	Felsic glass shards and pumice
II			
III			
		Minor green clinopyroxene	
IV	Trachyphonolite and minor basalt	Alkali feldspar > clinopyroxene > biotite > amphibole	
		Alkali feldspar > clinopyroxene (minor)	Felsic glass shards and pumice
	Tachylitic basalt ash		Minor felsic pumice
V	Basalt (tachylite and crystalline)	Plagioclase > clinopyroxene > alkali feldspar > amphibole, biotite	Trace of sideromelane shards

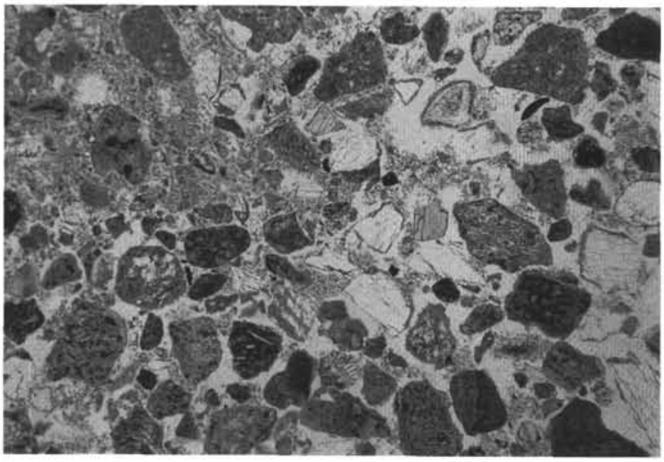

Figure 16. Photomicrograph of crystal-lithic sand showing rounded clasts of trachyphonolite tuff and lava, and crystals of alkali feldspar and clinopyroxene. Field of view is 8.0 mm wide. Sample 157-955A-42X-4, 83–84 cm.

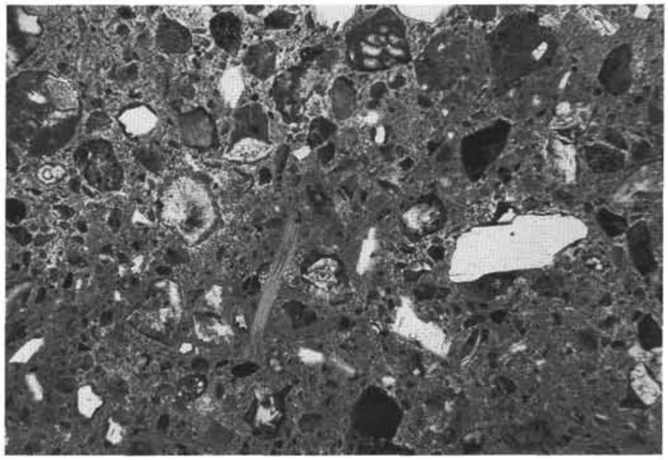

Figure 17. Photomicrograph of poorly sorted lithic-crystal-foraminifer sand showing crystals of alkali feldspar and biotite. Field of view is 8.0 mm wide. Sample 157-955A-43X-1, 97–98 cm.

The major and trace element compositions for volcaniclastic sediments from Unit IV are similar to those at Site 953, which were derived from the middle Miocene Fataga and Mogan Group ignimbrites. The crystal-lithic sand from Subunit IVa (interval 157-955A-51X-5, 80–82 cm) has a major element composition that falls within the range for Fataga trachyphonolites. It also has high incompatible trace element abundances, low V, Ni, and Cr, and a relatively low Zr/Nb ratio of 3.5. The other sample from Subunit IVa (interval 157-955A-52X-2, 116–118 cm) is a clayey foraminifer sand with crystals and minor lithics, and it has a high CaO content due to biogenic calcium carbonate. Recalculation of the analyses to a $CaCO_3$-free basis (see "Site 953," this volume) yields a major and trace element composition that also is similar to Fataga Group trachyphonolites.

A sample of vitric tuff with minor biogenic material from Subunit IVb (interval 157-955A-58X-2, 122–124 cm) has lower Al_2O_3 and alkalies, and higher MgO, than the samples from Subunit IVa at comparable SiO_2 contents. This sample also has higher Zr, lower Nb, and a Zr/Nb ratio of 6.9. All of these characteristics indicate that the tuff is related to the Mogan Group ignimbrites, consistent with the thin section observations discussed above.

The basaltic crystal-lithic tuff from Unit V (Section 157-955A-60X-CC) has a major and trace element composition similar to the Miocene basalts from Gran Canaria (Hoernle and Schmincke, 1993). It has moderately high Ni (292 ppm) and Cr (320 ppm), despite the absence of olivine, and a Zr/Nb ratio (6.4) that is similar to many of the basalts recovered from the lower part of the sequence at Site 953. It contains negligible biogenic material.

INORGANIC GEOCHEMISTRY

Introduction and Operation

A total of 29 interstitial-water samples were taken between 5.95 and 586.12 mbsf at Site 955 (Table 6). The sampling strategy and analytical methods were identical to those employed at Sites 950–954 (see "Explanatory Notes," this volume). Samples were analyzed for pH, salinity, chlorinity, alkalinity, sulfate, ammonia, sodium, potassium, silica, calcium, and magnesium. The bulk mineralogies of some samples were determined qualitatively by XRD analysis.

Changes in pore-water composition are driven by the bacterially mediated oxidation of organic matter from organic-rich sediments, precipitation of dolomite, dissolution of biogenic silica, and diagenetic reactions in the siliciclastic fraction, particularly the appearance of smectites and zeolites forming at the expense of volcanic glass. Lateral or vertical advection of evaporite-derived brines may be responsible for abnormally high salinities at depth.

Sulfate, Ammonia, and Alkalinity

Interstitial water SO_4^{2-} displays a classic linear diffusion profile, extrapolating from seawater values (28.9 mmol/L) at the sediment/water interface to trace concentrations (<1 mmol/L) at the onset of bacterially mediated sulfate reduction around 60 mbsf. Below this, sulfate concentrations remain negligible down to the bottom of the hole. The continued presence of trace sulfate throughout the sequence might reflect remnant seawater sulfate or

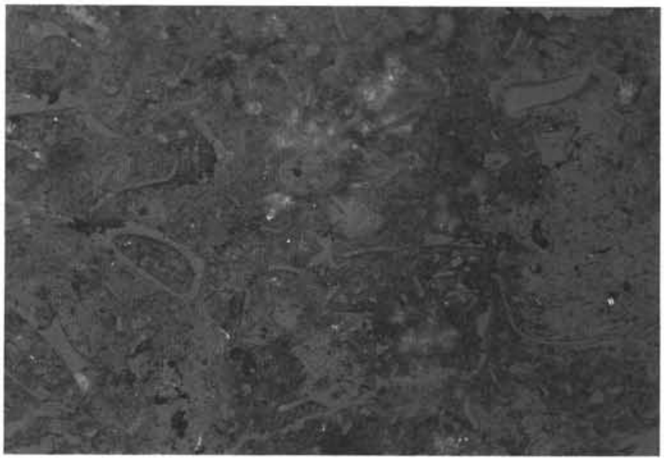

Figure 18. Photomicrograph of vitric tuff showing abundant glass shards. Field of view is 1.0 mm wide. Sample 157-955A-58X-2, 126–127 cm, reflected light.

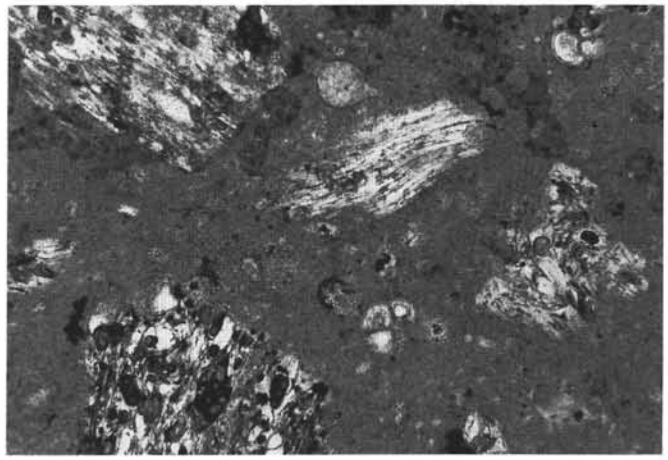

Figure 19. Photomicrograph of pumice clasts in a poorly sorted sand with abundant fine-grained matrix of clay and nannofossils. Field of view is 2.0 mm wide. Sample 157-955A-57X-2, 49–50 cm.

may be an artifact caused by oxidation of H_2S or other reduced sulfur phases during sampling. The sulfate profile at Site 955 has the steepest gradient and reaches the lowest minima of any site studied on Leg 157, indicating that sulfate reduction rates are greatest in this study area.

Methane, which appears at high concentrations along with traces of ethane at the sulfate minimum around 60 mbsf (see "Organic Geochemistry," this chapter), peaks at about 20,000 ppmv between 90 and 200 mbsf and then falls back to near 5000 ppmv through the remainder of the section. Active methanogenesis is occurring throughout the sequence, providing a source of CH_4 that is diffusing up to the top of the sulfate reduction zone where it is being oxidized.

Predictably, decreasing sulfate in the uppermost beds is matched by increasing alkalinity and ammonia production. Alkalinity increases from 4.7 mmol/L at 6 mbsf (significantly higher than the 2.3 mmol/L seawater value), to a maximum of 10.8 mmol/L at 42–52 mbsf (Fig. 20), below which concentrations decline exponentially, falling to <1 mmol/L below 360 mbsf. High alkalinity in the upper beds may be attributed to H_2S and HCO_3^- production accompanying sulfate reduction. As at the MAP sites, the alkalinity maximum occurs above the sulfate and calcium minima and the ammonia maximum, indicating that carbonate precipitation at and below 60 mbsf is consuming alkalinity.

Ammonia increases progressively from 150 to 1900 µmol/L between 6 and 90 mbsf (Fig. 20) and then decreases smoothly to 508 µmol/L in the deepest sample. The typical inverse linear relationship between sulfate and ammonia (Fig. 21) is well displayed in the upper 60 m. Declining NH_4 below 60 mbsf indicates gradual uptake at depth, probably caused by reactions involving diagenetic clay minerals.

Chloride and Salinity

Salinity decreases from seawater values (35 g/kg) in the upper 15 m to a minimum of 34 g/kg at 30–80 mbsf (Fig. 22) and then climbs steadily to a maximum of 54 g/kg around 525 mbsf. Low salinities near the top of the sequence may be attributed to Ca, Mg (discussed below), and SO4 depletion accompanying sulfate reduction.

Chloride shows a regular increase with depth, from seawater concentrations in the uppermost 15 mbsf to a maximum of 945 mmol/L at 525 mbsf before falling back to 920 mmol/L toward the base of the hole. The decrease in chlorinity below 525 mbsf could result from the release of chemically bound water from clay minerals. However,

Table 5. XRF major and trace element analyses of whole-rock samples, Site 955.

Hole, core, section:	955A-51X-5	955A-52X-2	955A-58X-2	955A-60X-CC
Interval (cm):	80–82	116–118	122–124	23–25
Depth (mbsf):	481.2	486.76	544.32	568.43
Lithologic unit:	IVa	IVa	IVb	V
Major elements (wt%)				
SiO_2	59.95	46.47	59.23	49.18
TiO_2	1.02	0.75	0.83	4.58
Al_2O_3	16.49	12.70	13.29	14.90
Fe_2O_3	3.60	2.97	4.90	11.56
MnO	0.08	0.06	0.16	0.12
MgO	0.59	0.48	1.60	4.57
CaO	6.82	27.07	13.24	8.70
Na_2O	6.37	4.39	3.52	3.36
K_2O	4.84	3.13	3.00	1.71
P_2O_5	0.09	0.14	0.15	0.52
Total	99.85	98.16	99.94	99.21
LOI	8.97	20.38	14.12	2.18
Trace elements (ppm)				
Cr	10	28	35	320
Ni	47	19	20	292
Cu	12	12	17	97
V	52	52	62	360
Zn	76	80	164	155
Sr	246	724	517	715
Ba	2074	1156	260	1037
Rb	70	53	85	27
Y	24	31	62	32
Zr	609	735	943	448
Nb	174	145	136	70
Ce	228	205	247	91
Zr/Nb	3.5	5.1	6.9	6.4

high salinities and chlorinities have been observed in many DSDP sites off the coast of northwestern Africa (Gieskes, 1981) where these high values have been attributed to penetration by saline fluids derived from leaching of underlying evaporites, or the lateral influx of continental ground waters that have previously leached coastal evaporites. Pore waters from Site 415 (Gieskes et al., 1980) display a chlorinity maximum of similar concentration and at a similar depth to that identified at Site 955; low sulfate concentrations at the latter site would imply a halite-dominated source.

Sodium and Potassium

Sodium (Fig. 23) displays a similar trend to salinity and chlorinity, although significant enrichment occurs only below 150 mbsf. By contrast, pore-water potassium concentrations decline linearly from

Table 6. Interstitial-water geochemistry, Hole 955A.

Core, section, interval (cm)	Depth (mbsf)	pH	Salinity (g/kg)	Cl (mmol/L)	Alkalinity (mmol/L)	SO_4 (mmol/L)	NH_4 (μmol/L)	Na (mmol/L)	K (mmol/L)	SiO_2 (μmol/L)	Ca (mmol/L)	Mg (mmol/L)	Mg/Ca (molar ratio)
157-955A-													
1H-4, 145–150	5.95	7.41	35.0	557	4.69	23.7	149	490	11.5	593	9.20	50.7	5.51
2H-4, 145–150	14.05	7.36	35.0	560	5.84	22.7	380	496	11.6	586	8.62	50.7	5.88
3H-4, 145–150	23.55	7.30	34.5	562	8.20	17.1	911	515	11.6	686	6.41	47.1	7.34
4H-4, 145–150	33.05	7.27	34.0	576	10.1	10.8	1230	516	10.9	727	5.56	44.4	7.99
5H-4, 145–150	42.55	7.33	34.0	579	10.8	6.74	1470	505	10.8	780	5.12	41.0	8.00
6H-4, 145–150	52.05	7.58	34.0	585	10.8	3.57	1620	483	10.4	789	4.80	36.7	7.64
7H-4, 145–150	61.55	7.72	34.0	588	10.5	0.39	1650	492	10.5	727	4.38	34.0	7.76
8H-4, 145–150	71.05	7.82	34.0	596	6.31	3.24	1840	504	10.2	798	5.04	34.3	6.80
9H-4, 145–150	80.55	7.62	34.0	595	10.1	0.22	1840	509	9.76	743	5.16	33.7	6.53
10H-4, 145–150	90.05	7.45	34.5	612	9.69	0.21	1930	476	9.32	917	5.51	31.0	5.63
12H-4, 145–150	109.05	7.58	36.0	613	7.44	0.47	1850	490	8.35	767	5.94	31.0	5.22
14H-4, 145–150	128.05	7.59	36.0	637	3.52	0.07	1810	498	8.69	397	5.65	31.6	5.60
16H-5, 145–150	148.60	7.55	36.0	651	3.14	0.23	1550	519	7.85	253	6.79	33.0	4.86
18H-4, 140–150	166.00	7.79	38.0	674	1.89	0.38	1590	533	7.83	172	7.46	33.0	4.42
20X-5, 150–155	183.90	7.45	40.0	686	2.03	0.32	1480	543	7.02	154	8.98	34.2	3.81
23X-2, 140–150	208.00	7.58	40.0	714	1.17	0.27	1360	553	6.18	132	10.7	34.3	3.20
26X-5, 140–150	241.40	7.31	41.5	730	1.18	0.77	1130	631	5.72	154	13.2	35.1	2.66
29X-4, 140–150	268.90	7.40	42.0	756	1.29	0.93	1170	640	5.36	141	15.1	34.9	2.31
32X-4, 140–150	297.60	7.18	44.0	770	1.11	0.56	1060	643	5.03	136	17.4	33.6	1.94
35X-4, 140–150	325.08	7.34	45.5	799	1.03	0.61	919	666	5.50	214	21.3	33.4	1.57
38X-5, 140–150	356.50	7.33	44.0	823	1.02	0.55	892	703	5.89	103	25.2	31.0	1.23
41X-5, 140–150	385.30	7.43	49.0	859	0.56	0.39	867	775	5.65	158	32.3	31.9	0.99
44X-5, 135–150	414.15	7.47	52.0	862	0.51	0.43	802	729	5.52	86	34.1	25.5	0.75
47X-5, 135–150	443.15	7.11	52.0	899	0.89	0.69	799	747	5.27	134	41.0	22.8	0.56
50X-3, 135–150	469.15	7.61	52.0	897	0.40	0.90	625	757	5.08	198	46.7	18.7	0.40
53X-2, 135–150	496.65	7.86	54.0	925	0.54	0.87	671	762	5.32	269	53.7	14.3	0.27
56X-2, 140–150	525.30	7.82	54.0	945	0.79	0.75	612	786	5.57	308	55.1	13.7	0.25
59X-5, 130–150	558.50	8.01	54.0	940	0.28	0.68	582	785	5.16	220	54.7	14.1	0.26
62X-5, 103–123	586.12	8.18	52.5	921	0.45	1.51	508	819	4.68	106	62.4	13.1	0.21

slightly greater (11.5 mmol/L) than seawater values at 6 mbsf, to 5.0 mmol/L at ~300 mbsf. Highly altered zeolitic tuffs occur in the lower part of the sequence at Site 955, so it is likely that the pore-water trend reflects diffusion of potassium from seawater and uptake by phillipsite that is forming diagenetically below 300 mbsf.

Minor variations in potassium concentrations (4.7–5.9 mmol/L) below 300 mbsf may relate to local diagenetic effects caused by varying proportions of volcaniclastic sediments interbedded with hemipelagic muds. No large-scale uptake of potassium occurs between 300–590 mbsf, confirming the importance of sediment-hosted rather then basement-related processes in controlling potassium uptake at this site.

Silica

The pore-water silica profile at Site 955 is smooth relative to the other sites studied. Silica climbs sharply from high surficial values of 600 μmol/L at 6 mbsf to a maximum of 920 μmol/L at 90 mbsf (Fig. 24) before declining markedly to a minimum of 130 μmol/L around 200 mbsf. Between 200 and 300 mbsf, silica fluctuates around 150 μmol/L with a broad peak of >300 μmol/L at 525 mbsf.

The silica maximum around 90 mbsf occurs within clayey nannofossil mixed sediments and oozes yielding diatoms and is attributable to the dissolution of biogenic opal in these sediments. Low concentrations of pore-water silica in the middle of the sequence are correlated with the appearance of diagenetic smectites and phillipsite. Higher values below 300 mbsf are associated with the occurrence of felsic volcanic glasses in the section.

Magnesium and Calcium

Calcium decreases from lower than seawater values of 9.2 mmol/L (Fig. 25) at 6 mbsf to a marked minimum of 4.4 mmol/L at 60 mbsf, indicating Ca^{2+} uptake into the solid phase at this level. Below this, concentrations increase progressively reaching a maximum of 62 mmol/L in the bottom sample. The Ca^{2+} minimum coincides with the base of the upper alkalinity peak and the top of the pore-water sulfate minimum, which is consistent with carbonate precipitation at the top of the sulfate reduction zone. High calcium concentrations in pore waters at the base of the sequence are a consequence of the dissolution of volcanic glasses and possibly the introduction of evaporite-derived brines.

Magnesium contents decline sharply from lower than seawater values of 50.7 mmol/L at 6 mbsf (Fig. 25) to a minimum of 31 mmol/L around 100 mbsf. Below this, Mg^{2+} concentrations increase gradually to a maximum of 35 mmol/L around 250 mbsf then decline again to 14 mmol/L at 500 mbsf, remaining at that level down to the base of the hole. A steep linear decline between the sediment/water interface and 60–100 mbsf is consistent with a diffusional supply of Mg^{2+} from seawater and uptake at that depth. The Mg/Ca ratio peaks around 40 mbsf, somewhat above the Ca^{2+} minimum and the change in gradient of the Mg^{2+} profile. Together, these trends suggest that dolomite precipitation, which XRD data demonstrate appears in abundance between 60 and 80 mbsf, is controlling carbonate equilibria in the upper 100 m at Site 955.

The temporary reversal in the general trend of Mg^{2+} depletion downhole might be caused by laterally advected magnesium-rich brines, or Mg^{2+} leaching of volcaniclastic debris exceeding magnesium uptake in the sediment. Below 300 mbsf, lower pore-water Mg^{2+} and increasing calcium concentrations probably result largely from diagenetic reactions within the silicate fraction, particularly the precipitation of smectites, which increase significantly below 400 mbsf.

ORGANIC GEOCHEMISTRY

The shipboard organic geochemistry program at Site 955 followed the same procedures as for previous sites, except for additional vacutainer sampling.

Volatile Hydrocarbons

Concentrations of methane (C_1) and ethane (C_2) gases were monitored in every core by the standard ODP headspace-sampling technique as part of the SSP program. The methane content increased from background levels of 2–3 ppmv to 5270 ppmv at 71 mbsf (Table 7). Levels stayed high (12,000–36,000 ppmv) in the 90–200 mbsf interval (Fig. 26) before dropping to 2000–10,000

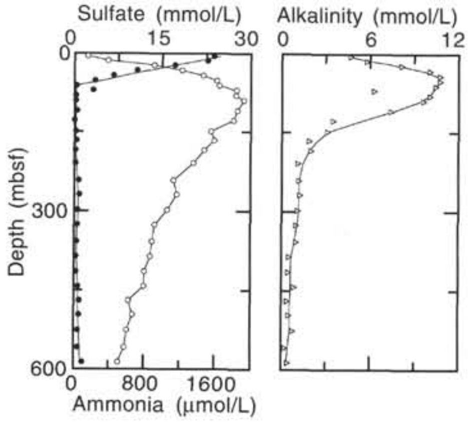

Figure 20. Interstitial-water sulfate (filled circles), ammonia (open circles), and alkalinity, Hole 955A.

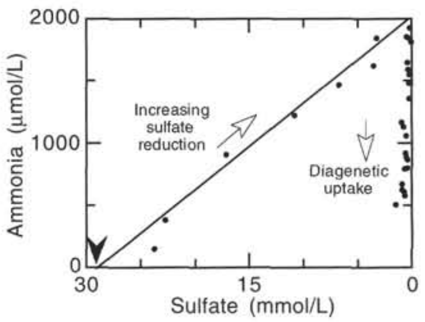

Figure 21. Inverse relationship between interstitial-water ammonia and sulfate, Hole 955A (filled arrowhead indicates seawater value).

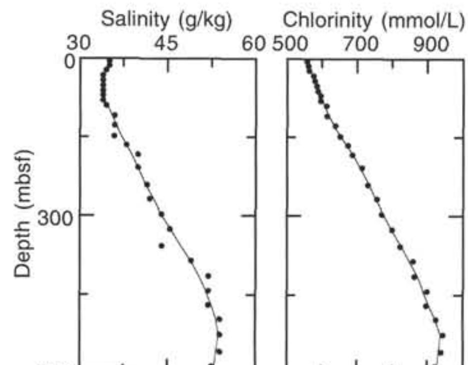

Figure 22. Interstitial-water salinity and chlorinity, Hole 955A.

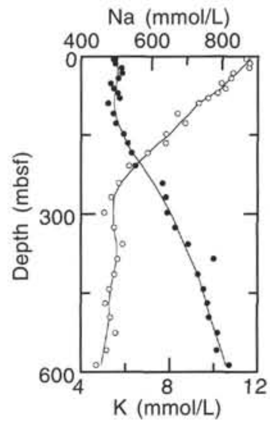

Figure 23. Interstitial-water sodium (filled circles) and potassium (open circles), Hole 955A.

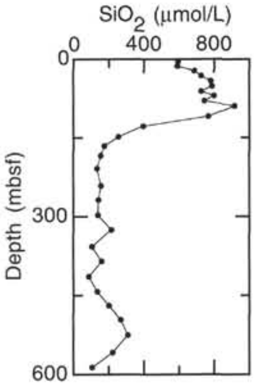

Figure 24. Interstitial-water silica, Hole 955A.

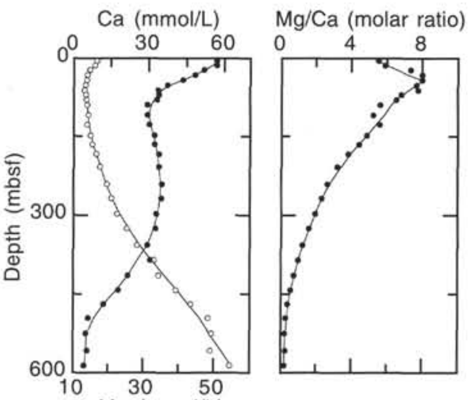

Figure 25. Interstitial-water calcium (open circles), magnesium (filled circles), and Mg/Ca ratio at Site 955.

ppmv for the remainder of the sequence. Unusually high values of 37,700 and 5000 ppmv were recorded at 441 and 516 mbsf, respectively. Ethane was also detected; C_1/C_2 ratios varied between 1000 and 8100 from 71 mbsf to the bottom of the hole.i No downhole increase was discernible (Fig. 26).

Cores sometimes showed cracks and gas pockets through the core liner on the catwalk. Most of the time these pockets were partly filled with water, preventing the extraction of uncontaminated gas samples, but in a few cores pure gas pockets could be sampled by the vacutainer method. This gas was analyzed on the NGA instrument, and both methane and ethane were detected but no higher hydrocarbons were found. The C_1/C_2 ratio was constant around 3300–3800. The high gas content of the sediments was also demonstrated by the pervasive presence of small fractures seen in the newly split cores.

The high levels of methane seen through most of the sequence at Site 955 probably originated from in-situ bacterial processes in the sediments, because no increasing trend with depth was observed that

Table 7. Methane and ethane concentrations (ppmv) in headspace samples, Hole 955A.

Core, section, interval (cm)	Depth (mbsf)	C_1	$C_{2=}$	C_2	C_1/C_2
157-955A-					
1H-5, 0–5	6.03	3			
2H-5, 0–5	14.13	2			
3H-5, 0–5	23.63	2			
4H-5, 0–5	33.13	2			
5H-5, 0–5	42.63	3			
6H-5, 0–5	52.13	2			
7H-5, 0–5	61.63	12			
8H-5, 0–5	71.13	5,270		1	5270
9H-5, 0–5	80.63	7,330		1	7330
10H-5, 0–5	90.13	20,800		3	6940
11H-5, 0–5	99.63	19,900		3	6640
12H-5, 0–5	109.13	12,300		2	6170
13H-6, 0–5	120.13	25,000	1	5	5000
14H-5, 0–5	128.13	15,000	1	3	5010
15H-6, 0–5	139.13	29,800	1	7	4260
16H-6, 0–5	148.63	20,900	0	4	5230
17H-6, 0–5	158.13	36,100	0	8	4510
18H-6, 0–5	167.63	20,700	1	4	5180
19X-6, 0–5	176.43	24,000	0	5	4800
20X-6, 0–5	183.93	27,000	0	6	4420
21X-2, 0–5	187.53	19,800	0	5	3960
22X-5, 0–5	201.53	22,300	0	7	4610
23X-3, 0–5	208.13	11,900	0	4	2970
24X-4, 0–5	219.13	11,300	0	3	3750
25X-6, 0–5	231.83	9,850	0	3	3280
26X-6, 0–5	241.53	1,030		1	1030
27X-5, 0–5	249.63	4,720		1	4720
28X-5, 0–5	259.33	8,500		2	4250
29X-5, 0–5	269.03	11,100		3	3690
30X-4, 0–5	277.23	11,100		3	3700
31X-5, 0–5	288.23	3,830		1	3830
32X-5, 0–5	297.73	6,700		2	3350
33X-5, 0–5	307.23	7,400		2	3700
34X-5, 0–5	316.83	7,830		2	3920
35X-5, 0–5	326.43	5,370		2	2690
36X-5, 0–5	336.13	2,980		1	2980
37X-5, 0–5	345.63	3,020		1	3020
38X-6, 0–5	356.63	3,758		2	1880
39X-6, 0–5	366.23	1,770		1	1770
40X-6, 0–5	375.83	10,600		3	3530
41X-6, 0–5	385.43	5,700		2	2850
42X-6, 0–5	395.03	6,930		2	3460
44X-6, 0–5	414.33	2,240		1	2240
45X-4, 0–5	421.03	3670		1	3670
46X-5, 0–5	432.23	3,850		1	3850
47X-5, 0–5	441.83	37,700		7	5380
48X-5, 0–5	451.53	2,680		1	2680
49X-5, 0–5	461.23	4,900		1	4900
50X-5, 0–5	470.83	6,840		1	6840
51X-5, 0–5	480.43	7,920		1	7920
52X-5, 0–5	490.13	8,120		1	8120
53X-2, 130–135	496.63	2,730		1	2730
55X-3, 0–5	515.93	55,000		8	6870
56X-6, 0–5	529.93	5,160		3	1720
57X-6, 0–5	539.53	9,480		2	4740
58X-6, 0–5	549.13	5,160		3	1720
59X-6, 0–5	558.73	16,800		3	5600
60X-6, 0–5	567.73	25,700		3	8560
61X-2, 0–5	572.03	2,040		0.5	4080
62X-2, 0–5	581.73	4,890		0.5	9780
63X-3, 0–5	592.83	7,190		1	7190

might indicate other origins. On the contrary, the highest concentrations occurred at the summit of the methanogenic zone in the interval 90–200 mbsf.

Carbon, Nitrogen, and Sulfur Concentrations

A total of 180 carbonate determinations were made at Site 955, assisting the lithostratigraphic subdivision of the succession (see "Lithostratigraphy," this chapter) as at the previous sites. Representative samples were analyzed for organic carbon, nitrogen, and sulfur on the CNS instrument. Results of 36 determinations are presented in Figure 27 and Table 8. Organic carbon generally varies between 0.04% and 2%, with maximum value at 38 mbsf (2.59%). Nitrogen varies between 0.03% and 0.19% and appears to follow the organic carbon values. Sulfur also generally covaries with organic carbon, ranging from below detection to 1.00%.

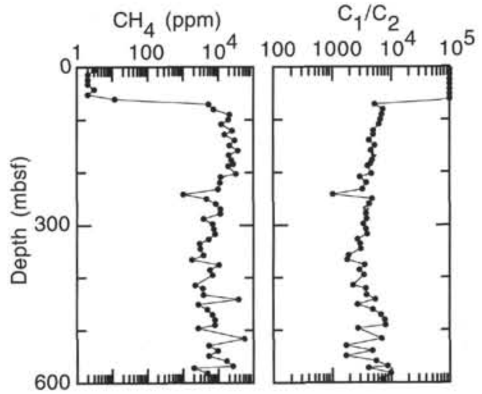

Figure 26. Methane concentrations and methane/ethane (C_1/C_2) ratios in headspace samples, Hole 955A.

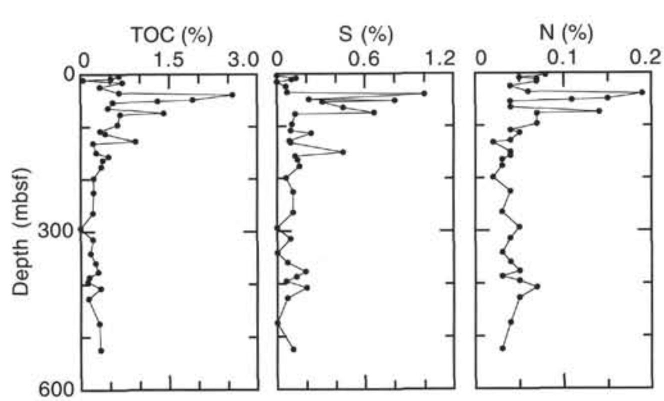

Figure 27. Concentration profiles of total organic carbon, total sulfur, and total nitrogen, Hole 955A.

Greenish sediments occurring in the slumped intervals from the upper part of the sequence exhibit the highest organic carbon values (Table 8) and are similar to those observed in organic-rich turbidites at other sites. Below 180 mbsf, organic carbon remains between 0.13% and 0.35% down to the bottom of the hole at 524 mbsf. There is no apparent correlation between organic carbon and methane content in the sediments, although higher values of both are found in the upper part of the hole. The highest organic carbon values occur at shallower depths (0–100 mbsf) than the highest methane values (80–200 mbsf).

In the upper part of the hole, C/N values are generally between 10 and 20 (Table 8), suggesting that a terrigenous component is mixed into the sediments. A high C/N spike at 128 mbsf (Fig. 28) may relate to samples containing woody material; land plant fragments were observed in several cores. C/N ratios tend to be below 10 in the lower part of the hole, which is consistent with a largely marine source for the organic matter here. However, organic carbon contents are low and clay mineral diagenesis may influence the C/N ratio.

PHYSICAL PROPERTIES

Introduction

The shipboard physical properties measurements program at Site 955 included nondestructive measurements of bulk density, bulk magnetic susceptibility, natural gamma and *P*-wave velocity on whole sections of core using the MST, as well as point measurements

Table 8. Elemental and organic carbon compositions of core samples, Hole 955A.

Core, section, interval (cm)	Depth (mbsf)	Inorganic carbon (wt%)	$CaCO_3$ (wt%)	Total carbon (wt%)	TOC (wt%)	Total nitrogen (wt%)	Total sulfur (wt%)	C/N
157-955A-								
1H-3, 50–51	3.50	6.49	54.1	7.14	0.65	0.08	BD	8.1
1H-6, 23–24	7.73	5.42	45.1	5.93	0.51	0.05	0.13	10.2
2H-2, 100–101	10.60	8.10	67.5	8.14	0.04	0.07	0.10	0.6
2H-6, 42–43	16.02	3.19	26.6	3.89	0.70	0.07	0.00	10.0
3H-5, 20–21	23.80	6.53	54.4	6.85	0.32	0.04	0.06	8.0
4H-6, 64–65	35.24	8.36	69.6	9.01	0.65	0.06	0.07	10.8
5H-2, 60–61	38.70	3.67	3.6	6.26	2.59	0.19	1.00	13.6
6H-2, 88–89	48.48	6.15	51.2	8.06	1.91	0.15	0.22	12.7
6H-4, 38–39	50.98	5.73	47.7	7.04	1.31	0.11	0.80	11.9
6H-5, 145–146	53.55	5.98	49.8	6.53	0.55	0.04	0.31	13.8
7H-6, 118–119	64.28	6.62	55.1	7.07	0.45	0.04	0.45	11.3
8H-6, 136–137	73.96	4.48	37.3	5.88	1.40	0.14	0.66	10.0
9H-2, 139–140	77.49	6.95	57.9	7.62	0.67	0.07	0.12	9.6
11H-2, 92–93	96.02	6.45	53.7	7.07	0.62	0.07	0.10	8.9
12H-4, 110–111	108.70	7.18	59.8	7.50	0.32	0.04	0.09	8.0
13H-1, 80–81	113.40	5.27	43.9	5.68	0.41	0.05	0.23	8.2
14H-4, 100–101	127.60	6.82	56.8	7.75	0.93	0.04	0.08	23.3
15H-1, 50–51	132.10	5.60	46.6	5.80	0.20	0.02	0.09	10.0
16H-7, 17–18	150.32	5.94	49.5	6.20	0.26	0.04	0.45	6.5
17H-5, 40–41	157.00	5.77	48.1	6.24	0.47	0.04	0.12	11.8
18H-3, 120–121	164.30	6.92	57.6	7.29	0.37	0.03	0.14	12.3
20X-1, 70–71	177.10	5.39	44.9	5.74	0.35	0.03	0.15	11.7
22X-3, 39–40	198.89	7.15	59.6	7.37	0.22	0.02	0.06	11.0
25X-2, 13–14	225.93	5.89	49.1	6.11	0.22	0.04	0.11	5.5
29X-2, 51–52	265.01	5.70	47.5	5.91	0.21	0.03	0.11	7.0
32X-2, 8–9	293.28	4.61	38.4	3.52	BD	0.05	BD	ND
34X-3, 70–71	314.50	2.97	24.7	3.17	0.20	0.04	0.09	5.0
37X-2, 67–68	341.77	2.71	22.6	2.87	0.16	0.03	BD	5.3
39X-1, 68–69	359.38	2.57	21.4	2.82	0.25	0.04	0.07	6.3
40X-6, 98–99	376.78	2.91	24.2	3.20	0.29	0.05	0.19	5.8
41X-6, 85–86	386.25	2.55	21.2	2.69	0.14	0.03	0.13	4.7
42X-6, 45–46	395.45	1.96	16.3	2.08	0.12	0.05	0.06	2.4
44X-1, 28–29	407.08	2.28	19.0	2.61	0.33	0.07	0.20	4.7
46X-1, 53–54	426.73	3.36	28.0	3.49	0.13	0.05	0.07	2.6
51X-1, 21–22	474.61	2.00	16.7	2.31	0.31	0.04	BD	7.8
56X-2, 55–56	524.45	1.84	15.3	2.17	0.33	0.03	0.11	11.0

Note: BD = below detection.

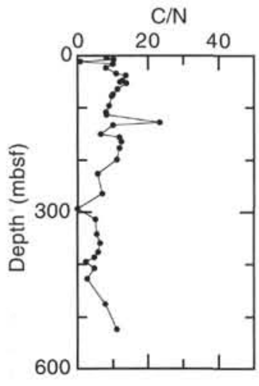

Figure 28. C/N ratio plotted against depth for samples, Hole 955A.

of *P*-wave velocity parallel and perpendicular to the core axis, shear strength, and index properties. The core below about 80 mbsf was disturbed by cracks and fractures caused by expansion of gas that disrupted the fabric of the core. These cracks made it impossible to determine compressional-wave velocities either with the MST, DSV or Hamilton Frame. While it was possible to complete strength measurements, the disruption of the sediment framework by gas expansion certainly weakened the cores. The strength values estimated by the vane shear and penetrometer techniques are probably substantially less than in-situ values. Similarly, since the GRAPE density, magnetic susceptibility, and natural gamma are all volume dependent characterizations, these measurements have been influenced by the introduction of voids into the cores. Local trends may still reflect in-situ variations. Absolute comparison to other cores or even between segments of these cores is not recommended.

Whole-core Measurements

MST

Whole-round measurements of GRAPE density and magnetic susceptibility were made on all cores throughout Hole 955A. *P*-wave velocity measurements were made on cores down to about 137.5 mbsf. Velocity measurements were discontinued below this depth because the extensive gas expansion fractures prevented transmission of sound energy through the core. The influence of these fractures is evident in Figure 29 as an increased scatter in the raw data points below ~80 mbsf. Figures 30, 31, and 32 show data from the GRAPE density, natural gamma, and magnetic susceptibility sensors. To save time, the sample spacing on the natural gamma was changed from 30 cm to 50 cm at about 120 mbsf. Increased variation introduced by gas expansion required all data to be filtered with a 0.5 m running median filter to eliminate spikes. This variation is indicated by increased scatter in the raw data for the GRAPE below about 110 mbsf (Fig. 30) and for magnetic susceptibility below about 220 mbsf (Fig. 32). Intervals longer than the filter length without data are indicated by gaps in the curves.

For comparison, each of the MST data sets is plotted at a common scale in Figures 32 through 35 for ranges 0–200, 200–400, and 400–595 (total depth) mbsf, respectively. The four individual curves do not indicate significant covariation between the different signals. This is reinforced by the crossplots in Figure 36. Only density and velocity show what appears to be a significant correlation. The remainder of the plots show indistinct clouds, suggesting the near independence of the plotted characters.

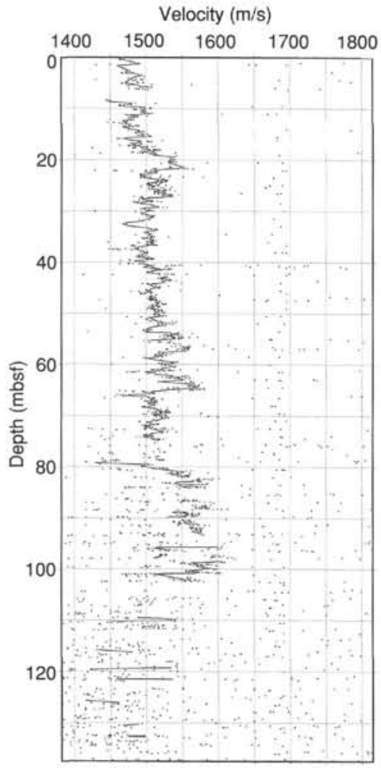

Figure 29. MST velocity, Hole 955A. Filtered data indicated by lines, raw data by discrete points.

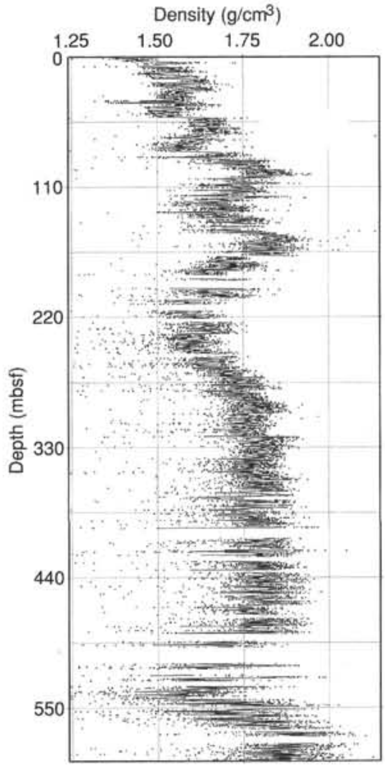

Figure 30. MST density, Hole 955A. Filtered data indicated by lines, raw data by discrete points.

Split-core Measurements

Measurements made on the split core include index properties (wet- and dry-bulk density, water content, grain density, porosity, and void ratio; Fig. 37), compressional-wave velocity (Fig. 38), shear strength (Fig. 39), and thermal conductivity (Fig. 39). Core recovery in this hole was good and resulted in a continuous set of physical properties measurements.

Index Properties

Index properties were determined from discrete samples by gravimetric methods in each core throughout Hole 955A. Calculations of index properties have been made following Methods B and C (see "Explanatory Notes" this volume). Although some variation in the values calculated by the different methods clearly exists, this difference is particularly noticeable with grain density (see "Site 950," this volume). Method B was chosen for determination of the bulk density (Fig. 37) and Method C was utilized for the remainder of the determinations.

Values of the index properties from Hole 955A are presented in Table 9. The downhole trends seen in Figure 37 show an overall decrease in water content and porosity (Fig. 37) by about 30%, and a corresponding increase in bulk density (Fig. 37), from the mud line to 170 mbsf, lower limit of lithologic Subunit IA (see "Lithostratigraphy," this chapter). Between this level and about 210 mbsf the increased amount of sand and silt interbeds within Subunit IB produces noticeable variations on all measured index properties, although a general increasing trend in water content and decrease in density is observed. Downhole, Units II and III show a continuous trend of decreasing water content and porosity and increasing density down to 380 mbsf. Part of this downcore trend, especially on the upper part of the interval (between 220 and 300 mbsf) may be the result of distortion of the cored segments by the confining pressure of extraction from the seafloor. Silt and sand interbeds become more common toward the base of Unit III and downhole. This is reflected again by larger variations in the index properties, typically by peaks of high water content and low bulk density corresponding to water-saturated sand intervals and volcaniclastic deposits. In contrast, the grain density trend downcore shows a very different profile (Fig. 37) on which the only changes result from the general increase of silt and sand interbeds below Unit II, and coarse-grained volcanic intervals toward the base of Hole 955A, within lithologic Units IV and V.

P-wave Velocity

The DSV penetration transducers were used to determine the *P*-wave velocity of the core from 0.24 mbsf to 85 mbsf. Approximately one sample per section was obtained between Cores 1H and 9H. Deeper in the section, insertion of the transducers split the core, which disrupted coupling between the transducers and the sample, making further measurements with this device impossible. It was possible to measure velocities with the Hamilton Frame occasionally on some samples above 120 mbsf and down to Core 13H. Below this depth gas expansion fractures disrupted the sediment framework, making further measurements impossible and perhaps explaining some of the anomalously low velocities listed in Table 10. All the compressional velocities determined with either the Hamilton Frame or the DSV above 120 mbsf are plotted in Figure 38. The continuity of the curve, independent of the measuring apparatus, suggests that the influence of the core liner on the Hamilton Frame measurements

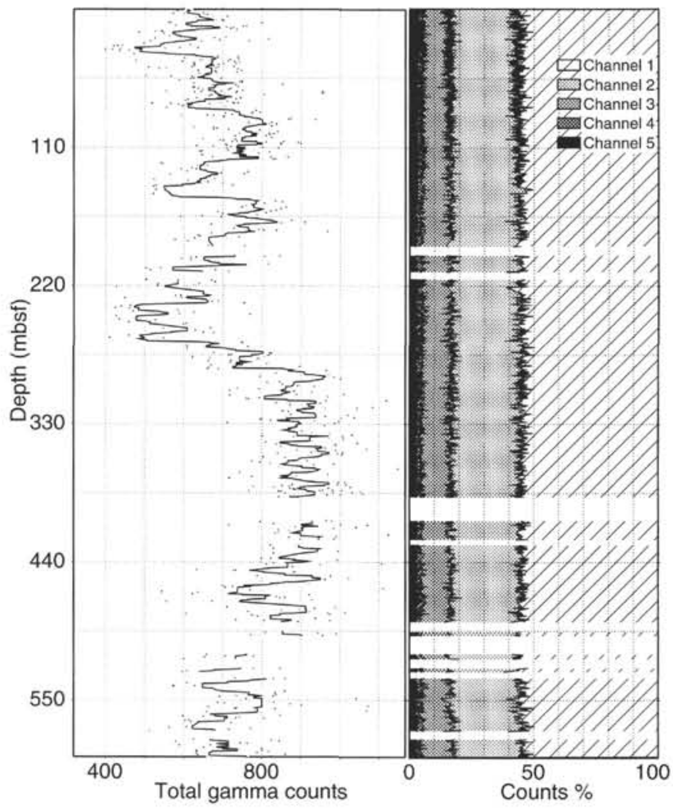

Figure 31. MST total natural gamma ray and percentage counts by channel, Hole 955A. Filtered data indicated by lines, raw data by discrete points.

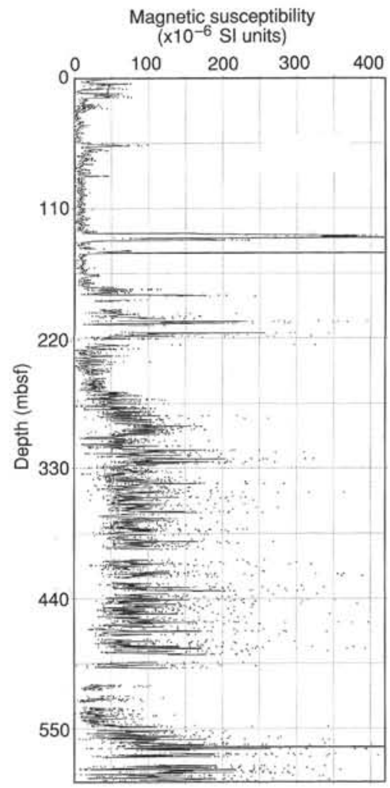

Figure 32. MST magnetic susceptibility, Hole 955A. Filtered data indicated by lines, raw data by discrete points.

is correctly accounted for. Because of increased lithification with depth, below 485 mbsf some velocities were determined with the Hamilton Frame. Compared to other sites at this depth, these velocities are low, suggesting the continued influence of gas expansion in the deep section.

Shear Strength

The motorized vane shear device and the handheld penetrometer were used together to measure the sediment strength, providing a means of comparison between the two instruments. Vane shear measurements were made from Core 3H at 20.00 mbsf, averaging one per section or every other section, through Core 36X at 331.19 mbsf. Penetrometer measurements were made beginning on Core 6H at 46.67 mbsf and continued until the sediment did not yield to the penetrometer probe. Below Core 36X at 331.19 mbsf the probe either chipped the core face or left a small impression. Data are presented in Table 11 and are plotted against depth downhole in Figure 39. Notice that the vane shear and penetrometer values correlate well throughout the entire interval in which both measurements were made. The data show a general trend of increasing strength downhole from about 0 kPa to 200 kPa at ~340 mbsf. While it was possible to make these measurements on the gas disrupted cores, the strength estimates were certainly influenced by the cracks and fractures introduced by gas expansion. While local strength variations estimated by the vane shear apparatus and the penetrometer compare well, the penetrometer values show a persistent deviation at 100 mbsf and increase to nearly 50 kPa at 330 mbsf.

Thermal Conductivity

Thermal conductivity measurements were conducted on alternate core sections beginning with Section 157-955A-1H-1 and continuing to Section 157-955A-13H-5 at ~120 mbsf, where measurements were discontinued because of increasing core disruption by gas expansion. These values are listed in Table 12 and plotted in Figure 40. Thermal conductivity shows a general increase, reflecting increasing consolidation, to ~110 mbsf. The dramatic decrease seen below this point is probably the result of increased core disruption, which would have substantially reduced conductive transport of heat.

DOWNHOLE MEASUREMENTS

Logging Operations

A full suite of three Schlumberger tool strings were run at Hole 955A. The quad combination, geochemical, and FMS tool strings provided comprehensive coverage of the entire open hole section. The WHC was used during logging to counter ship heave resulting from the mild sea-state conditions (0.3–1.25 m heave). The base of the drill pipe was initially set at 103 mbsf. A summary of the logging tool strings used on Leg 157, the basis of their measurement principles, and logging operations are discussed in the "Explanatory Notes." A summary of the logging operations at Hole 955A is given in Table 13.

A downgoing log was recorded at 1500 ft/hr from the end of the pipe to a total depth of 599 mbsf. Total penetration in Hole 955A was 599.4 mbsf and therefore no hole fill was encountered. A short upgoing log was recorded at 900 ft/hr from this depth to 456 mbsf, followed by the main log from 599 to 73 mbsf. The geochemical combination recorded data from 599 mbsf to the mud line (73–0 mbsf, through pipe) at 550 ft/hr. A second run at the same logging speed recorded data from 599 to 461 mbsf. The third run, FMS, comprising a natural gamma-ray tool in combination with an FMS, recorded three open-hole runs, the first from 599 to 390 mbsf at 1500 ft/hr, the sec-

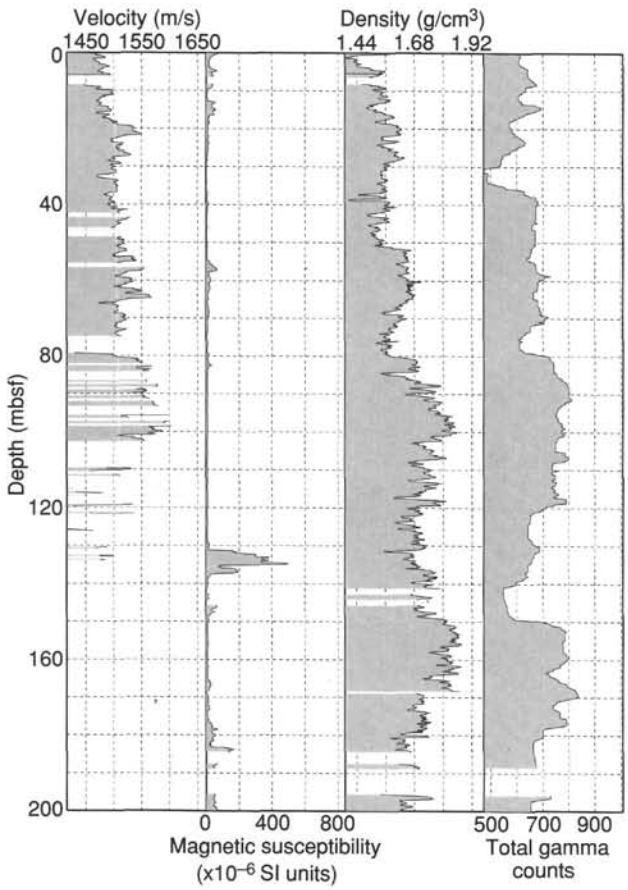

Figure 33. Filtered MST velocity, magnetic susceptibility, density, and natural gamma for 0–200 mbsf, Hole 955A.

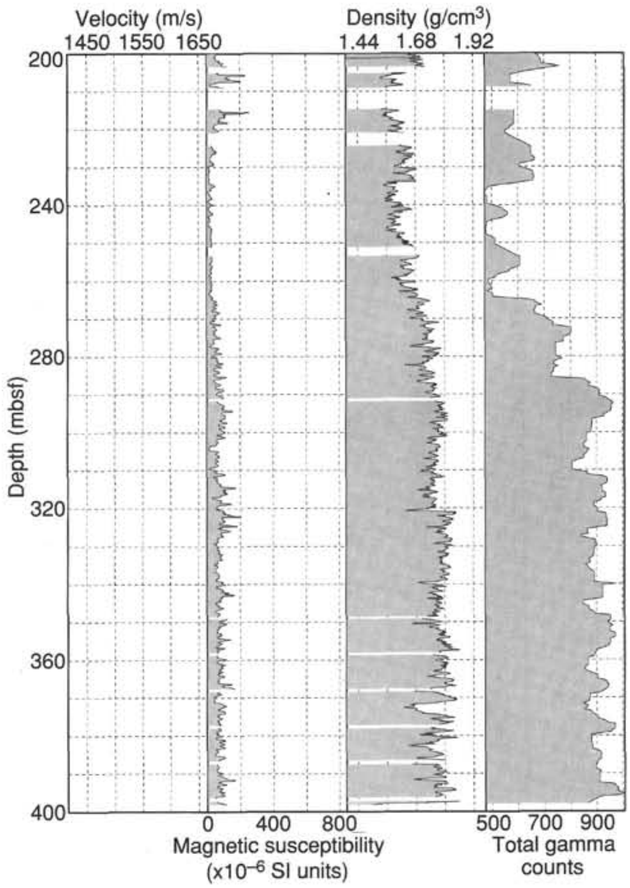

Figure 34. Filtered MST velocity, magnetic susceptibility, density, and natural gamma for 200–400 mbsf, Hole 955A.

ond from 599 to 91 mbsf at 1500 ft/hr, and the final run from 599 to 70 mbsf at 1800 ft/hr.

Log Quality

The main logs recorded at Hole 955A are shown in Figures 41, 42, and 43 and are generally of high quality. Above 73 mbsf, the sonic, induction, and density data are invalid, and the natural gamma-ray and other geochemical logs are highly attenuated by the presence of the drill pipe.

Hole 955A is very rugose in parts, shown by the hole caliper in Figure 42, and as a result the density log has suffered in quality. The white area in the center of the figure shows the diameter of a gauge hole drilled with the XCB coring bit, while the shaded areas show how much wider the hole is than originally drilled. In the comparison of log bulk density to discrete measurements on core (Fig. 44), the log bulk density appears to have intervals of poor quality data that correlate with zones of wider, rugose borehole. This occurs when pad contact with the borehole wall is incomplete, resulting in a small amount of borehole fluid being included with the measurement of sediment density.

For the most part, the velocity data from the logs are of very good quality. A minor amount of cycle skipping and other noise is present in the raw log data, but shipboard processing of the traveltimes eliminated most of these excursions. The sonic velocity presented in Figure 42 is the processed data and has been spliced with the MST data above 74 mbsf.

Hole width also affects the natural gamma-ray activity log by raising the count rate where the hole is narrow and lowering it where it is wide. Post-cruise processing will correct for these environmental factors.

Data from the geochemical logging tool require extensive post-cruise processing to convert the relative elemental yields into weight percentages of elements and oxides. The preliminary elemental yield data can be used to determine relative elemental variations (Fig. 43).

Results

Variation of Logs with Depth

The open-hole interval logged in Hole 955A (~73–599 mbsf) covers lithologic Units I to V (Quaternary to middle Miocene) (see "Lithostratigraphy," this chapter). The sequence is dominated by hemipelagic fine grained sediments, interbedded with volcaniclastic material in the lower part. The drilled sequence is subdivided into log units since the lithostratigraphy at this site was principally defined on subtle variations in sand content and type of volcaniclastic material, rather than bulk formation properties measured by the logs.

Log Unit I (73–265 mbsf) is characterized by high and variable log-carbonate values with a corresponding lower and variable total gamma ray (Figs. 41 and 43). It encompasses lithologic Units I and II and is composed predominantly of a nannofossil mixed sediment with foraminifers. Within this interval there are nonvolcanic sand beds, particularly in Subunit Ib, which is characterized by the washed out nature of the hole over the interval ~165–210. Log Unit I shows distinct changes in sediment composition as seen from the carbonate index log in Figure 43. Carbonate values are high down to ~148 mbsf and then an interval of lower carbonate from 148 to 210 mbsf. From 210 to 265 mbsf the carbonate content is greater and shows a sharp decrease at 265 mbsf at the boundary with log Unit II below (coinci-

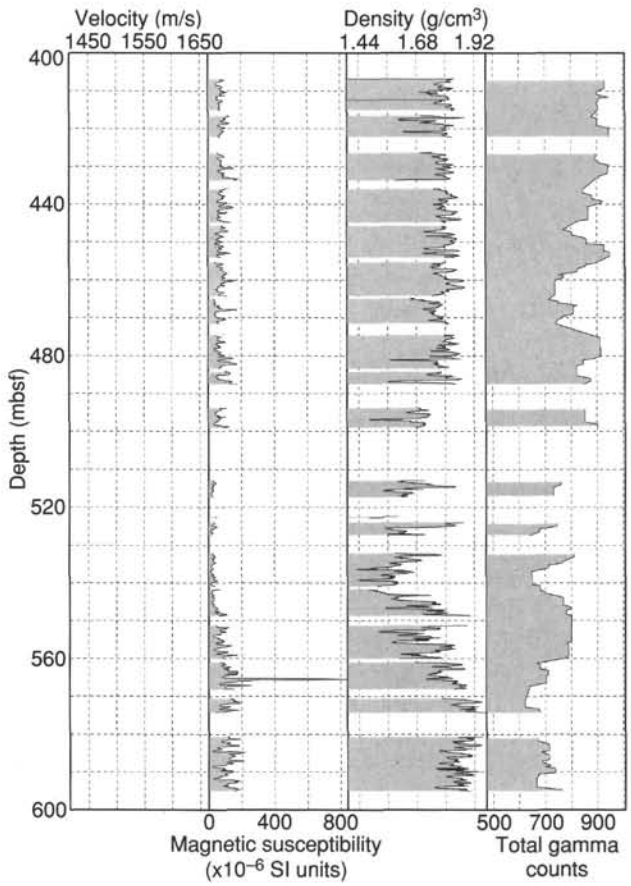

Figure 35. Filtered MST velocity, magnetic susceptibility, density and natural gamma for 400 mbsf to total depth, Hole 955A.

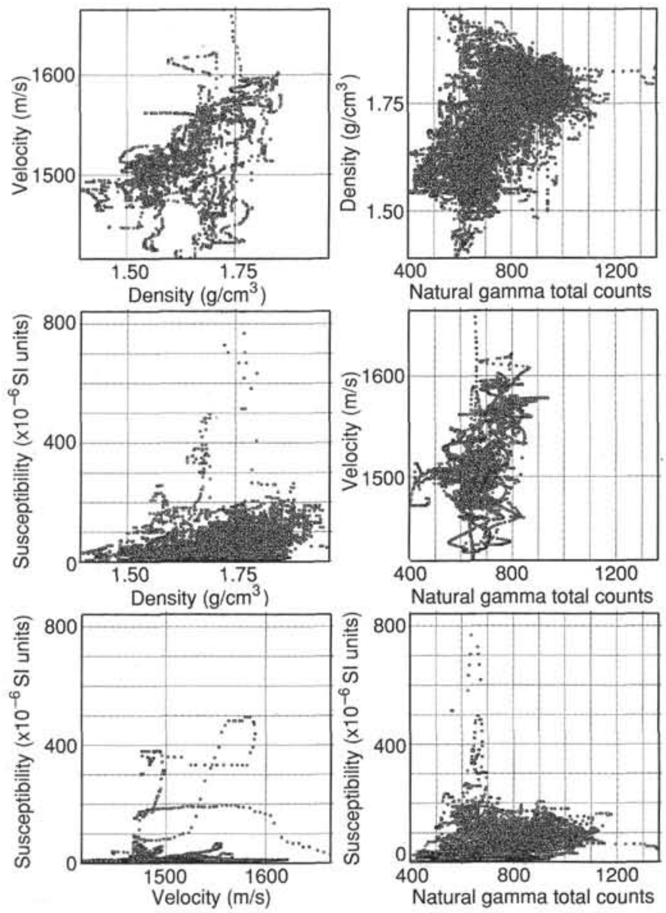

Figure 36. Crossplots of MST estimated rock properties, Hole 955A.

dent with the Miocene/Pliocene boundary, "Biostratigraphy" section, this chapter). These changes are reflected in the resistivity and sonic velocity logs (Fig. 42) with a notable increase in velocity at 210 mbsf on transition into the carbonate-rich zone. The variation in carbonate values in log Unit I are in general agreement with the carbonate variations from core analysis, although the resolution of the core data is poorer and the sampling is predominantly from pelagic intervals and therefore not necessarily representative of the bulk formation geochemistry, as measured by the GST.

Log Unit II (265–465 mbsf) appears as a homogeneous zone in the logs. The total gamma ray is higher (Fig. 41) than in the unit above, reflecting the higher clay and lower carbonate component (Fig. 43). The sonic log shows a normal compaction trend, increasing linearly with depth. The FMS dipmeter logs show a subtle change in strike and dip of beds around 370 mbsf, correlating with a hiatus identified from paleontological data. A slight change in character is notable in the resistivity (Fig. 42) log at this depth.

Log Unit III (465–565 mbsf) shows an increase in the mean of the gamma-ray log together with an increase in its variability, representing an increase in the felsic volcaniclastic components in the sediments. This encompasses the lower parts of lithostratigraphic Subunits IVa and IVb, which contain volcaniclastics of evolved composition, correlated to the lower Fataga and Mogan phases of volcanism on Gran Canaria. The resistivity is lower and more variable in log Unit III, correlating with a higher percentage of volcanic sands observed in the cores, resulting in higher porosities. The presence of discrete ash layers is well imaged by the FMS (Fig. 45) and should augment core-based studies of ash distribution.

Log Unit IV (564–599 mbsf) is characterized by a sharp decrease in the Th and U logs and an increase in the carbonate log (Figs. 41 and 43) correlating with the abrupt disappearance of felsic material noted in the cores. This corresponds to lithostratigraphic Unit V and represents the end of the Gran Canaria basaltic shield phase of volcanism. Bulk density, resistivity, and sonic velocity also increase, representing the compositional change to the more dense mafic material.

Evidence for Slump Blocks

Much slumping was evident in the cores in lithostratigraphic Units I and II and there is evidence from seismic records (see Fig. 2) of large slump blocks coming into this area from the African margin to the east. The subdivisions in log Unit I (~148, 210, 265 mbsf), primarily based on carbonate variation, are coincident with hiatus or zone boundaries in paleontological data (see "Biostratigraphy," this chapter). At ~150 mbsf an age inversion in both nannofossil and foraminifer zones indicates older material lying on younger sediments. This obvious evidence for slump blocks is supported by the changes in the logs. Preliminary analysis of FMS dipmeter data indicates a high degree of slumping is present in the upper portion of the hole with generally higher dips observed in the interval above ~210 mbsf. From the combined evidence of the logs and paleontological data it appears that the interval ~100–150 mbsf and possibly 150–210 mbsf are contiguous slump blocks. Planned post-cruise analysis of FMS data will address these preliminary observations in more detail.

Temperature

The Lamont-Doherty temperature tool was deployed on the quad combination tool string in Hole 955A. An accurate thermal gradient cannot be obtained from this measurement; cold seawater is circulat-

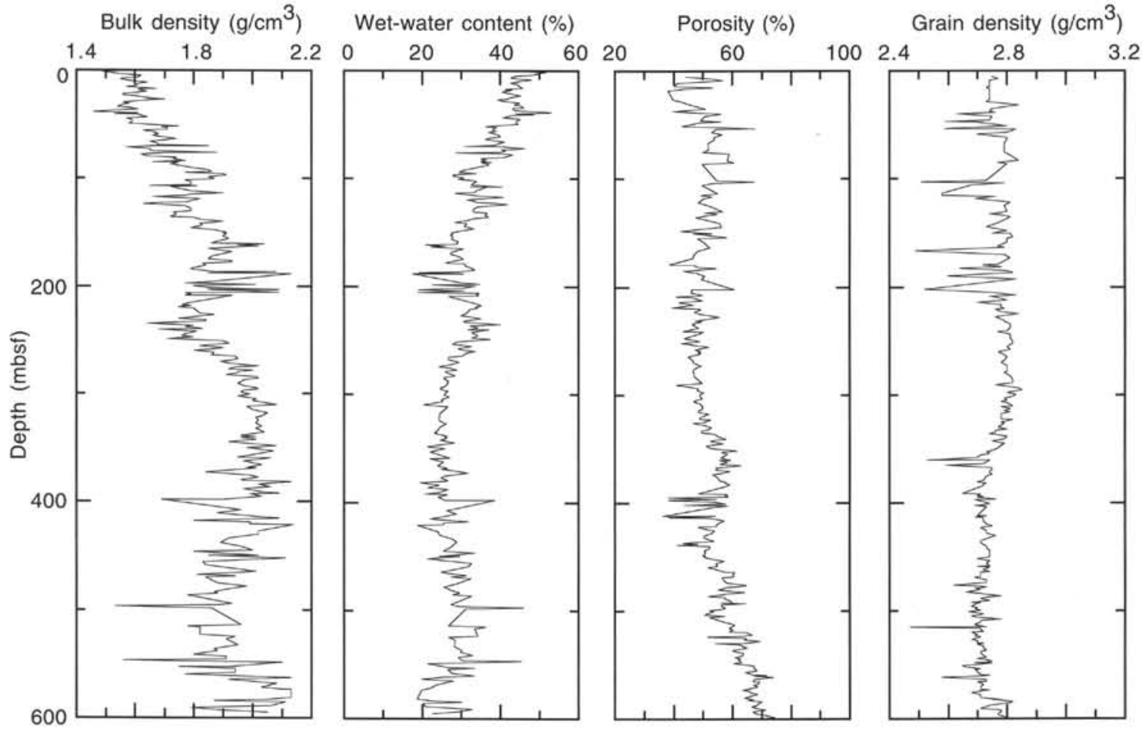

Figure 37. Bulk density (Method B); wet-water content, porosity, and grain density (Method C). Hole 955A.

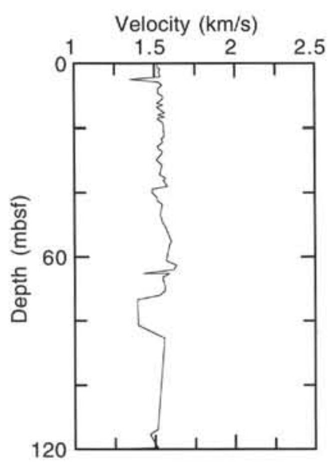

Figure 38. *P*-wave velocity, Hole 955A.

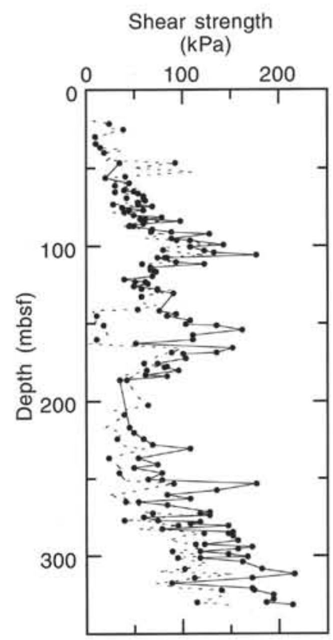

Figure 39. Strength data determined by vane shear (dashed line) and hand-held penetrometer (solid line) methods, Hole 955A.

ed in the hole during drilling, which cools the adjacent formation. A minimum of three bottom-hole temperature measurements over a period of time are required to extrapolate the virgin bottom-hole temperature and hence calculate the true thermal gradient. Nevertheless, a temperature of 12.5°C was obtained at 599 mbsf and with a mud-line temperature of 3.1°C the thermal gradient must be greater than 15.7°C/km.

Porosity Estimates

Porosity has been calculated from resistivity and sonic velocity logs and is compared to porosity measurements on discrete core samples (Figs. 46, 47, and 48). The methods of determining resistivity-porosity using Archie's (1942) equation and sonic-porosity using the time average equation are described in detail on the logging data from Site 953 (this volume).

The fit of the resistivity-porosity (Fig. 46), using the calculated constants of a = 1.6 and m = 1.4, is very good for the upper portion of the hole compared to core porosity but breaks down below 400 mbsf. The calculated sonic-porosity (Fig. 47) shows a reasonable correlation in the upper portion of the hole but again is poorer in the lower section. These discrepancies are related to the higher percentage of volcanic sands found in the lower portion of the hole.

Table 9. Index properties, Hole 955A.

Core, section, interval (cm)	Depth (mbsf)	WCw (%)	WCd (%)	BDb (g/cm³)	BDc (g/cm³)	GDb (g/cm³)	GDc (g/cm³)	DDb (g/cm³)	DDc (g/cm³)	Porb (%)	Porc (%)	VRb	VRc
157-955A-													
1H-1, 7–9	0.07	43.28	76.30	1.61	1.60	2.85	2.80	0.91	0.91	68.01	67.58	2.13	2.08
1H-2, 6–8	1.56	51.58	106.55	1.49	1.48	2.87	2.80	0.72	0.72	74.88	74.43	2.98	2.91
1H-3, 102–104	4.02	47.56	90.71	1.55	1.53	2.87	2.77	0.81	0.80	71.76	71.01	2.54	2.45
1H-4, 30–32	4.80	43.91	78.30	1.62	1.59	2.95	2.77	0.91	0.89	69.24	67.95	2.25	2.12
1H-5, 73–75	6.73	42.75	74.66	1.61	1.60	2.83	2.78	0.92	0.92	67.37	66.97	2.06	2.03
1H-6, 29–31	7.79	45.16	82.33	1.56	1.57	2.75	2.78	0.86	0.86	68.82	69.10	2.21	2.24
2H-1, 62–64	8.72	47.86	91.78	1.55	1.53	2.91	2.77	0.81	0.80	72.30	71.29	2.61	2.48
2H-2, 22–24	9.82	45.41	83.18	1.57	1.55	2.83	2.71	0.86	0.85	69.70	68.74	2.30	2.20
2H-3, 42–44	11.52	42.54	74.05	1.64	1.60	2.93	2.73	0.94	0.92	67.95	66.41	2.12	1.98
2H-4, 5–7	12.65	44.25	79.38	1.61	1.57	2.97	2.74	0.90	0.88	69.71	68.01	2.30	2.13
2H-5, 82–84	14.92	44.96	81.67	1.60	1.58	2.94	2.81	0.88	0.87	70.10	69.13	2.34	2.24
2H-6, 34–36	15.94	45.76	84.37	1.57	1.56	2.83	2.82	0.85	0.85	69.97	69.90	2.33	2.32
2H-7, 35–37	17.45	41.20	70.05	1.67	1.63	2.97	2.78	0.98	0.96	67.00	65.50	2.03	1.90
2H-CC, 9–11	17.77	42.05	72.57	1.63	1.61	2.84	2.75	0.94	0.93	66.80	66.06	2.01	1.95
3H-1, 50–52	18.10	42.94	75.25	1.61	1.60	2.80	2.78	0.92	0.91	67.27	67.14	2.06	2.04
3H-2, 88–90	19.98	40.39	67.77	1.64	1.63	2.77	2.71	0.98	0.97	64.66	64.15	1.83	1.79
3H-3, 136–138	21.96	43.70	77.62	1.56	1.58	2.62	2.71	0.88	0.89	66.49	67.27	1.98	2.06
3H-4, 111–113	23.21	45.18	82.43	1.56	1.55	2.75	2.70	0.86	0.85	68.90	68.51	2.22	2.18
3H-5, 67–69	24.27	42.92	75.21	1.60	1.58	2.79	2.68	0.92	0.90	67.18	66.30	2.05	1.97
3H-6, 87–89	25.97	41.57	71.15	1.64	1.61	2.84	2.72	0.96	0.94	66.37	65.35	1.97	1.89

Notes: WCw = water content (% wet sample weight), WCd = water content (% dry sample weight), BD = bulk density, GD = grain density, DD = dry density, Por = porosity, and VR = void ratio. Suffixes "b" and "c" on column heads indicate value calculated using Method B and Method C, respectively (see "Explanatory Notes," this volume).

Only a part of this table is reproduced here. The entire table appears on the CD-ROM (back pocket).

In an attempt to improve the fit of the resistivity-porosity the parameters of a and m in Archie's equation were recalculated from the cross plot of ln R_t/R_w and in (see "Site 953," this volume) for different zones downhole. The results are shown in Figure 48 and exhibit a marked improvement, giving an excellent fit overall with the core data.

SEDIMENT ACCUMULATION RATES

A sediment accumulation curve has been constructed for Site 955 (Fig. 49) based on 35 nannofossil and 17 planktonic foraminiferal age determinations, giving a total of 52 points (Table 14). All nannofossil and most foraminifer datum levels were identified in hemipelagic layers or in burrow infills of hemipelagic sediment. Sediment accumulation rates are reasonably well constrained by microfossil datum levels in the interval below 245 mbsf.

The sediment accumulation rate is ~67 m/m.y. from the surface to 102 mbsf (0–1.6 Ma) in the upper part of lithologic Subunit Ia. Sediments in this interval are visibly affected by slumping (see "Lithostratigraphy," this chapter), but the coherent nature of the accumulation curve in this interval suggests that the slumped units have retained their stratigraphic integrity. At ~102 mbsf there is an apparent hiatus, spanning a minimum of 0.77 m.y. between 1.6 and 2.37 Ma.

Several seemingly discrete packages of sediment were identified from 102 mbsf to ~240 mbsf. All the sediment within each of these packages belongs to the same zone or to consecutive zones within the limits of zonal resolution. Some and possibly all of these packages may represent slumped blocks of sediment. Some zones are missing between these packages, and younger zones are present beneath older ones. Again the core is visibly affected by slumping in this interval.

The age limits of these packages are poorly constrained, as many of the datums used are, of necessity, species absences. Also highest occurrences of species that occur at the top of a package may not be the true last appearance datum, but may reflect slump related truncation. The situation is similar for lowest occurrences. Accordingly, no meaningful accumulation rates can be calculated within these packages.

The highest package, from ~103 to ~120 mbsf, has a minimum age of 2.37 Ma and a maximum age of 2.44 Ma. The underlying package is from ~120 to ~130 mbsf and has with a minimum age of 2.76 Ma and a maximum age of 4.01 Ma. The next underlying package is from ~130 to ~145 mbsf, and it has a minimum age of 4.63 Ma and a maximum age of 5.56 Ma.

The section from 120 to 130 mbsf is apparently repeated from 145 to ~205 mbsf, with a minimum age of 2.76 Ma and a maximum age of 4.01 Ma. The underlying package is from ~205 to ~240 mbsf, with a minimum age of 3.77 Ma and a maximum age of 4.39 Ma. A straight line on the accumulation rate diagram (Fig. 49) can be drawn through the lower two packages, indicating that perhaps the apparent discontinuities between them are related to sampling intervals. Shore-based examination may resolve this issue. No further slumping is evident below 240 mbsf.

The sediment accumulation rate is ~18 m/m.y., from 240 to ~285 mbsf (4.63–6.8 Ma) in lithologic Unit II, which seems to reflect the later part of the hiatus in volcanic activity on Gran Canaria. In the lowermost part of Unit II and Unit III, from 285 to ~370 mbsf (6.8–8.8 Ma), the accumulation rate is ~42 m/m.y., which probably reflects the earlier part of the volcanic hiatus on Gran Canaria. A hiatus appears to be present at ~370 mbsf, spanning ~0.6 m.y. between 8.8 and 9.4 Ma. A hiatus occurs in the same interval at Site 954, suggesting the possibility of a regional event.

The sediment accumulation rate is ~60 m/m.y. from 370 to ~445 mbsf (9.4–10.8 Ma) in lithologic Subunit IVa. This high rate is probably related to the input of turbidites from the African margin and the later part of the Fataga phase of volcanism on Gran Canaria. The accumulation rate based on microfossils is ~31 m/m.y., from 445 mbsf in the lower part of lithologic Subunit IVa, and Subunit IVb, to the lowest microfossil datum at 595 mbsf in Unit V (10.8 to 14.5–15.8 Ma, see below). Correlation of distinctive volcaniclastic layers to Gran Canaria, where they are well dated, suggests somewhat younger ages for Subunit IVb (517–567 mbsf). The microfossil age at 595 mbsf is 15.8 Ma, whereas if you extrapolate the age from the volcaniclastic layers at 540–567 mbsf the age is ~14.5 Ma. The younger ages suggested by the volcaniclastic layers give an accumulation rate of ~50m/m.y. However, there is a major contrast in lithology between Subunit IVb, which is rich in volcaniclastic layers, and Unit V, which is dominantly hemipelagic, so the higher accumulation rates end at 567 mbsf, with the basal cores returning to low background accumulation rates.

IN-SITU TEMPERATURE MEASUREMENTS

Four ADARA temperature measurements were made while coring Hole 955A. The measurements were taken during Cores 3H (27.1 mbsf), 6H (55.6 mbsf), 9H (84.1 mbsf), and 12H (112.6 mbsf). Sub-

Table 10. Compressional-wave velocities, Hole 955A.

Core, section, interval (cm)	Depth (mbsf)	Velocity (km/s)	Tool	Temperature (°C)
157-955A-				
1H-1, 24–26	0.24	1.52	DSV	
1H-1, 110–112	1.10	1.52	DSV	
1H-2, 29–31	1.79	1.54	DSV	18.8
1H-2, 109–111	2.59	1.53	DSV	18.7
1H-3, 28–30	3.28	1.53	DSV	19.0
1H-3, 105–107	4.05	1.53	DSV	19.3
1H-4, 33–35	4.83	1.35	DSV	19.5
1H-4, 122–124	5.72	1.52	DSV	19.0
1H-5, 76–78	6.76	1.55	DSV	19.5
1H-6, 32–34	7.82	1.52	DSV	19.5
2H-1, 46–48	8.56	1.52	DSV	20.5
2H-1, 124–126	9.34	1.52	DSV	20.1
2H-2, 52–54	10.12	1.55	DSV	20.8
2H-2, 139–141	10.99	1.55	DSV	19.5
2H-3, 52–54	11.62	1.54	DSV	21.0
2H-3, 132–134	12.42	1.52	DSV	19.7
2H-4, 35–37	12.95	1.55	DSV	20.7
2H-4, 103–105	13.63	1.52	DSV	20.0
2H-5, 20–22	14.30	1.54	DSV	20.1
2H-5, 119–121	15.29	1.56	DSV	19.8

Note: Temperature = temperature of the sample. Tools are DSV or Hamilton Frame.

Only a part of this table is reproduced here. The entire table appears on the CD-ROM (back pocket).

Table 11. Strength measurements, Hole 955A.

Core, section, interval (cm)	Depth (mbsf)	Pk str (kPa)	Res (kPa)	Pen (kPa)
157-955A-				
3H-2, 90–91	20.00	7	2	
3H-3, 140–141	22.00	24	12	
3H-4, 114–115	23.24	21	6	
3H-5, 72–73	24.32	24		
3H-6, 32–33	25.42	39	6	
4H-1, 72–73	27.82	20	6	
3H-7, 133–134	27.93	21	7	
4H-2, 121–122	29.81	9	4	
4H-3, 132–133	31.42	12	4	
4H-4, 54–55	32.14	15	8	
4H-5, 120–121	34.30	10	4	
4H-6, 82–83	35.42	11	4	
4H-7, 8–9	36.18	11	4	
5H-1, 21–22	36.81	14	5	
5H-1, 117–118	37.77	32	15	
5H-2, 57–58	38.67	38	7	
5H-3, 23–24	39.83	18	9	
5H-5, 81–82	43.41	24	8	
5H-6, 77–78	44.87	21	8	
6H-1, 57–58	46.67			34

Notes: Pk str = peak strength, undrained shear strength as measured by the vane shear, Res = residual shear strength, and Pen = unconfined shear strength as measured by the penetrometer, converted to kPa.

Only a part of this table is reproduced here. The entire table appears on the CD-ROM (back pocket).

bottom equilibrium temperatures were extrapolated from synthetic curves that were constructed to fit transient temperature data. It was not possible to calculate an equilibrium temperature for Core 3H because of frictional heating of the probe during the temperature station. This was most likely caused by the probe going too deeply into the sediments or movement of the probe during measurements. An equilibrium temperature for Core 6H was calculated to be 6.157°C but this number was considered unreliable because the probe also began to heat up (for perhaps the same reasons as for Core 3H). Therefore, only a few minutes of data were collected (Fig. 50). Cores 9H (Fig. 51) and 12H (Fig. 52) gave more reliable equilibrium temperatures of 6.378°C and 7.708°C, respectively. The mud line temperature was calculated at 3.154°C for the site.

Table 12. Thermal conductivity measurements, Hole 955A.

Core, section, interval (cm)	Depth (mbsf)	Method	TCcorr (W/mK)	Standard error (W/mK)	Drift (°/min)
157-955A-					
1H-1, 50	0.50	F	0.902	0.011	–0.012
1H-3, 50	3.50	F	1.019	0.012	–0.022
1H-5, 50	6.50	F	1.081	0.0126	–0.017
2H-1, 50	8.60	F	1.250	0.0138	0.036
2H-3, 50	11.60	F	0.981	0.0107	0.025
2H-5, 50	14.60	F	1.298	0.0118	0.028
3H-1, 50	18.10	F	0.976	0.0139	–0.008
3H-3, 50	21.10	F	1.203	0.00895	0.006
3H-5, 50	24.10	F	1.082	0.0136	0.027
4H-1, 50	27.60	F	1.009	0.013	–0.034
4H-3, 50	30.60	F	1.088	0.0105	–0.009
4H-5, 50	33.60	F	1.074	0.00854	–0.002
5H-1, 50	37.10	F	0.950	0.0154	0.023
5H-3, 50	40.10	F	1.062	0.0175	–0.008
5H-5, 50	43.10	F	1.108	0.0148	0.020
6H-1, 50	46.60	F	0.975	0.0118	0.001
6H-3, 50	49.60	F	1.065	0.00908	–0.012
6H-5, 50	52.60	F	1.103	0.0112	–0.005
7H-1, 50	56.10	F	1.225	0.0102	0.037
7H-3, 50	59.10	F	1.189	0.0147	0.011
7H-5, 50	62.10	F	0.995	0.0145	–0.012
8H-1, 50	65.60	F	1.138	0.0134	0.009
8H-3, 50	68.60	F	0.981	0.0107	0.037
8H-5, 50	71.60	F	1.170	0.0142	0.018
9H-1, 50	75.10	F	1.029	0.0103	–0.004
9H-3, 50	78.10	F	1.011	0.0124	–0.032
9H-5, 50	81.10	F	1.106	0.0130	–0.018
10H-1, 50	84.60	F	1.087	0.0140	0.009
10H-3, 50	87.60	F	1.326	0.0167	–0.006
10H-5, 50	90.60	F	1.22	0.0129	0.03
11H-1, 50	94.10	F	1.12	0.0146	0.023
11H-3, 50	97.10	F	1.238	0.00822	–0.009
11H-5, 50	100.10	F	1.416	0.0163	0.001
12H-1, 50	103.60	F	1.353	0.0138	0.053
12H-3, 50	106.60	F	1.316	0.0083	–0.025
12H-5, 50	109.60	F	0.952	0.0115	–0.004
13H-1, 50	113.10	F	1.033	0.0162	–0.024
13H-3, 50	116.10	F	0.941	0.0143	–0.010
13H-5, 50	119.10	F	1.394	0.0106	0.012

Notes: Method used either F = full-space or H = half-space. TCcorr = thermal conductivity corrected for drift.

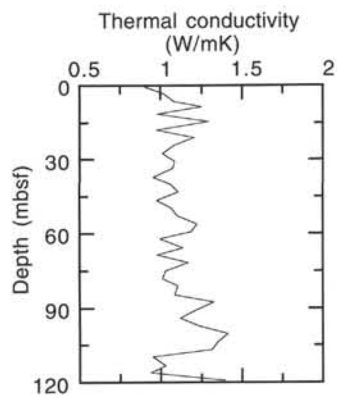

Figure 40. Thermal conductivity, Hole 955A.

A geothermal gradient can be calculated from temperature measurements downhole that can provide an estimate of heat flow when used with an estimate of thermal conductivity. Plotting the sub-bottom equilibrium temperatures along with the mud-line temperature against depth, the geothermal gradient was approximated at 39.99°C/km by using a linear mean (Fig. 53). Core 3H was not used in calculating the geothermal gradient because no equilibrium temperature data were available, nor was Core 6H used because of the unreliability of the measurements. Heat flow was calculated by multiplying the geothermal gradient by the average thermal conductivity for the hole (see "Physical Properties," this chapter). Thermal conductivity downhole had an average value of approximately 1.15 W/(m·K), resulting in a heat flow value of 45.99 mW/m^2.

REFERENCES

Archie, G.E., 1942. The electrical resistivity log as an aid in determining some reservoir characteristics. *Trans. Am. Inst. Min. Metall. Pet. Eng.,* 146:54–62.

Bogaard, P., Schmincke, H.-U., Freundt, A., Hall, C., and York, D., 1988. Eruption ages and magma supply rates during the Miocene evolution of Gran Canaria: single crystal $^{40}Ar/^{39}Ar$ laser ages. *Naturwissenschaften,* 75:616–617.

Cremer, M., Orsolini, P., and Ravenne, C., 1985. Cap-Ferret Fan, Atlantic Ocean. *In* Bouma, A.H., Normark, W.R., and Barnes, N.E. (Eds.), *Submarine Fans and Related Turbidite Systems:* New York (Springer), 113–119.

Freundt, A., and Schmincke, H.-U., 1995. Eruption and emplacement of a basaltic welded ignimibrite during caldera formation on Gran Canaria. *Bull. Volcanol.,* 56:640–659.

Gieskes, J.M., 1981. Deep-sea drilling interstitial water studies: implications for chemical alteration of the oceanic crust, layers I and II. *In* Warme, J.E., Douglas, R.G., and Winterer, E.L. (Eds.), *The Deep Sea Drilling Project: A Decade of Progress.* Spec. Publ.—Soc. Econ. Paleontol. Mineral., 32:149–167.

Gieskes, J.M., Graham, D., and Ellis, R. 1980. Interstitial-water studies, Deep Sea Drilling Project Sites 415 and 416. *In* Lancelot, Y., Winterer, E.L., et al., *Init. Repts. DSDP,* 50: Washington (U.S. Govt. Printing Office), 691–693.

Haq, B.U., Hardenbol, J., and Vail, P.R., 1987. Chronology of fluctuating sea levels since the Triassic. *Science,* 235:1156–1167.

Hoernle, K., and Schmincke, H.-U., 1993. The petrology of the tholeiites through melilite nephelinites on Gran Canaria, Canary Islands: crystal fractionation, accumulation, and depth of melting. *J. Petrol.,* 34:573–578.

Rio, D., Fornaciari, E., and Raffi, I., 1990. Late Oligocene through early Pleistocene calcareous nannofossils from western equatorial Indian Ocean (Leg 115). *In* Duncan, R.A., Backman, J., Peterson, L.C., et al., *Proc. ODP, Sci. Results,* 115: College Station, TX (Ocean Drilling Program), 175–235.

Schmincke, H.U., 1976. Geology of the Canary Islands. *In* Kunkel, G. (Ed.), *Biogeography and Ecology in the Canary Islands:* The Hague (W. Junk), 67–184.

————, 1994. *Geological Field Guide: Gran Canaria* (7th ed.): Kiel, Germany (Pluto Press).

Schmincke, H.-U., and von Rad, U., 1979. Neogene evolution of Canary Island volcanism inferred from ash layers and volcaniclastic sandstones of DSDP Site 397 (Leg 47A). *In* von Rad, U., Ryan, W.B.F., et al., *Init. Repts. DSDP,* 47 (Pt. 1): Washington (U.S. Govt. Printing Office), 703–725.

Thierstein, H.R., Geitzenauer, K., Molfino, B., and Shackleton, N.J., 1977. Global synchroneity of late Quaternary coccolith datum levels: validation by oxygen isotopes. *Geology,* 5:400–404.

Weaver, P.P.E., 1983. An integrated stratigraphy of the upper Quaternary of the King's Trough Flank area, N.E. Atlantic. *Oceanol. Acta,* 6:451–456.

Young, J.R., 1990. Size variation of Neogene *Reticulofenestra* coccoliths from Indian Ocean DSDP cores. *J. Micropaleontol.,* 9:71–85.

Young, J.R., Flores, J.-A., and Wei, W., 1994. A summary chart of Neogene nannofossil magnetobiostratigraphy. *J. Nannoplankton Res.,* 16:21–27.

Ms 157IR-109

NOTE: For all sites drilled, core-description forms ("barrel sheets") and core photographs can be found in Section 6, beginning on page 561. Smear-slide and thin-section data are given in Section 7, beginning on page 835. The CD-ROM (back pocket, this volume) contains physical properties and geochemical data, MST data, logging data, and color core photographs (Sites 950 and 953 only).

Table 13. Summary of logging operations, Hole 955A.

Date (September 1994)	Time (UTC)	Activity
12	15:40	Last core on deck. Prepare hole for logging. Hole displaced with sepolite mud for logging operations.
13	00:00	Hole preparation complete, rig up wireline.
	01:45	RIH with NGT-LSS-CNT-HLDT-DIT (+TLT).
	02:50	Start downgoing log from EOP to TD (599 mbsf).
	04:06	Upgoing log at 900 ft/hr from 599 to 456 mbsf. RIH to TD.
	04:45	Main upgoing log at 900 ft/hr from 599 mbsf to EOP (pulled to 73 mbsf). HLDT caliper off at 103 mbsf. POOH.
	09:20	RIH with NGT-ACT-GST (+TLT).
	10:45	Main upgoing log from 599 mbsf to mudline at 550 ft/hr. RIH to TD.
	14:26	Repeat uplog from TD to 461 mbsf at 550 m/hour. POOH.
	16:50	RIH with NGT-FMS.
	18:08	Upgoing log from TD to 390 mbsf at 1500 ft/hr. RIH to TD.
	18:51	Main upgoing log from TD to 91 mbsf. RIH to TD.
	20:14	Repeat upgoing log from TD to 70 mbsf. POOH.
	22:20	Tool out of Hole. Rig down.
	23:15	End of logging operations.

Note: Drillers TD = 599.4 mbsf. WD = 2865.4 mbrf. EOP = 102.5 mbsf.

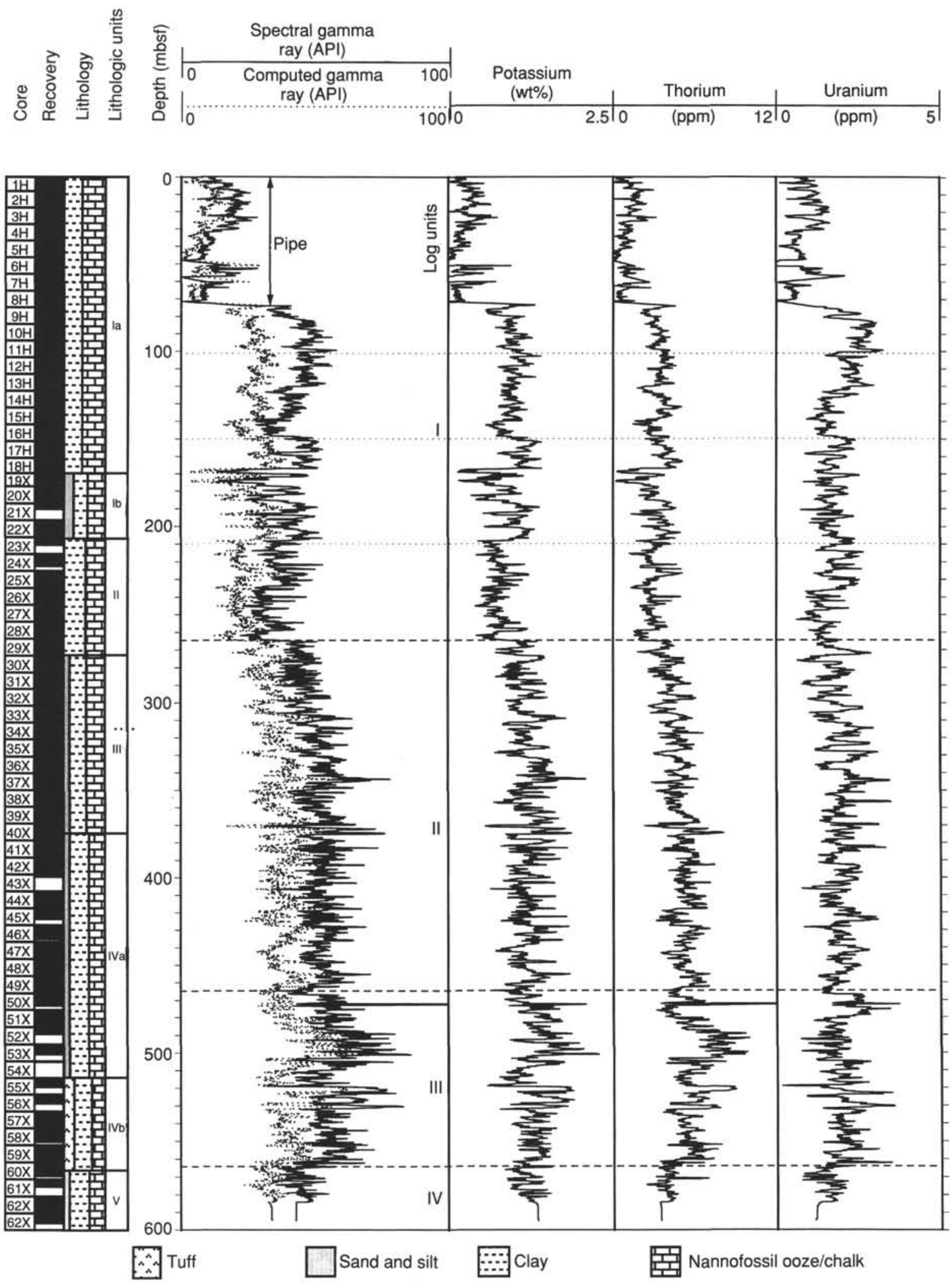

Figure 41. Hole 955A natural gamma-ray data from the NGT recorded on the geochemical gamma-ray tool string. The left track shows the total and the computed gamma-ray counts; tracks for K, Th, and U components of the total gamma-ray signal follow.

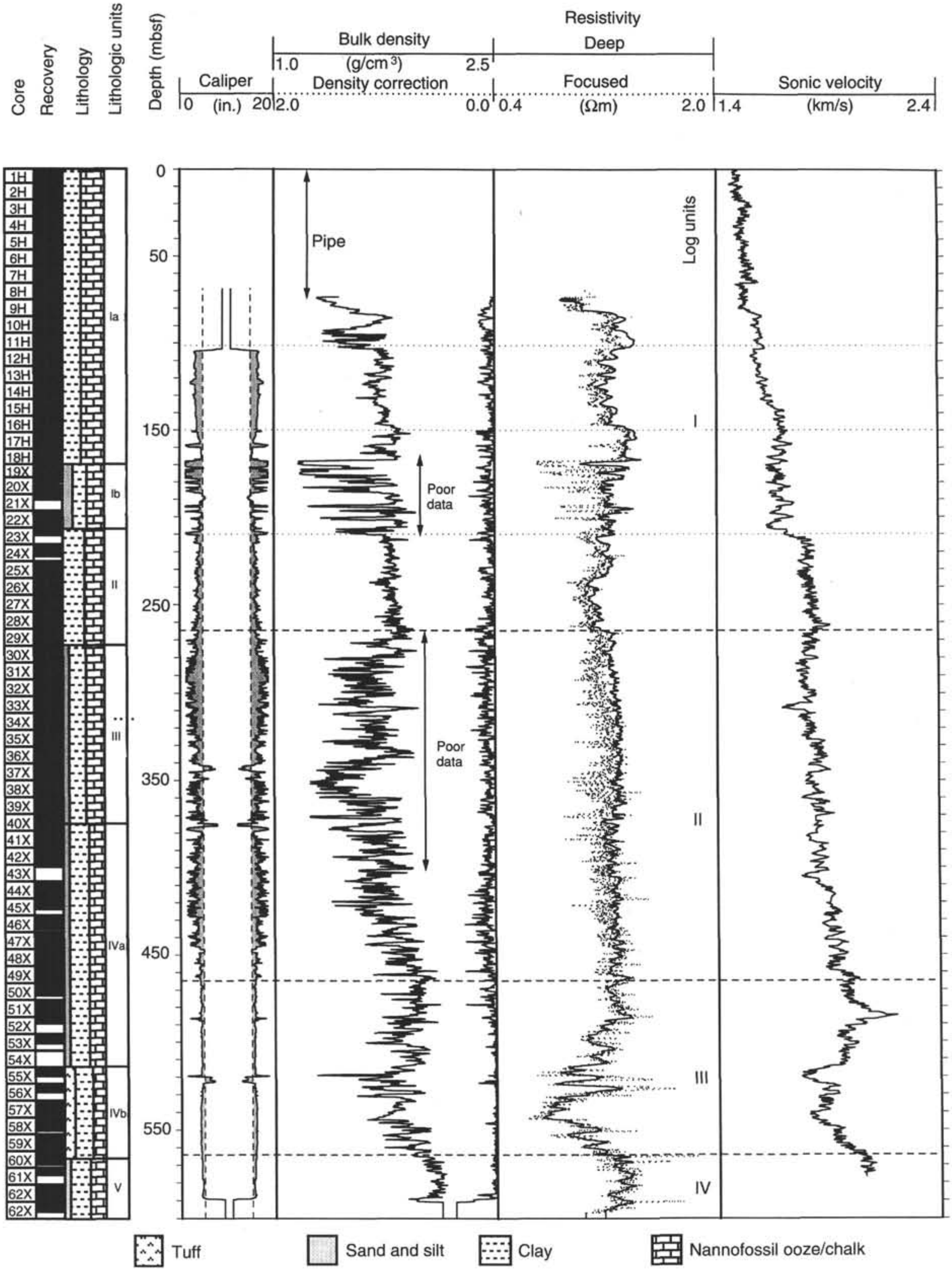

Figure 42. Hole 955A physical logs summary. Caliper data from the HLDT shown with bulk-density data from the HLDT, deep phasor induction and spherically focused resistivity from the phasor DIT, and sonic velocity data from the LSS. The central white area in the caliper log represents the XCB bit size (10 1/8 in.); shading represents the "washed out" portion of the hole from the bit size to actual measured diameter. The sonic velocity data have been processed to remove cycle skips.

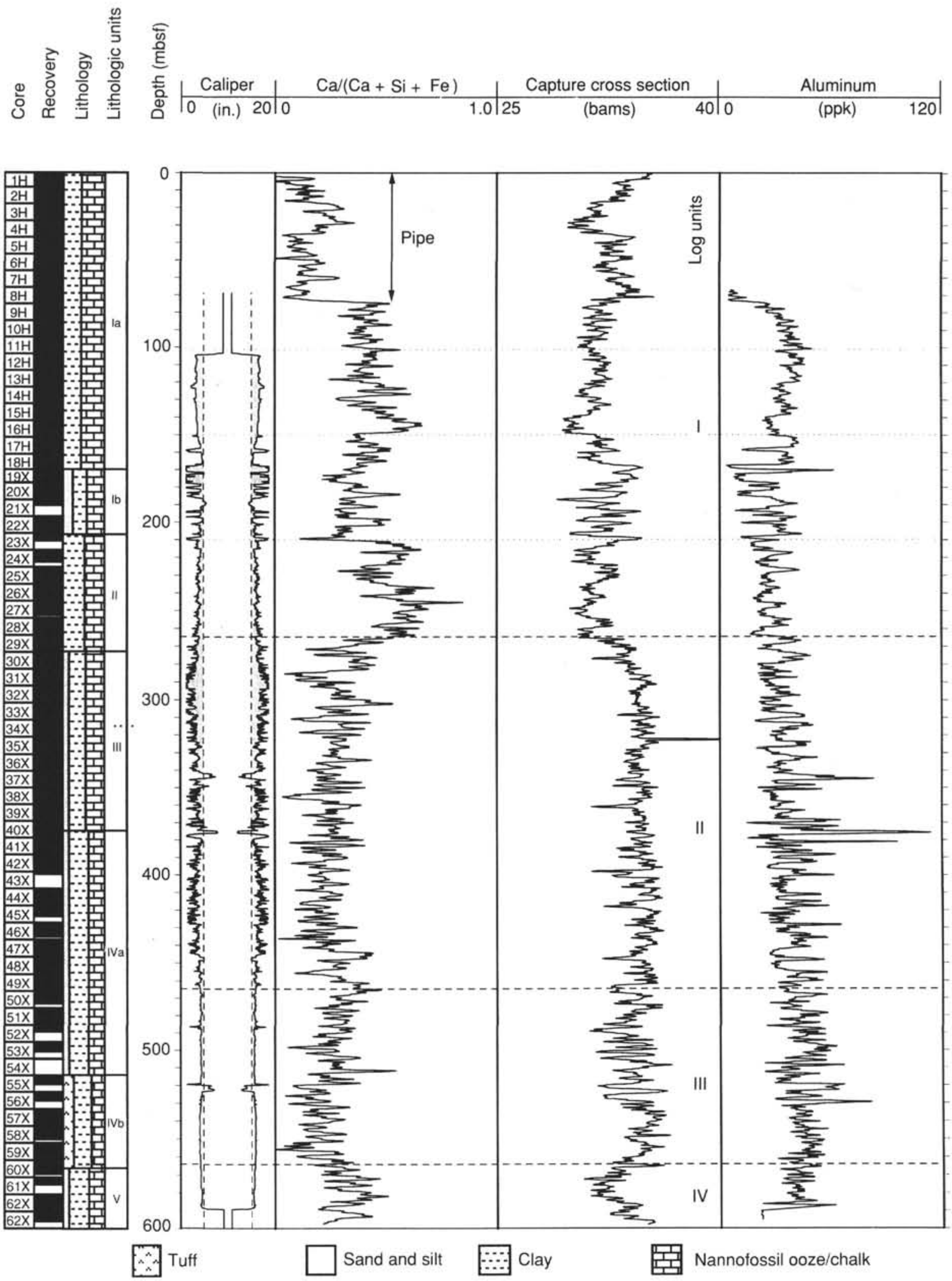

Figure 43. Hole 955A geochemical logs. Caliper data from the HLDT shown with elemental yield ratio of Ca/Ca + Fe + Si, thermal neutron capture cross section from the GST, and Al abundance from the AACT.

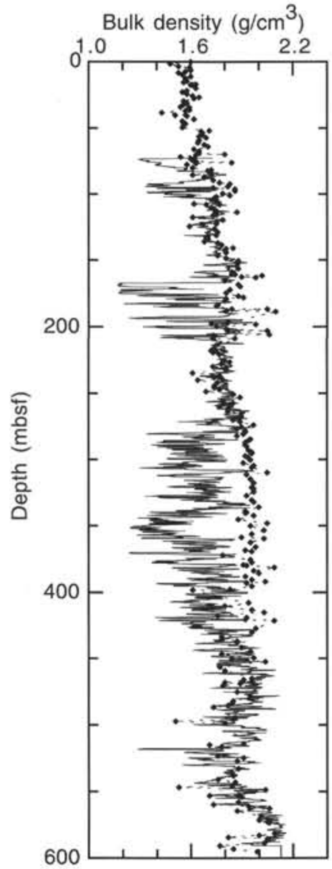

Figure 44. Log densities (solid line) from the HLDT compared to density measurements on discrete core samples (dotted line).

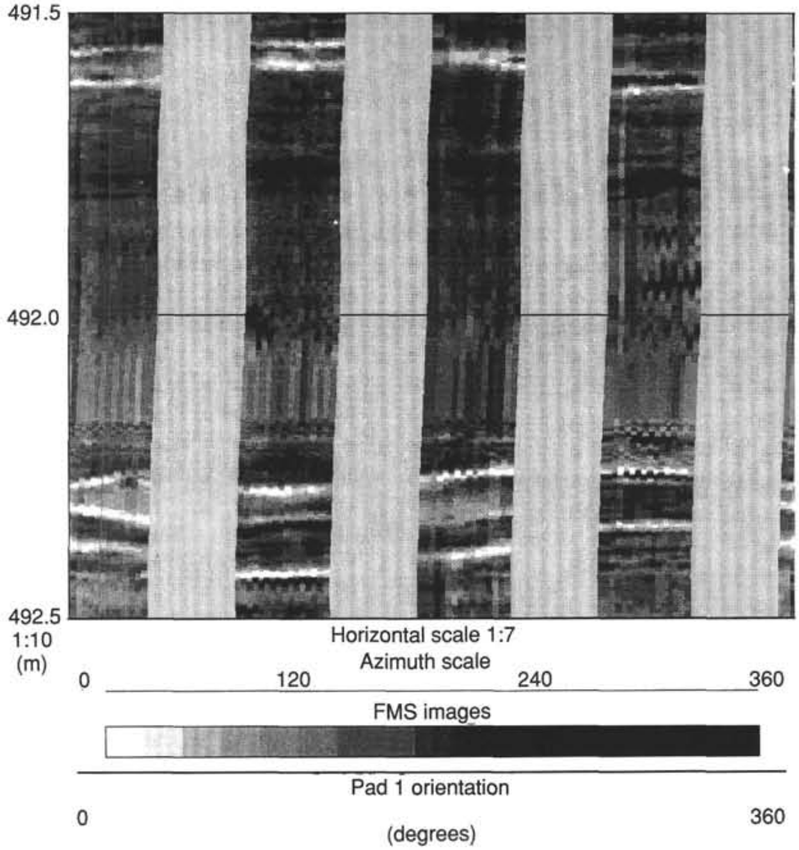

Figure 45. Oriented microresistivity traces from the FMS over a 1 m interval from 491.5 to 492.5 mbsf, Hole 955A. The images show several thin ash layers that appear as white (more resistive) bands.

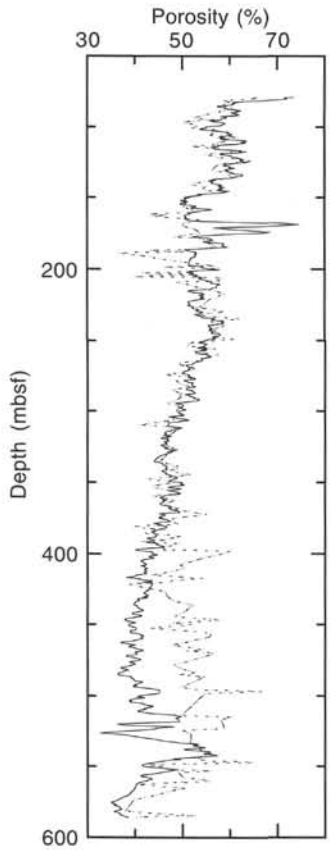

Figure 46. Hole 955A porosity calculated from the shallow focused resistivity log (solid line) using Archie's law (constants $a = 1.6$, $m = 1.4$) compared to measurements of porosity on discrete core samples (broken line).

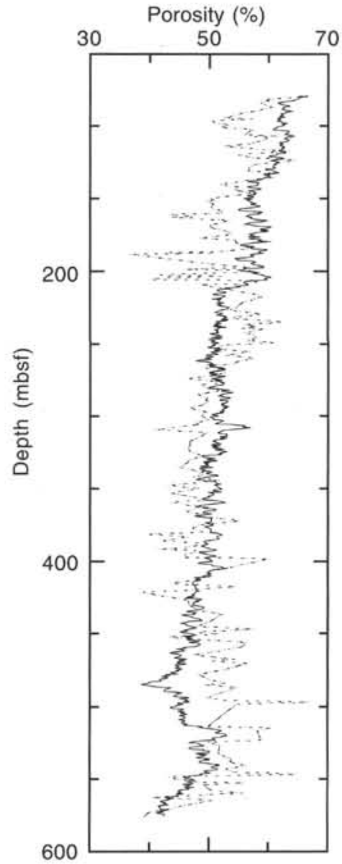

Figure 47. Hole 955A porosity calculated from the sonic velocity log (solid line) using the time average equation compared to measurements of porosity on discrete core samples (broken line).

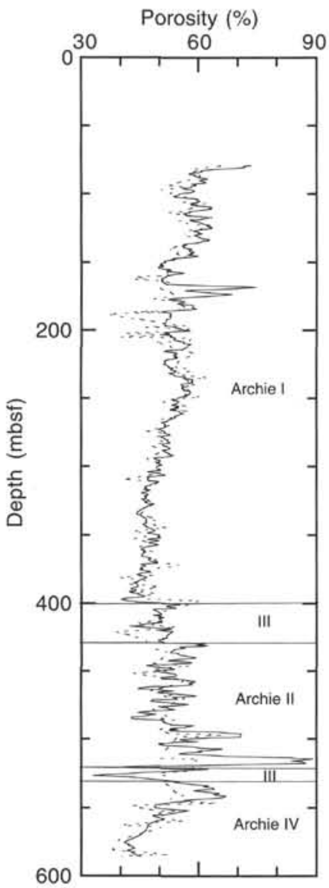

Figure 48. Porosity calculated from the shallow focused resistivity log (solid line) using zoned parameters of *a* and *m* for Archie's law compared to measurements of porosity on discrete core samples (broken line). I: $F = 1.6 \times \phi^{-1.4}$; II: $F = 4 \times \phi^{-0.6}$; III: $F = 3.7 \times \phi^{-1.19}$; IV: $F = 2 \times \phi^{-1.4}$.

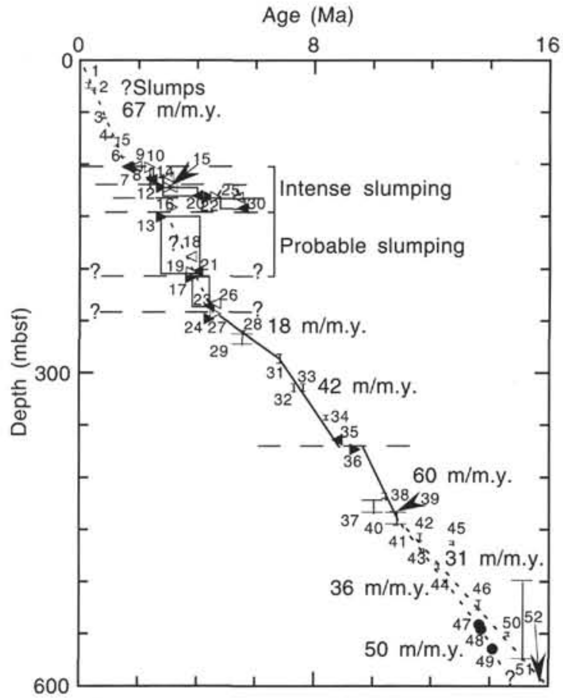

Figure 49. Sediment accumulation rates for Hole 955A. Vertical bars represent distance between sample points. Numbers refer to datum levels given in Table 14. Right-pointing filled triangle = nannofossil minimum age, left-pointing filled triangle = nannofossil maximum age, right-pointing open triangle = foraminifer minimum age, and left-pointing open triangle = foraminifer maximum age.

Table 14. Datum levels used in calculation of sediment accumulation rate curves.

	Event	Sample		Depth (mbsf)		Age	Age (Ma)	
		Top	Bottom	Top	Bottom	(Ma)	Maximum	Minimum
		157-955A-	157-955A-					
1	FO abundant *Gephyrocapsa* spp. (<3 µm)	3H-3, 132	3H-7, 70	21.92	27.30	0.26	—	—
2	LO *P. lacunosa*	3H-7, 70	4H-2, 70	27.30	29.30	0.46	—	—
3	LO *R. asanoi*	6H-7, 6	7H-1, 68	55.16	56.28	0.83	—	—
4	FO *R. asanoi*	8H-6, 73	8H-CC	73.33	74.92	1.03	—	—
5	LO *Gephyrocapsa* spp. (>5.5 µm)	8H-CC	9H-6, 44	74.92	82.54	1.24	—	—
6	FO *Gephyrocapsa* spp. (>5.5 µm)	10H-7, 13	10H-CC	93.23	93.73	1.46	—	—
7	Absence *C. macintyrei*	11H-7, 21	—	102.81	—	—	1.6	—
8	FO *Gr. truncatulinoides*	11H-6, 41	—	101.50	—	—	1.92	—
9	LO *D. brouweri*	11H-CC	—	103.08	—	—	—	1.95
10	LO *Gr. miocenica*	11H-CC, 0–2	—	103.07	—	—	—	2.37
11	Absence *D. pentaradiatus*	13H-2, 76	—	114.86	—	—	2.44	—
12	LO *D. tamalis*	13H-7, 59	—	122.19	—	—	—	2.76
13	LO *D. tamalis*	16H-7, 60	—	150.75	—	—	—	2.76
14	Absence *Gr. multicamerata*	12H-CC, 0–2	—	112.66	—	—	3	—
15	LO *Gr. multicamerata, D. altispira*, absence *Ss. seminulina*	13H-CC, 0–2	—	122.28	—	—	3.15	3
16	LO *Sphaeroidinellopsis seminulina*	15H-CC, 0–2	—	141.23	—	—	—	3.15
17	LO *R. pseudoumbilicus*	23X-3, 89	—	208.99	—	—	—	3.77
18	Absence *Gr. margaritae*	21X-CC, 0–2	—	189.00	—	—	3.79	—
19	LO *Gr. margaritae*	22X-CC, 0–2	—	203.57	—	—	—	3.79
20	FO *D. tamalis*	14H-6, 60	—	130.20	—	—	4.01	—
21	FO *D. tamalis*	22X-6, 11	—	203.11	—	—	4.01	—
22	LO *Amaurolithus* spp.	14H-CC	—	131.81	—	—	—	4.39
23	Absence *Amaurolithus* spp.	26X-2, 40	—	235.90	—	—	4.39	—
24	LO *Amaurolithus* spp.	27X-4, 26	—	248.36	—	—	—	4.39
25	LO *G. nepenthes*, absence *Gr. juanai*	14H-CC, 0–2	—	131.80	—	—	5.4	4.63
26	Absence *G. nepenthes*	25X-CC, 0–2	—	233.84	—	—	4.63	—
27	LO *G. nepenthes*	26X-CC, 0–2	—	243.58	—	—	—	4.63
28	LO *D. quinqueramus*	28X-5, 34	28X-CC	259.64	262.87	5.38	—	—
29	LO *Gr. juanai*	28X-CC, 0–2	29X-CC, 0–2	262.86	272.56	5.4	—	—
30	Absence *D. quinqueramus*	16H-1, 80	—	141.90	—	—	5.56	—
31	FO *R. pseudoumbilicus* (>7 µm)	30X-CC	31X CC	282.22	291.09	6.8	—	—
32	FO *A. primus*	33X-CC	34X-5, 80	310.78	317.60	7.3	—	—
33	LO *M. convallis*	33X-CC	34X-5, 80	310.78	317.60	7.6	—	—
34	FO *D. berggrenii/quinqueramus*	37X-1, 80	37X-4, 80	340.40	344.90	8.4	—	—
35	FO *M. convallis*, absence *R. pseudoumbilicus* (>7 µm)	39X-4, 80	—	364.00	—	—	8.8	—
36	LO *D. hamatus*, LO *R. pseudoumbilicus* (>7 µm)	40X-4, 80	—	373.60	—	—	—	9.4
37	FO *Nq. acostaensis*	45X-CC, 0–2	46X-CC, 0–2	422.29	433.69	9.99	—	—
38	FO *D. hamatus*	44X-CC	45X-3, 58	415.18	420.08	10.4	—	—
39	FO *C. coalitus*	46X-5, 43	46X-CC	432.63	433.70	10.7	—	—
40	LO *C. miopelagicus*	47X-CC	48X-1, 34	444.80	445.84	10.8	—	—
41	FO *G. nepenthes*	46X-CC, 0–2	47X-CC, 0–2	433.69	444.79	10.8	—	—
42	LO *C. floridanus*	48X-CC	49X-5, 33	454.05	461.53	11.6	—	—
43	FO common *D. kugleri*	50X-3, 74	50X-CC	468.54	471.57	11.7	—	—
44	FO *D. kugleri*	51X-CC	52X-CC	483.74	487.55	12.2	—	—
45	LO *C. premacintyrei*	49X-5, 33	49X-CC	461.53	464.20	12.7	—	—
46	LO *S. heteromorphus*	55X-CC	56X-3, 120	517.74	526.60	13.6	—	—
47	Ash layer	58X-1	—	541.60	—	~13.63	—	—
48	Ash layer	58X-4	—	546.00	—	13.71	—	—
49	Ash layer	60X-3	—	565.00	—	~14	—	—
50	LO *H. perch-nielsenae*	58X-CC	59X-1, 105	548.81	552.25	14.6	—	—
51	FO *Orbulina* spp.	53X-CC, 0–2	61X-CC, 0–2	498.99	574.25	15.1	—	—
52	LO *H. ampliaperta*	63X-4, 60	63X-CC	594.90	595.06	15.8	—	—

Note: Numbers in left column refer to numbers in Figure 49.

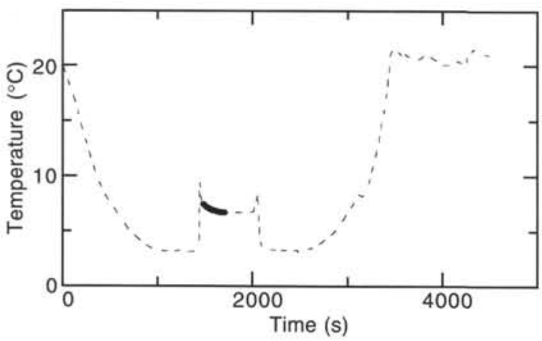

Figure 50. Measured temperatures (ADARA Tool 12) starting from the approximated zero time at the mud line and continuing through to the extraction of Core 157-955A-6H, 55.6 mbsf. The equilibrium temperature was extrapolated as 6.157°C, but this temperature is considered unreliable because of frictional heating of the probe. Dashed line shows measured temperature; solid line shows calculated temperature.

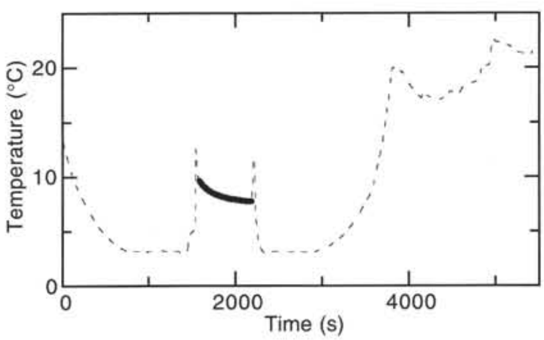

Figure 51. Measured temperatures (ADARA Tool 12) starting from the approximated zero time at the mud line and continuing through to the extraction of Core 157-955A-9H, 84.1 mbsf. The equilibrium temperature was extrapolated as 6.378°C. Dashed line shows measured temperature; solid line shows calculated temperature.

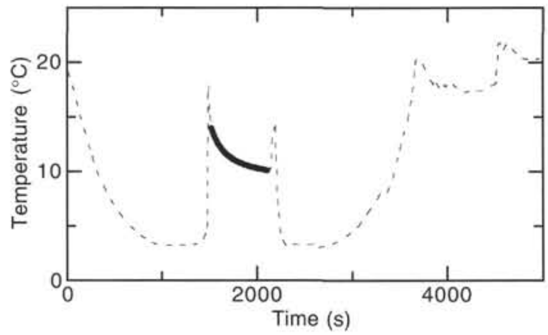

Figure 52. Measured temperatures (ADARA Tool 12) starting from the approximated zero time at the mud line and continuing through to the extraction of Core 157-955A-12H, 112.6 mbsf. The equilibrium temperature was extrapolated as 7.708°C. Dashed line shows measured temperature; solid line shows calculated temperature.

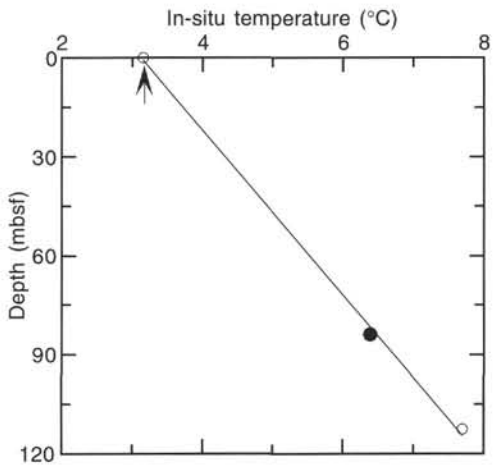

Figure 53. Hole 955A geothermal gradient from in-situ temperature measurements. The mud line (3.154°C, indicated by arrow) and equilibrium temperatures plotted vs. depth; the slope gives the geothermal gradient as 39.99°C/km ($y = 3.1263 + 0.03999x$). Filled circle = Core 157-955A-9H, 84.1 mbsf, 6.378°C; open circle = Core 157-955A-12H, 112.6 mbsf, 7.708°C. There was no equilibrium temperature calculated for Core 157-955A-3H and the temperature for Core 157-955A-6H was not used to calculate the gradient because of frictional heating of the probe.

SHORE-BASED LOG PROCESSING

HOLE 955A

Bottom felt: 2865.4 mbrf
Total penetration: 599.4 mbsf
Total core recovered: 534.08 m (89%)

Logging Runs

Logging string 1: DIT/LSS/HLDT/CNTG/NGT
Logging string 2: ACT/GST/NGT
Logging string 3: FMS/GPIT/NGT (three passes)

Wireline heave compensator was used to counter ship heave resulting from the mild sea conditions (0.3–1.25 m).

Bottom-hole Assembly

The following bottom-hole assembly depths are as they appear on the logs after differential depth shift (see "Depth shift" section) and depth shift to the seafloor. As such, there might be a discrepancy with the original depths given by the drillers on board. Possible reasons for depth discrepancies are ship heave, use of wireline heave compensator, and drill string and/or wireline stretch.

DIT/LSS/HLDT/CNTG/NGT: Bottom-hole assembly at 67.5 mbsf.

ACT/GST/NGT: Bottom-hole assembly at 73 mbsf.

FMS/GPIT/NGT: Bottom-hole assembly at 72 mbsf.

Processing

Depth shift: All original logs have been interactively depth shifted with reference to NGT from ACT/GST/NGT run, and to the seafloor (–2864.4 m). This value differs slightly from the "bottom felt" depth given by the drillers: it corresponds to the depth of the mud line as seen on the ACT/GST/NGT log. A list of the amount of differential depth shifts applied at this hole is available upon request.

Gamma-ray processing: NGT data have been processed to correct for borehole size and type of drilling fluid.

Acoustic data processing: The four transit time measurements have been edited to eliminate some of the noise and cycle skipping experienced during the recording. Then they have been averaged before calculating compressional velocity.

Geochemical processing: For detailed explanation of the processing please refer to the "Explanatory Notes" chapter (this volume) or to the geochem.doc file on the enclosed CD-ROM. The elemental yields recorded by the GST tool represent the relative contribution of only some of the rock-forming elements (iron, calcium, chlorine, silica, sulfur, hydrogen, gadolinium, and titanium—the last two computed during geochemical processing) to the total spectrum. Because other rock-forming elements are present in the formation (such as aluminum, potassium, etc.), caution is recommended in using the yields to infer lithologic changes. Instead, ratios (see acronyms.doc on CD-ROM) are more appropriate to determine changes in the macroscopic properties of the formation. A list of oxide factors used in geochemical processing includes the following:

$SiO_2 = 2.139$
$CaCO_3 = 2.497$
$FeO^* = 1.358$
$TiO_2 = 1.668$
$K_2O = 1.205$
$Al_2O_3 = 1.889$

FeO^* = computed using an oxide factor that assumes a 50:50 combination of Fe_2O_3 and FeO factors.

Quality Control

During the processing, quality control of the data is mainly performed by cross-correlation of all logging data. Large (>12 in.) and/or irregular borehole affects most recordings, particularly those that require eccentralization (CNTG, HLDT) and a good contact with the borehole wall.

Hole diameter was recorded by the hydraulic caliper on the HLDT tool (CALI) and the caliper on the FMS string (C1 and C2).

Data recorded through bottom-hole assembly, such as the gamma ray recorded above 69 mbsf, should be used qualitatively only because of the attenuation on the incoming signal. Invalid gamma-ray data were recorded from 67 to 74 mbsf during the DIT/LSS/HLDT/CNTG/NGT run.

FACT = quality control curve in geochemical processing. Accuracy of the estimates is inversely proportional to the magnitude of the curve.

Note: Details of standard shore-based processing procedures are found in the "Explanatory Notes" chapter, this volume. For further information about the logs, please contact:

Cristina Broglia
Phone: 914-365-8343
Fax: 914-365-3182
E-mail: chris@ldeo.columbia.edu

Elizabeth Pratson
Phone: 914-365-8313
Fax: 914-365-3182
E-mail: beth@ldeo.columbia.edu

Hole 955A: Natural Gamma Ray-Resistivity-Sonic Logging Data

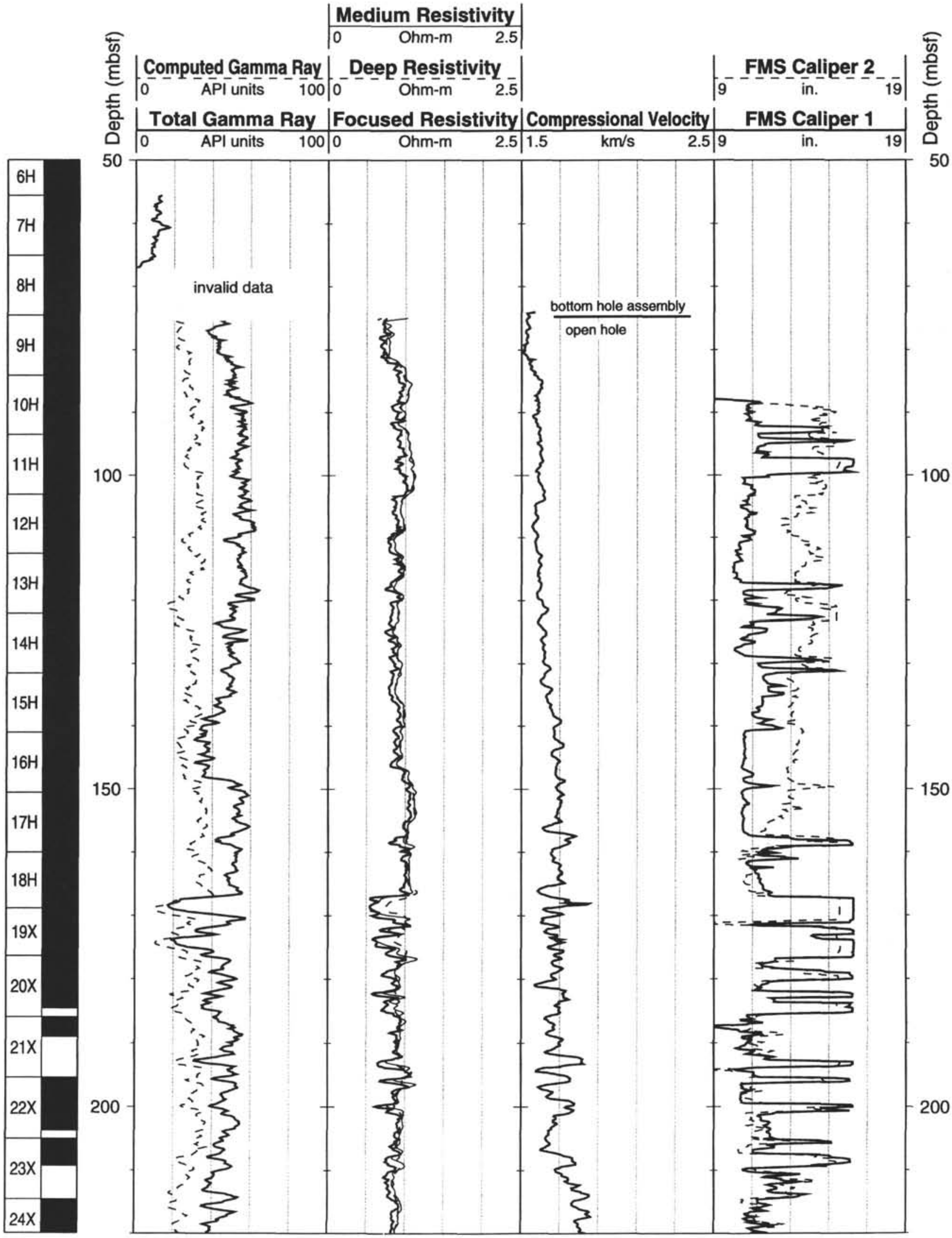

Hole 955A: Natural Gamma Ray-Resistivity-Sonic Logging Data (cont.)

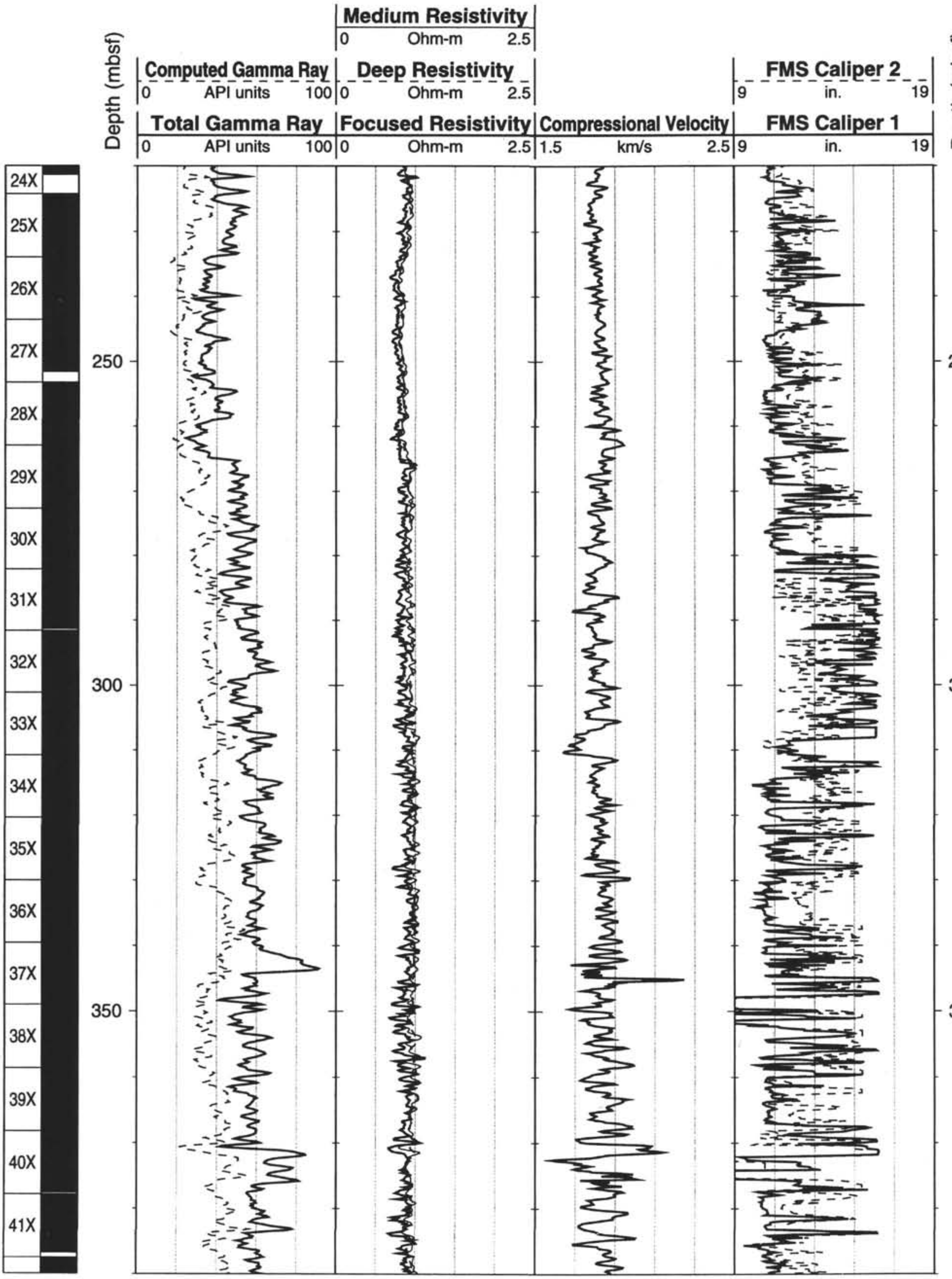

Hole 955A: Natural Gamma Ray-Resistivity-Sonic Logging Data (cont.)

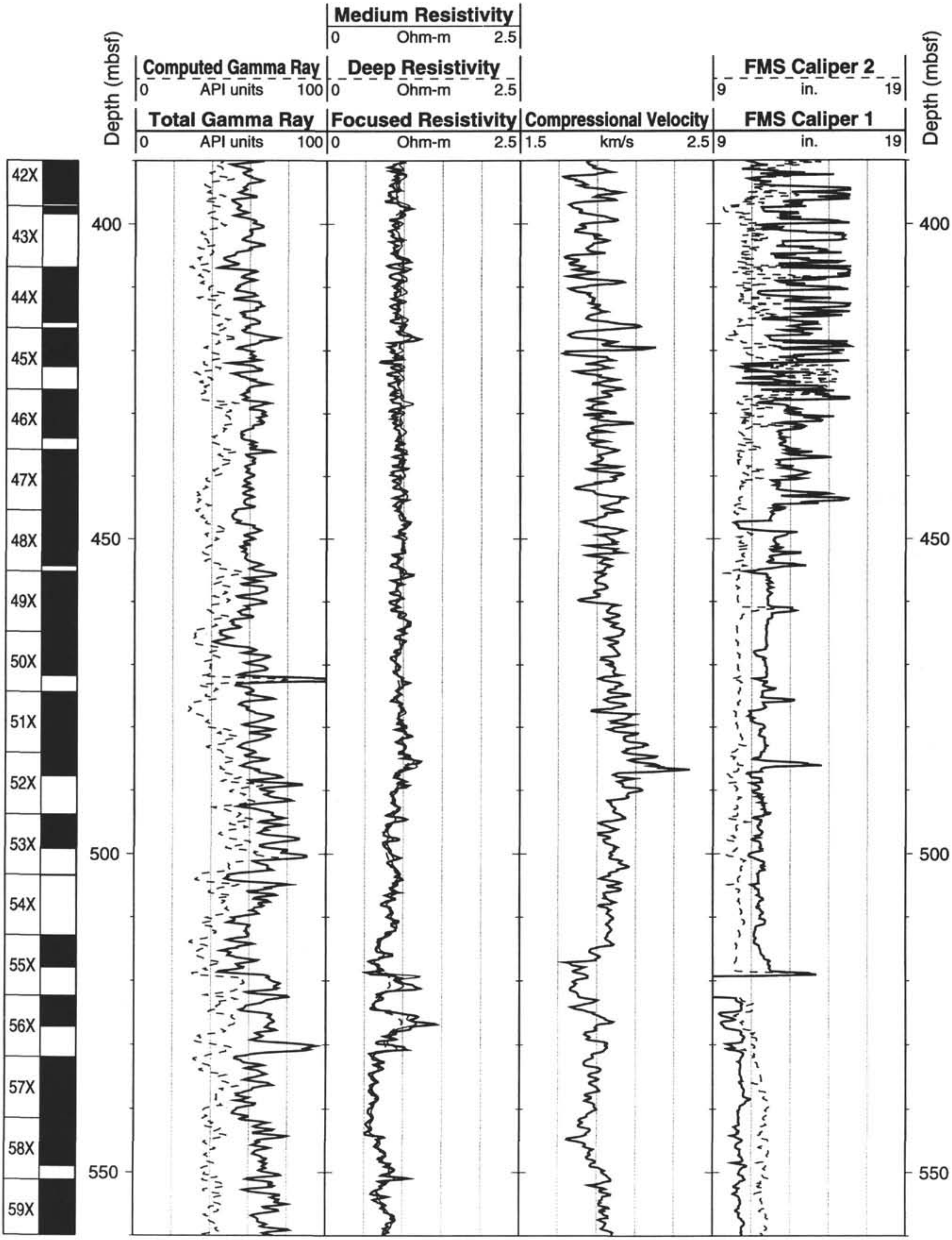

Hole 955A: Natural Gamma Ray-Resistivity-Sonic Logging Data (cont.)

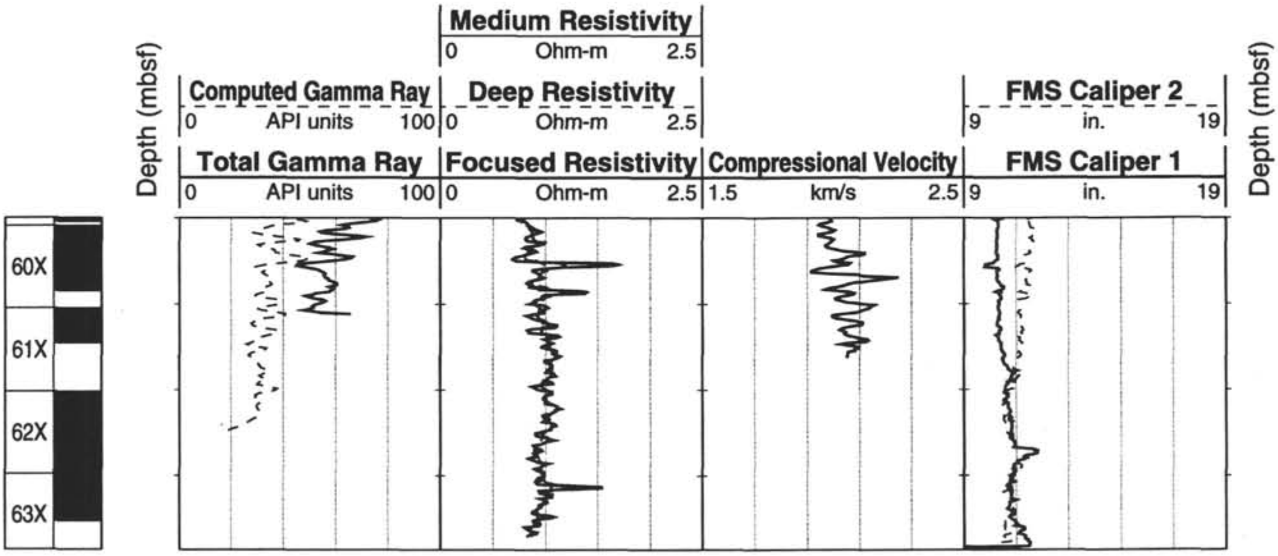

Hole 955A: Natural Gamma Ray-Density-Porosity Logging Data

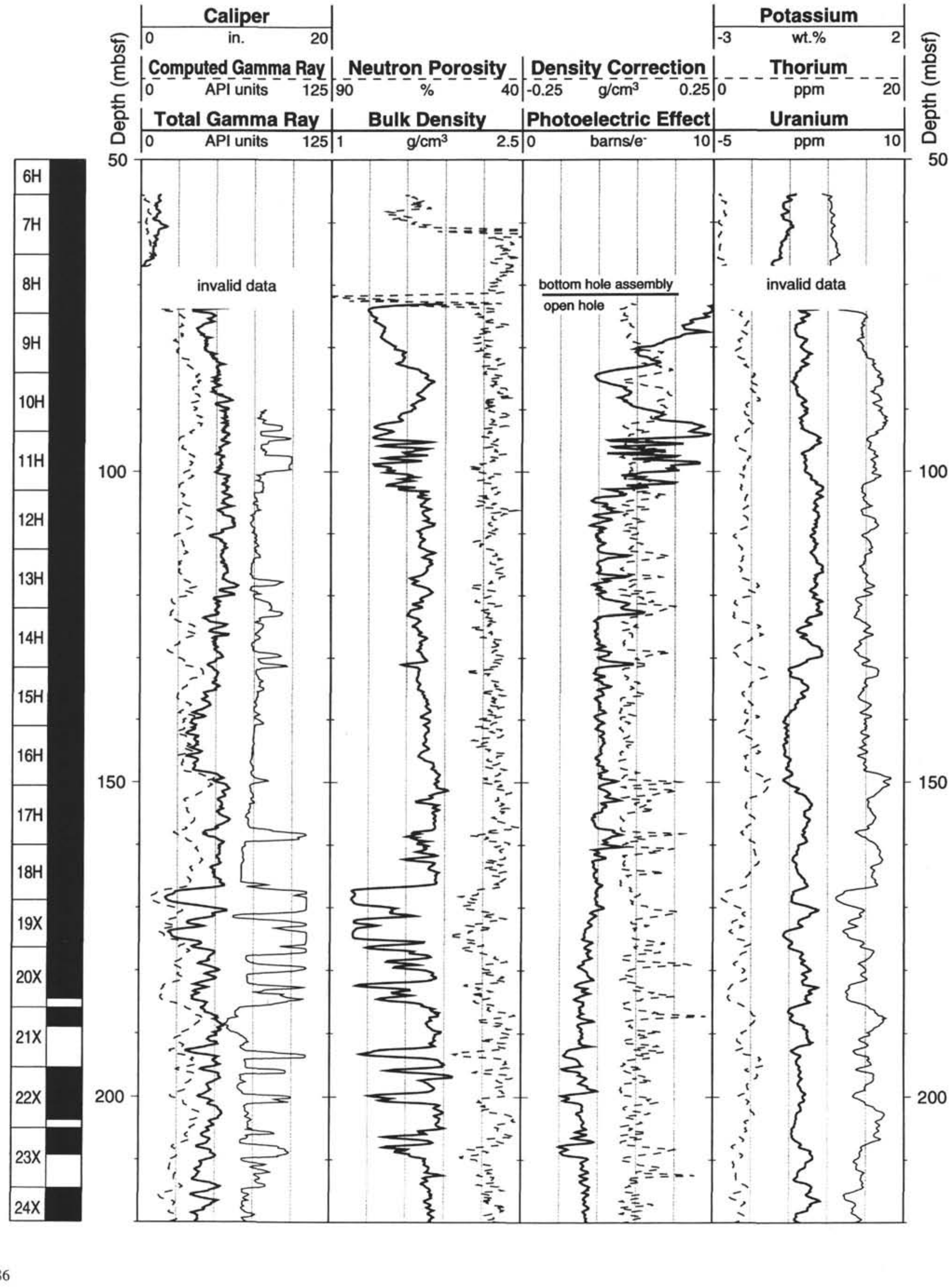

Hole 955A: Natural Gamma Ray-Density-Porosity Logging Data (cont.)

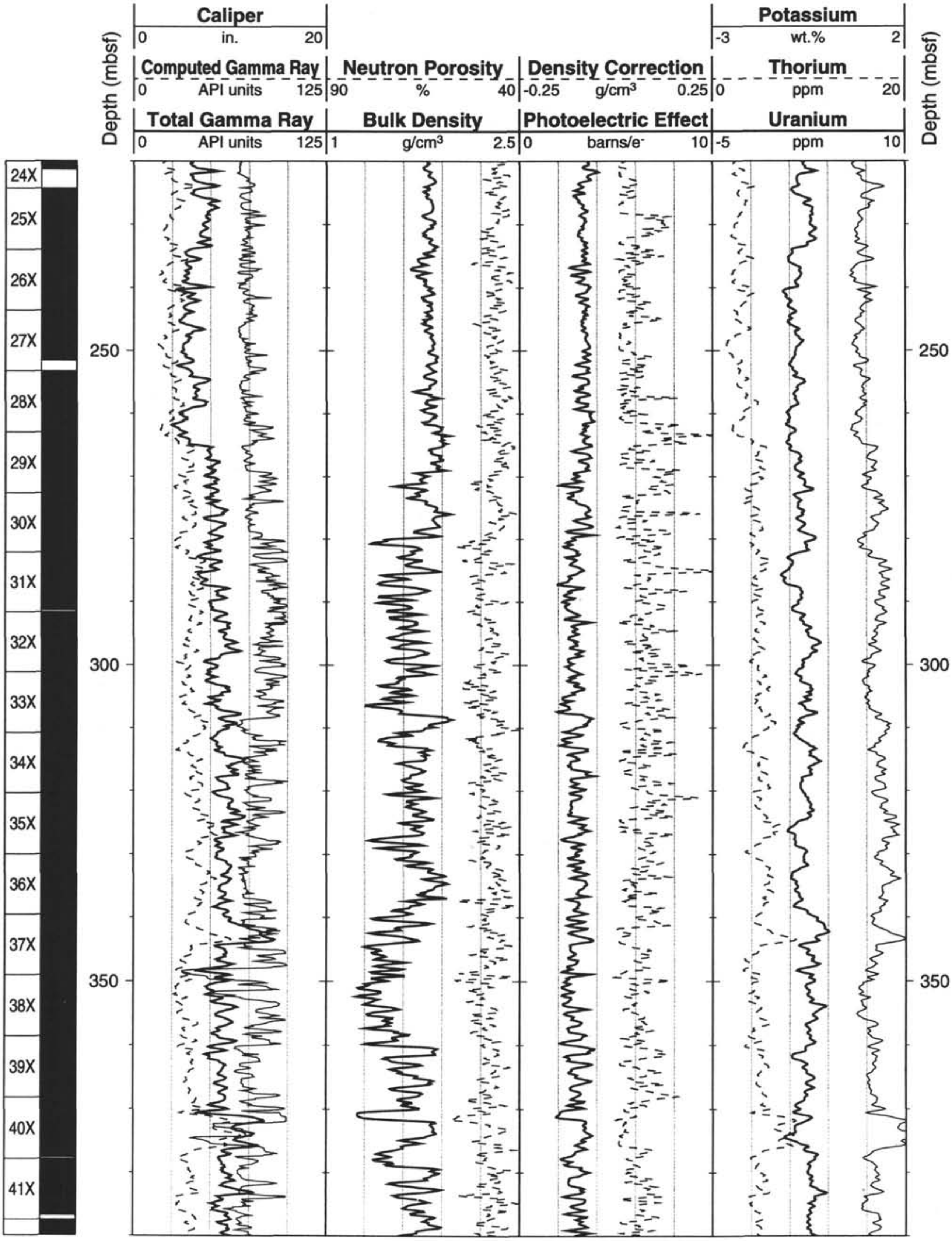

Hole 955A: Natural Gamma Ray-Density-Porosity Logging Data (cont.)

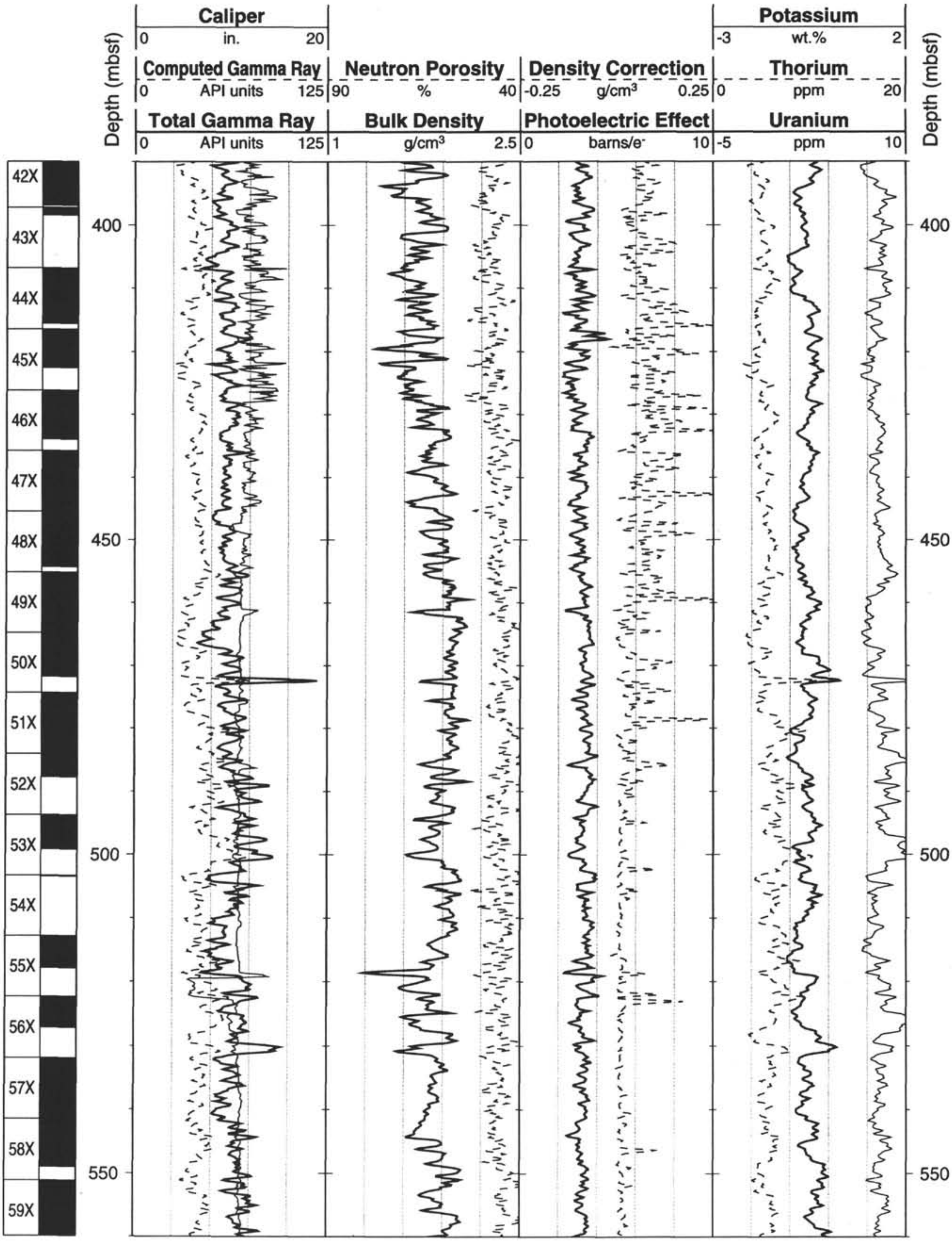

Hole 955A: Natural Gamma Ray-Density-Porosity Logging Data (cont.)

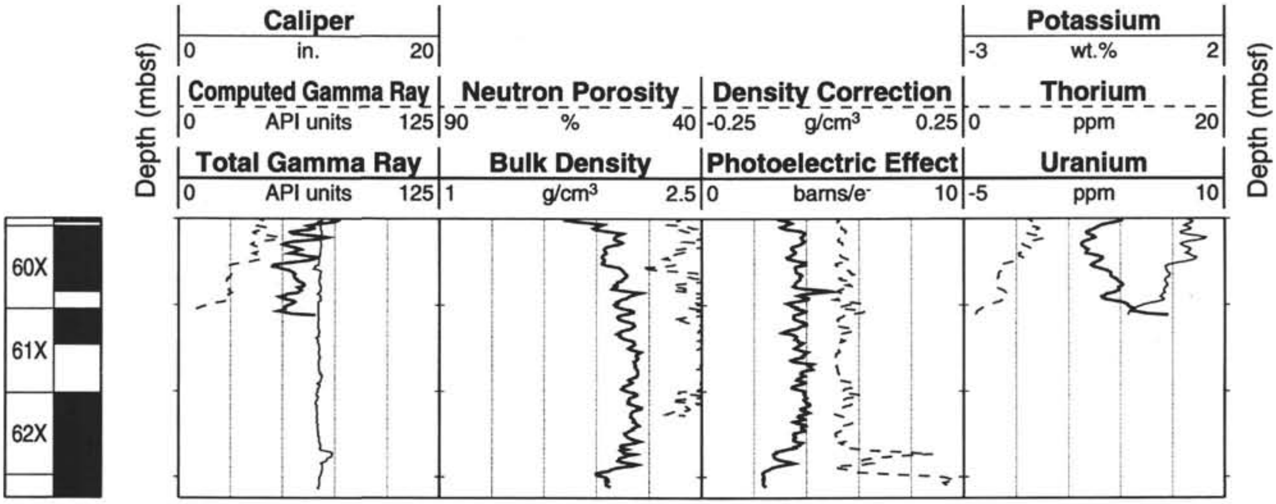

Hole 955A: Natural Gamma Ray Logging Data

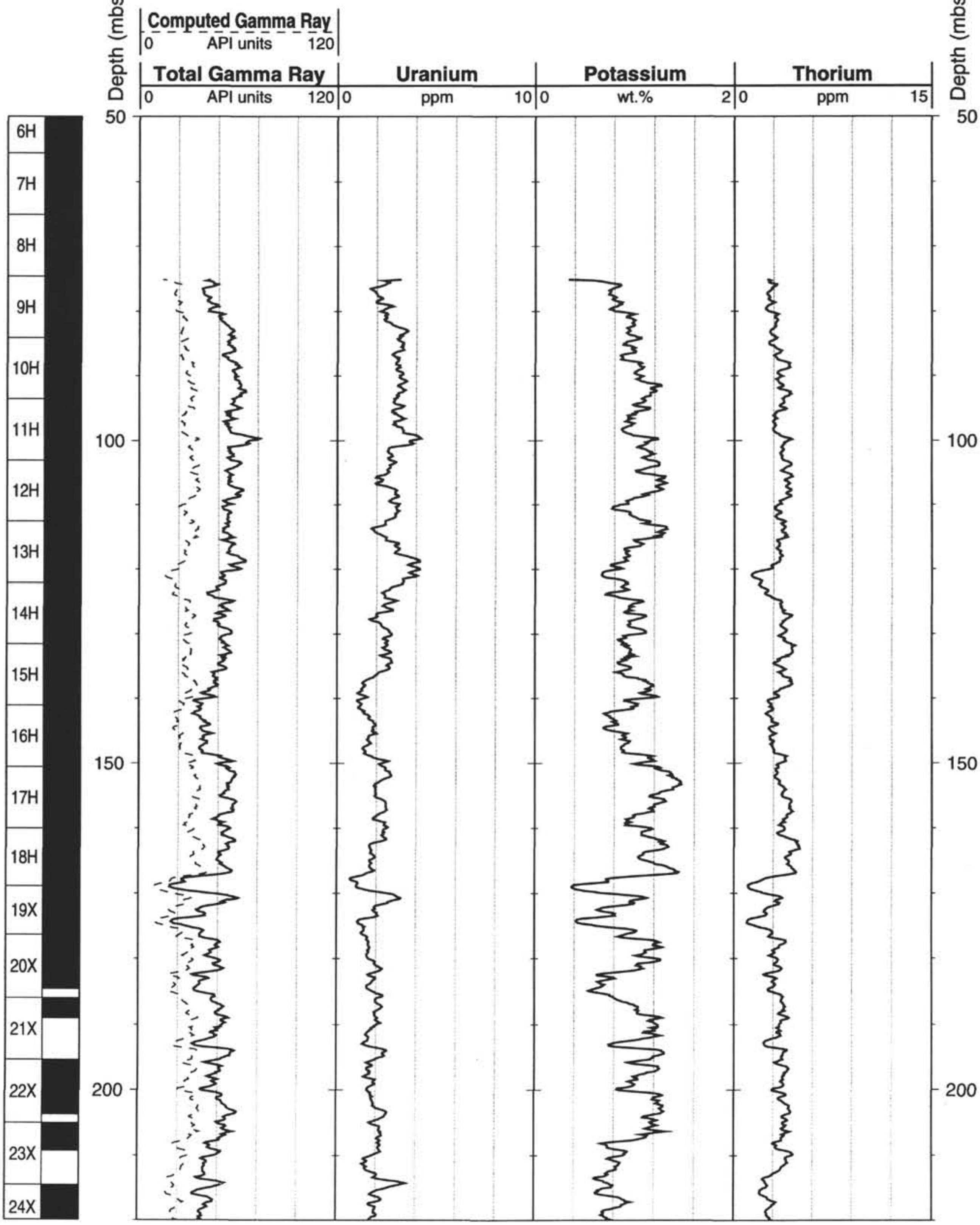

Hole 955A: Natural Gamma Ray Logging Data (cont.)

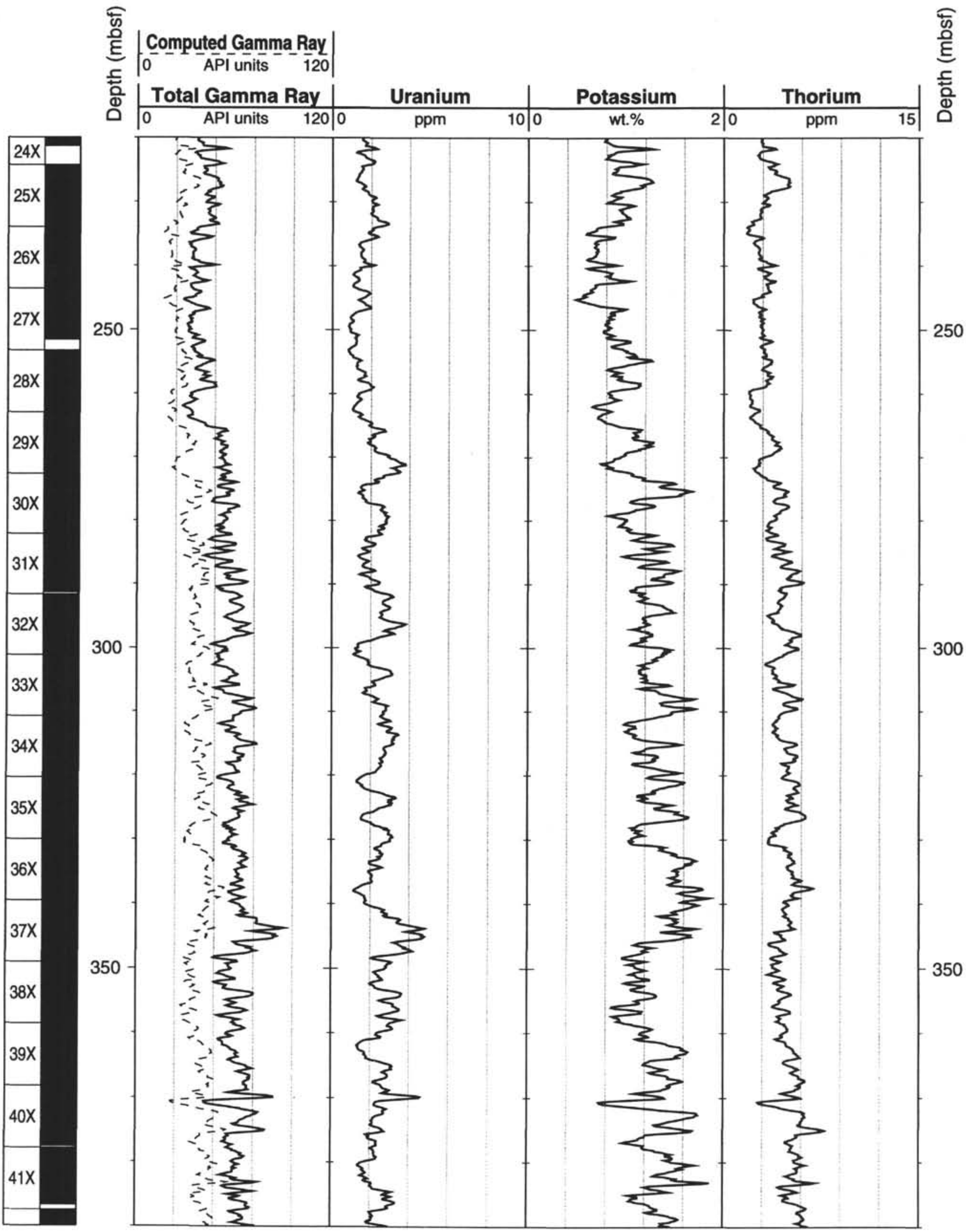

Hole 955A: Natural Gamma Ray Logging Data (cont.)

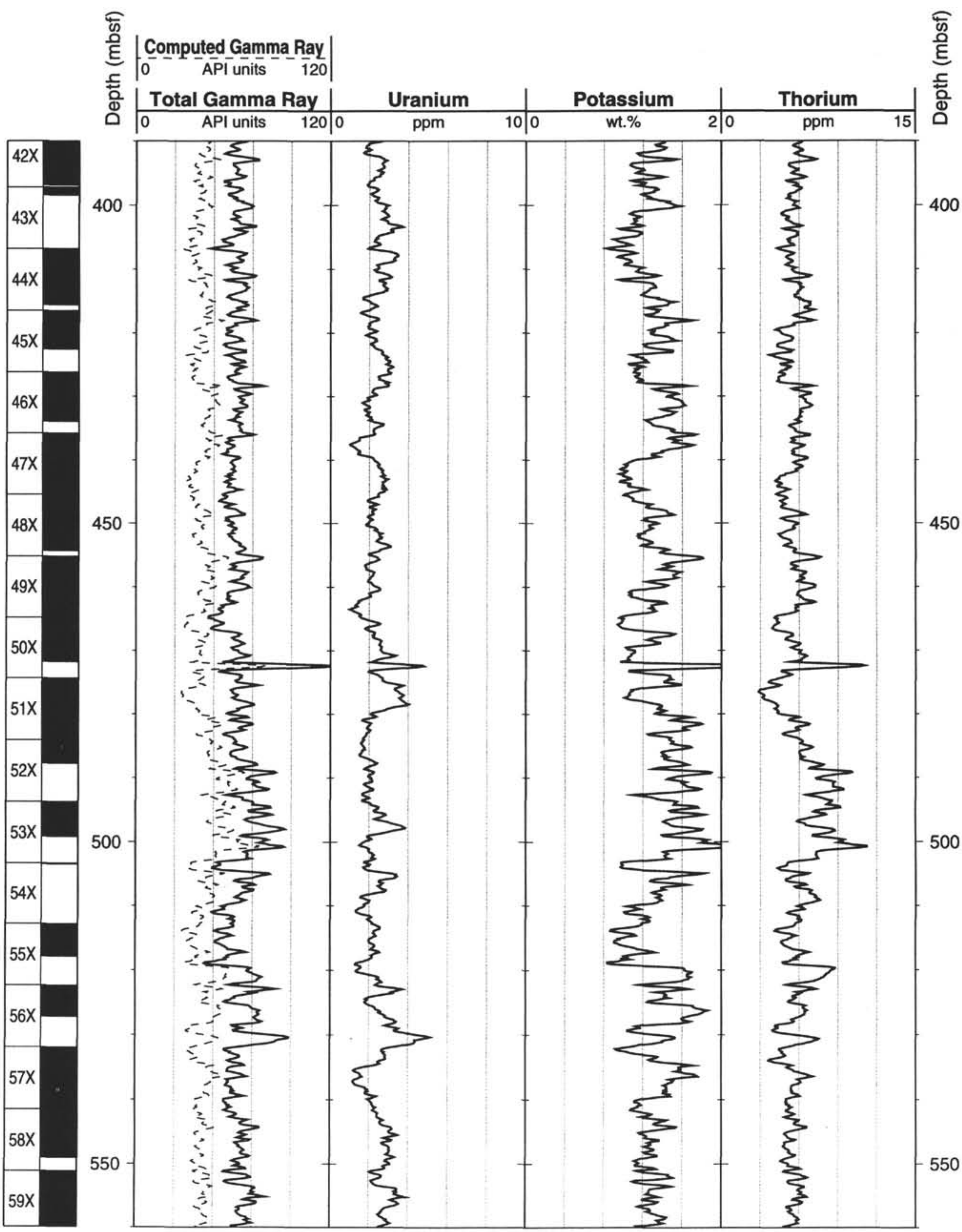

Hole 955A: Natural Gamma Ray Logging Data (cont.)

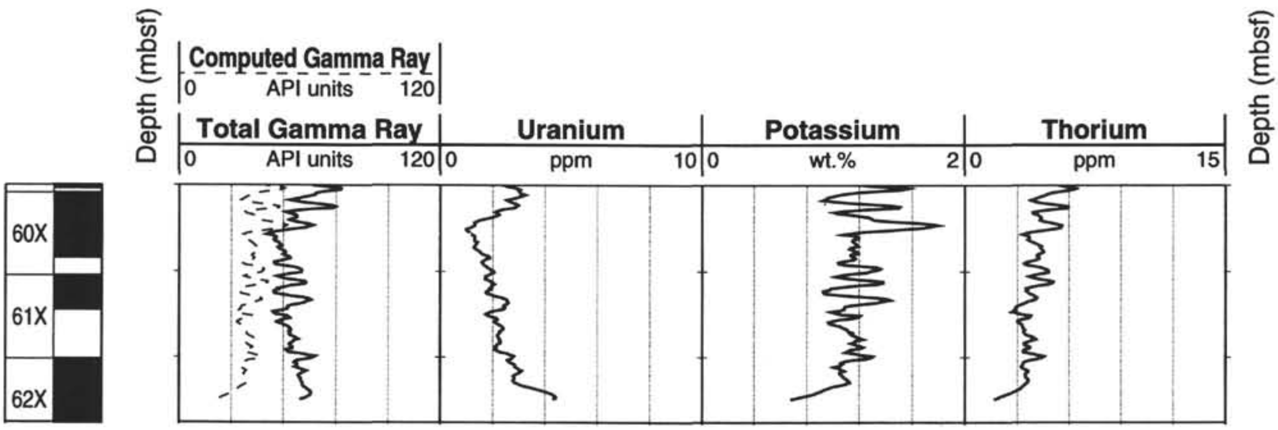

Hole 955A: Geochemical Logging Data

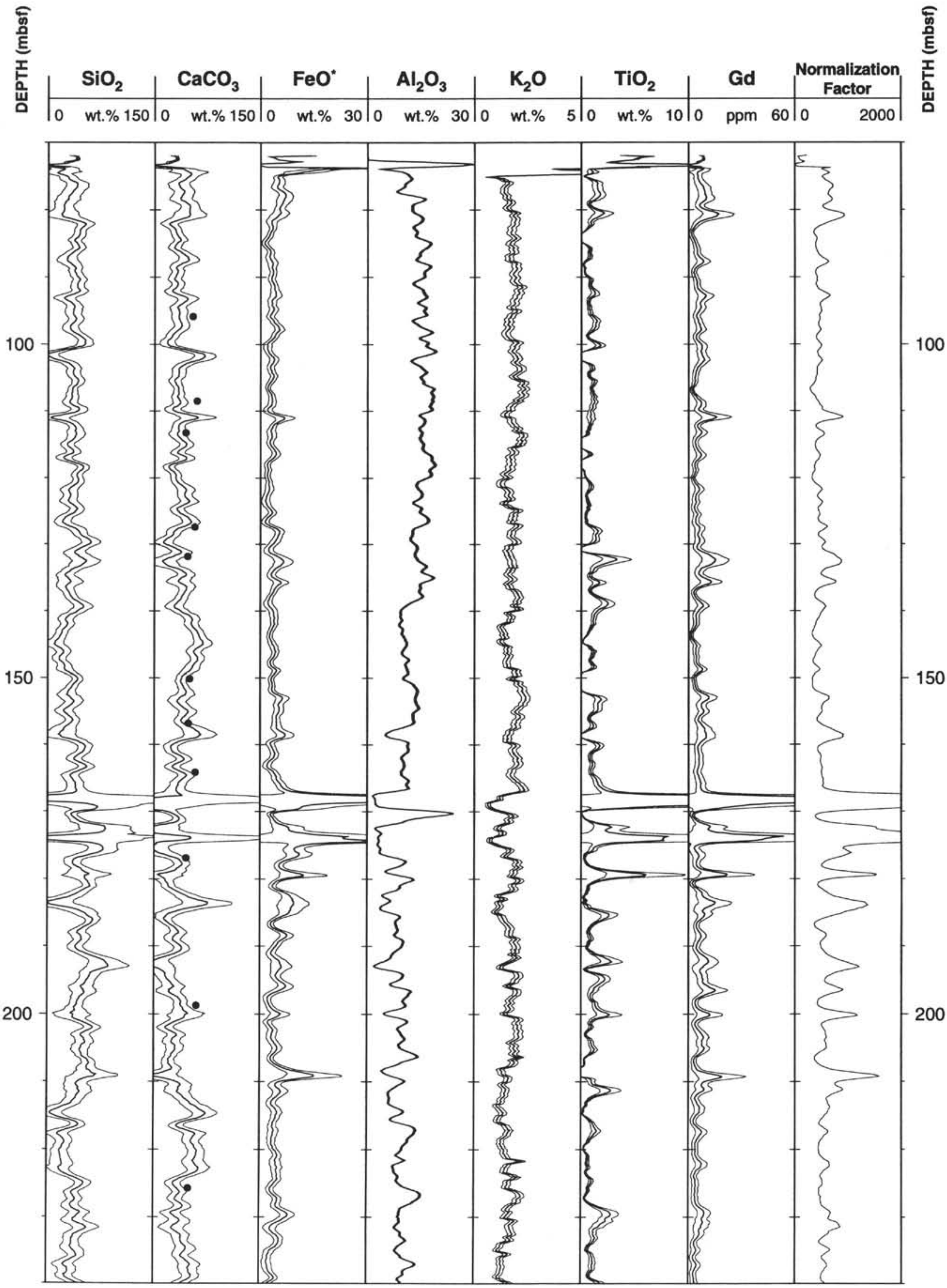

Hole 955A: Geochemical Logging Data (cont.)

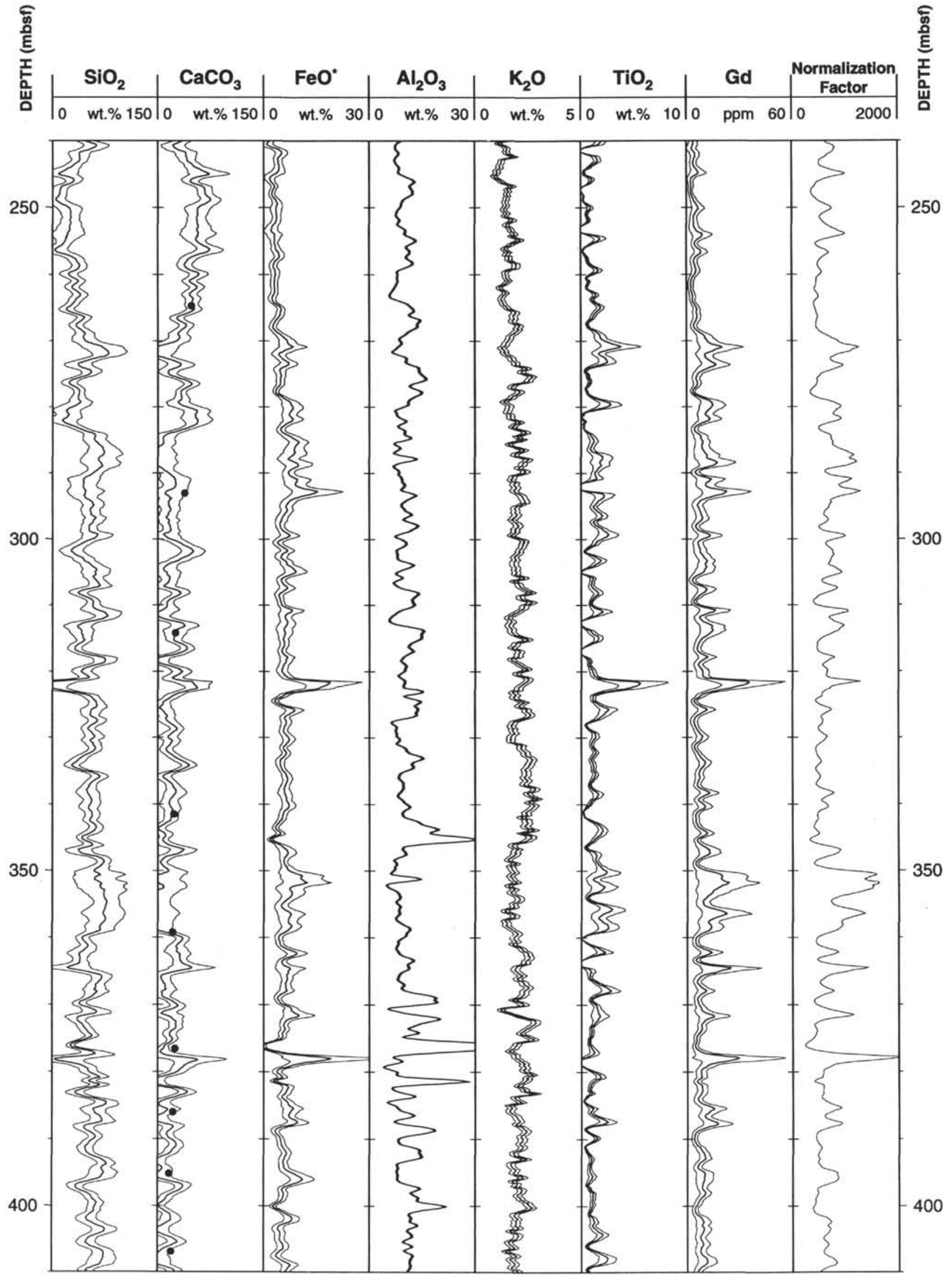

Hole 955A: Geochemical Logging Data (cont.)